Fall 2016

Aerosol transport by coughing in a depressurized and air-conditioned chamber

Bo Zhang
New Jersey Institute of Technology

ABSTRACT

AEROSOL TRANSPORT BY COUGHING IN A DEPRESSURIZED AND AIR-CONDITIONED CHAMBER

by

Bo Zhang

Expiratory droplets from human coughing in an air-conditioned environment have always been considered to be potential carriers of pathogens, responsible for respiratory disease transmission. The air movement/circulation and ambient conditions such as pressure and temperature are all key factors of aerosol transport. To study the transmission of disease by human coughing in a depressurized air-conditioned chamber, there are many technical challenges, including the following: 1) the study of simulating human coughing; 2) the collection of aerosol generated by coughing; 3) the CFD simulation of coughing-induced aerosol transport in an air-conditioned chamber; 4) the validation of such a CFD simulation by experiment; 5) the depressurization of the air-conditioned chamber and 6) the mechanistic study of droplet evaporation. Accordingly, this work provides the following to study the aerosol transmission in a depressurized chamber: a transient repeatable bimodal cough simulator is designed and built; a chamber with air-conditioning and circulation is built; a breathing simulator is designed and built as well as measurement validation is done; a full field three dimensional CFD simulation of the aerosol transport in the air-conditioned chamber is established; a droplet evaporation model is built as well as the technology of depressurization for an open flow system.

The cough and breath simulators are designed for purposes of aerosol generation and collection. The CFD simulation is used to calculate various conditions of the aerosol transport and deposition, especially the effect of the air movement/circulation and

ambient conditions. The experiment chamber is for validation of CFD simulation. The droplet evaporation is built to better simulate one of the most important factors for the droplets, the evaporation effect, and can be implemented into the CFD model by User-Defined Functions. The depressurization technology is to provide the vacuum environment for the experiment air-conditioned chamber. This study also seeks a breakthrough of a heat transfer model of latent heat partition, which would be a critical factor for the droplet evaporation. The whole project lays down the foundation of the study of aerosol transport in a depressurized air-conditioned chamber, for its inhalation by human, contamination into AC system and deposition on the environment surfaces. It also initiates the coupling with medical model by providing critical input conditions for coughing-induced disease transmission to study the disease transmission as well as de-contamination. Future studies would include the calibration and measurement of the breath simulator, the aerosol transport measurement in the air-conditioned chamber, more parametric study of CFD simulation, a more sophisticated multi-component evaporation model and the implementation of this evaporation model in the CFD simulation through User-Defined Functions. If possible, one could couple the more realistic latent heat partition model with the droplet evaporation model and also include the depressurization effect for at least the CFD simulation if not for the experiment.

AEROSOL TRANSPORT BY COUGHING IN A DEPRESSURIZED AND AIR-CONDITIONED CHAMBER

by
Bo Zhang

A Dissertation
Submitted to the Faculty of
New Jersey Institute of Technology
in Partial Fulfillment of the Requirements for the Degree of
Doctor of Philosophy in Mechanical Engineering

Department of Mechanical and Industrial Engineering

January 2017

.

APPROVAL PAGE

AEROSOL TRANSPORT BY COUGHING IN A DEPRESSURIZED AND AIR-CONDITIONED CHAMBER

Bo Zhang

Dr. Chao Zhu, Dissertation Advisor Professor of Mechanical and Industrial Engineering, NJIT	Date
Dr. Zhiming Ji, Committee Member Associate Professor of Mechanical and Industrial Engineering, NJIT	Date
Dr. Chao-Hsin Lin, Committee Member Technical Fellow, Boeing Commercial Airplanes	Date
Dr. I. Joga Rao, Committee Member Professor and Chair of Mechanical and Industrial Engineering, NJIT	Date
Dr. Eon Soo Lee, Committee Member Assistant Professor of Mechanical and Industrial Engineering, NJIT	Date

BIOGRAPHICAL SKETCH

Author: Bo Zhang

Degree: Doctor of Philosophy

Date: January 2017

Undergraduate and Graduate Education:

- Doctor of Philosophy in Mechanical Engineering,
  New Jersey Institute of Technology, Newark, NJ, 2017

- Master of Science in Fluid Mechanics Engineering,
  North China Electric Power University, Beijing, P. R. China, 2010

- Bachelor of Science in Aircraft Engine Engineering,
  Beijing University of Aeronautics & Astronautics, Beijing, P. R. China, 2007

Major: Mechanical Engineering

Presentations and Publications:

Zhang, Bo, He Pengfei, Du, Bing, Zhu, Chao, "Effects of Asymmetric Feeding on Gas-Solid-Liquid Transport and Catalytic Cracking Reaction in the Feed Zone of Riser," Chemical Engineering Science, 2016 (In press)

Zhang, Bo, Zhu, Chao, Ji, Zhiming, Lin, Chao-Hsin, "Design and Characterization of a Cough Simulator," Indoor Air, 2016 (revision)

He, Pengfei, Zhang, Bo, Zhu, Chao, Ji, Zhiming, Lin, Chao-Hsin, "Dynamic Process Modeling on Depressurization by Cooling-Controlled Condensation in a Closed Chamber," International Journal of Heat and Mass Transfer, 78, 330 (2014)

Patel, Rajesh, He, Pengfei, Zhang, Bo, Zhu, Chao, "Transport of Interacting and Evaporating Liquid Sprays in a Gas-Solid Riser Reactor," Chemical Engineering Science, 100, 433 (2013)

Zhang, Bo, Guo, Guangyu, Zhu, Chao, Ji, Zhiming, "Dynamic process modeling on a condensation based depressurization system," AVS63, Nashville, TN, USA, November 2016

Zhang, Bo, He Pengfei, Du, B., Zhu, Chao, "Effects of Asymmetric Feeding on Gas-Solid-Liquid Transport and Catalytic Cracking Reaction in the Feed Zone of Riser," GLS12, Manhattan, NY, USA, July 2016

Zhang, Bo, He, Pengfei, Zhu, Chao, Ji, Zhiming., Lin, Chao-Hsin, "Dynamic Process Modeling on Depressurization by Cooling-Controlled Condensation in a Closed Chamber," ASME-FEDSM, Chicago, IL, USA, August 2014

Zhang, Bo, He, Pengfei, Zhu, Chao, "Modeling on Hydrodynamic Coupled FCC Reaction in Gas-Solid Riser Reactor," ASME-FEDSM, Chicago, IL, USA, August 2014

He, Pengfei, Patel, Rajesh, Wang, D., Zhu, Chao, Zhang, Bo, "Hydrodynamic Model of Gas-Solids Risers Flow with Continuous Axial and Radial Flow Structure," ASME-FEDSM, Chicago, IL, USA, August 2014

He, Pengfei, Patel, Raivat, Zhang, Bo, Zhu, Chao "Liquid Attachment and Momentum Transfer by Collisions between Free-Fall Solids and Liquid Spray Droplets," ASME-IMECE, Houston, TX, USA, November 2012

This dissertation is dedicated to my family

For my parents, who gave me life

For my grandparents, who raised me

For my life long philosophy, always being optimistic in this world

And try to make it a better place:

不見南師久，漫說北群空。
當場只手，畢竟還我萬夫雄。
自笑堂堂漢使，得似洋洋河水，依舊只流東？
且複穹廬拜，會向藁街逢！

堯之都，舜之壤，禹之封。
於中應有，壹個半個恥臣戎！
萬裏腥膻如許，千古英靈安在，磅礴幾時通？
胡運何須問，赫日自當中。

——陳亮《水調歌頭・送章德茂大卿使虜》

ACKNOWLEDGMENT

I would like to express my deepest appreciation to my advisor Prof. Chao Zhu, who instilled not only research skills and academic knowledge, but also the philosophy of life into me. He is more than an advisor to me for and beyond research. I would also like to thank Prof. Zhiming Ji, who helped me a lot and is not official but a co-advisor in my heart. I want to appreciate Dr. Chao-Hsin Lin, whom financially initiated my dissertation study and educated me with his wisdom and knowledge. After all, none of my accomplishments could be achieved without the continuous financial support from Department of Mechanical & Industrial Engineering, and I sincerely thank the Chair and Prof. I. Joga Rao for his support and serving as committee member as well as Prof. Eon Soo Lee.

I consider myself very luck for becoming friend with so many people here at NJIT. Our Lab Coordinator Joseph Glaz and his team Gregory Policastro and Nick, who always offer their valuable help even they are constantly occupied. Prof. Herli Surjanhatta is the nicest person of the whole department and also I consider him as one of my greatest friend. This five year-journal is by no means short, during the time I learned so much especially from Dr. Pengfei He, who is another Ph.D. graduated from our group and senior than me. I also want to thank Dr. Fangda Cui, Mr. Zhong Sun and Dr. Wei Hao, my best and closest friends. I could not name everyone, but last not least, I would like to thank my group mates, Mr. Gao Pan and Mr. Guangyu Guo and many others who worked with us. It is an immeasurable honor to cooperate with each and every one of you.

TABLE OF CONTENTS

TABLE OF CONTENTS
(Continued)

TABLE OF CONTENTS
(Continued)

Chapter **Page**

TABLE OF CONTENTS
(Continued)

Chapter **Page**

LIST OF TABLES

LIST OF FIGURES

LIST OF FIGURES
(Continued)

LIST OF FIGURES
(Continued)

LIST OF FIGURES
(Continued)

LIST OF SYMBOLS

A	Area
c	Specific heat capacity
C_D	Drag coefficient
c_p	Specific heat at constant pressure
D	Diameter; mass diffusivity
d	diameter
g	Gravity acceleration
H	Cone height
h	Convective heat transfer coefficient, enthalpy
h_{fg}	Latent heat
J	Diffusion flux; area coefficient
K	Calibration parameter
k	Thermal conductivity
L	Latent heat; characteristic length; distance
m	Mass
$\dot{m}$	Mass flow rate, condensate rate
Nu	Nusselt number
p	Pressure
pe	Peclet number
Pr	Prandtl number
q	Heat flux

R	Gas constant; radius of droplet
r	Chamber radius; radius in general
Ra	Raleigh number
Re	Reynolds number
S	Source term
Stk	Stokes number
T	Temperature
t	Time
U	Velocity
u	Internal energy, velocity
V	Volume
Y	Species fraction

Greek letters

α	Mole percentage; coefficient; voidage
β	Coefficient
δ	Thickness; condensation film thickness
μ	Viscosity
ρ	Density

Subscripts

0	Initial condition
a	Air or non-condensable gas

c	Coolant water
ch	Chamber
conv	Convection
d	Droplet
FD	Flushing distributor (steam pipe)
i	Inlet; phase
l	Liquid, condensate water
m	mixture
NCG	Non condensable gas
o	Outlet
p	Pipe of cooling coil
R	Radius of droplet
r	Radiation
rad	Radiation
ref	Reference condition
s	Surface
sat	Saturated condition
T	Total
v	Steam vapor
δ	Thickness

CHAPTER 1

INTRODUCTION

1.1 Background of Dissertation

The transmission of infectious respiratory diseases has always been a topic of public health, drawing significant attention of various disciplines for decades (Morawska, 2006; Cheng *et al*., 2013). One of the most common routes of transmission is through inhaling pathogen-carrying aerosol/airborne droplets from sneezing and coughing, such as in the common cold and influenza (Moser, 1979), in severe acute respiratory syndrome (SARS) (Olsen *et al.*, 2003), in avian flu and Ebola (Funk and Kumar, 2015; Osterholm *et al.*, 2015; WHO, 2015). Due to the limited knowledge of Ebola transmission, even with modern technology, an unprecedented number of medical personnel in the front line are still unable to evade infection (WHO, 2014). More importantly, it is unrealistic if not impossible to predict new outbreak of contagions in the future, but it is reasonable to believe that the spread of most respiratory diseases follows a certain pattern. There is urgent need to reveal the transmission of those infectious diseases.

There are several major ways of disease transmission by human coughing, such as inhaling the pathogen-carrying aerosol or direct contact with the deposited coughing droplets. This kind of disease transmission starts from the exhaling of pathogen carrying-agents from an infected person (Cole and Cook, 1998), and then dispersing into the air until finally inhaled by a susceptible person or depositing onto the floor or cloth`ings. Although the coughing-induced disease transmission can spread in both indoor and outdoor environments, the former has a more severe effect than the latter.

The reason for this is the aerosol droplets can rapidly disperse and quickly evaporate to a nonviable stage due to sky/solar radiation (Edwards and Dragsted, 1952). On the other hand, the indoor environment are confined with limited space and low air exchange rate as well as low radiation, and thus may have higher risk for coughing-induced infection transmission (Houk *et al*., 1998; WHO 1998; WHO 1999 and Mangili and Gendreau, 2005). Another reason is that people are spending more and more time indoors, nowadays around 90% of their time (Klepeis *et al*., 2003 and Aliaga and Winqvist, 2003). In some long-distance public transportation environments, such as buses and airplanes, the ventilation on board may enhance the possibility of transmission due to re-used air and long exposure time. Hence, it is important to investigate coughing-induced disease transmission in indoor environments, such as office spaces (Kenyon *et al*., 2000), hospitals (WHO, 1999), and aircraft cabins (WHO, 1998).

For indoor environments, the air flow pattern is dominated by an air-conditioned system design for each specific case. The flow pattern may play a significant role in disease transmission as suggested by others, since it dominates the droplet's trajectory. For airborne droplets, they are more likely following the air flow if they are smaller in size, since the *Stokes* number is smaller. Besides the trajectory, another important aspect is evaporation, which could be quite complicated since many are affected by many factors including temperature, humidity, radiation, and pressure. Pressure is taken into consideration because for some conditions, such as high altitude locations, airplane cabins and the passenger space of future vacuum tube rail transportation such as Hyperloop, the pressure is normally below sea level pressure, which is approximately 1 atmospheric pressure. The evaporation rate might be enhanced under depressurized

conditions (Cheng *et al*., 2016), therefore the pathogen-carrying agents may travel farther as less liquid attached.

Creating a sub-atmospheric pressure environment in a chamber is essential to some industrial processes such as negative pneumatic conveying and vacuum heat treatment. The depressurization can be realized via various pumping techniques (Hanlon, 2003; Chambers, 2005). For this study, the required depressurized environment should include the following features: 1) Capability of being scaled-up. This is due to the comparing to capacity of traditional vacuum technology, indoor environment supposed to be huge, no matter for hospital rooms, buses or aircraft cabins. 2) Open flow environment. Due to the chamber studied here being an environment with air-conditioned and ventilation, the depressurization must be able to operate under an open flow environment, which is a rare application for traditional vacuum technology.

Above mentioned indoor, air-conditioned air ventilation and depressurization are all about the environment, or ambient condition for this study, but the key issue is the cough itself, which dictates the initial condition for the aerosol transport. To provide proper initial conditions, the characteristics of a cough considered in the study should at least include cough velocity, cough duration, volumetric air capacity per cough, total mass of cough droplets per cough, area of mouth opening in coughing and droplet size distributions, etc. The most important factor contributing to cough-induced disease transmission is the characteristics of the droplets, which comes to no surprise if droplets are believed to be the pathogen-carrying agents. Among all characteristics, the droplet size is a crucial factor for the following reasons.

First, different sized droplets are generated from different depths of the respiratory tract as high-speed exhaling airflow skims over the mucus (Ross, 1955; Geng, 1985; Zhang *et al.*, 2015). Although it is difficult to determine the exact origin of expiratory droplets, the assumption that the larger droplets are generated from the upper tract is still widely accepted since the smaller droplets have a smaller *Stokes* number and tend to follow the gas flow more easily. This also indicates that different sized droplets may carry various types and densities of pathogens from the mucus surface of different respiratory tract depths. Second, the spread distance of droplets can be significantly affected by droplet size or its inertia. The coughing-induced disease transmission could be classified as droplet transmission for large droplets and airborne transmission for comparatively smaller droplets, respectively (Gralton *et al.*, 2011). The former usually settles quickly to the surrounding surfaces (such as the ground or clothing) within 1 m from where they were released (Garner, 1996), and the latter may remain airborne for a longer period of time and therefore has a much broader spreading area (Duguid, 1946; Wang *et al.*, 2005; Xie *et al.*, 2007). Third, the droplet size dominates its penetration depth and deposition inside the respiratory tract. Studies show that the smaller droplets are more likely to penetrate deeper into the respiratory tract while the larger droplets are more likely to deposit onto the upper airway surface. The critical diameter, also known as the cut-off diameter, is around 5 to 10 microns (WHO, 2007; Gralton *et al.*, 2011). The penetration distance matters because the possibility and mortality of infection grow as the pathogen deposition site penetrates deeper (Thomas, 2013).

Overall, the smaller droplets are more responsible for the respiratory disease transmission, and the bigger droplets are more responsible for contamination

transmission. Due to their importance, the determination of droplet size and its distribution has been a focus of recent studies (Sze To *et al.*, 2009; Chao *et al.*, 2010). Many studies have agreed that the size of cough droplets have at least two main ranges (Wan *et al.*, 2007; Yang *et al.*, 2007): one group of fine droplets typically from sub-micron to about 5 microns, and the other of coarse droplets from several tens of microns to sub-millimeters.

To determine the aerosol transport, a collection method should be employed. In this study, this collection method is accomplished by a novel breath simulator. As mentioned previously, the coughing-induced disease transmission starts from exhaling of pathogen-carrying-agents from an infected person, and ends at inhaling the aerosol of susceptible person or depositing onto the floor or clothing. The inhaling of aerosol determines what amount of pathogen is a potential risk for a studied individual exposed in such an environment. Similar to coughing, there are major characteristics of breathing, such as breath duration and transient velocity for the design of the breath simulator. The designed breath simulator is able to operate in pair with the cough simulator in the A/C chamber environment. The breath simulator is able to capture the surrounding aerosol similar as functional as human breathing. In addition, the total amount of aerosol capture is quantitatively measured. The breath simulator is portable to be located at any place inside or outside the A/C chamber.

To study the aerosol transport inside an A/C chamber, such a chamber needs to be built in the first place. The dimension of this A/C chamber is carefully selected with the design of air-conditioned system. This chamber should have a typical size for coughing-induced aerosol transporting within (considering a typical size of small school bus,

standard hospital ward or small size bedroom). The reason for the experimental study of aerosol transport in the A/C chamber is to assist numerical simulation, which has many advantages but at the same time it has flaws. The numerical simulation can always provide vivid results as long as the calculation converges. However, due to the current development of computational fluid dynamics theory, physical model selection remains unclear for example for weak turbulence and weak buoyance. In the particular study, the coughing from human mouth and the chamber inlet flow from the A/C system may well fit in the range of weak turbulence, while the temperature difference between the human body and the air around may result in but a weak buoyance. Via the experiment measurement of aerosol transport inside an A/C chamber, a lot of information can be provided to the CFD model for numerical simulation purpose for model selection as well as boundary condition.

Except the experimental approach, many literatures have showed that numerical simulation can be a very fast and efficient way to study the aerosol/particle transport in indoor environment. Both commercial and self-compiled Computational Fluid Dynamics codes are widely used. Unlike the experiments, the numerical simulation has its financially affordable and less time consuming advantages, especially for parametric study of an existed framework. The reason is because it always cost much more time and money to adjust parameters for experiment study. In short, a proper defined CFD model can be a very effective approach to study such aerosol transport problem with good agreement on experiment data (Wan *et al*., 2009; Yan *et al*., 2009 and Zhang *et al*., 2009).

Hence, by studying all the factors above, the aerosol transport by coughing in an air-conditioned chamber will be determined. And a frame work for determining the aerosol fate is established.

1.2 Technical Challenges in the Dissertation

Within this decade, many researchers have studied the coughing-induced disease transmission, but there are still many technical challenges to determine the aerosol transport in the sub-atmospheric pressure air-conditioned chamber. This includes the following aspects: 1) the study of coughing; 2) the collection of aerosol generated by coughing; 3) The CFD simulation; 4) the depressurization and 5) the droplet evaporation.

First, the study of coughing has been conducted by many researchers via experimental approaches. As discussed in the previous section, one of the most important factors is the droplet size. The determination of droplet size and its distribution has been a focus of recent studies (Sze To *et al.*, 2009; Chao *et al.*, 2010). Many studies have agreed that the size of cough droplets have at least two main ranges (Wan *et al.*, 2007; Yang *et al.*, 2007): one group of fine droplets typically from sub-micron to about 5 microns, and the other of coarse droplets from several tens of microns to sub-millimeters. A cough simulator generating such of droplets is defined here as a bimodal cough simulator. The desired characteristics of a bimodal cough simulator should include the following features: coughing duration about 1 s (Wan *et al.*, 2007; Sze To *et al.*, 2009), volumetric air capacity per cough around 0.4 liter (Wan *et al.*, 2007; Sze To *et al.*, 2009), total mass of cough droplets per cough from 6.7 to 75 mg (VanSciver *et al.*, 2011; Sze To *et al.*, 2009), area of mouth opening in coughing from about 2 to 5 cm^2 (Gupta *et al.*, 2009b;

Chao *et al*., 2010; VanSciver *et al*., 2011), coarse droplet size from 100 to 300 µm (Wan *et al.,* 2007), fine droplet size around 5 µm (Wan *et al.*, 2007), the maximum coughing velocity at mouth opening from 1.5 to 30 m/s (Zhu *et al*., 2006; VanSciver *et al*., 2011) and droplet size distributions in probability density function (PDF) over a range from 2 µm to 2 mm (Sze To *et al.*, 2009; Chao *et al*., 2010; Gralton *et al.*, 2011). There have been few reported prototypes of bimodal cough simulators, and none meeting all the desired features above. Lindsley (2013) suggested to use an airbrush to generate coarse droplets and a nebulizer for fine droplets. However, the system was operated either by airbrush or by nebulize but not simultaneously for both. It also failed to give the coughing velocity, which is an important factor for pathogen spreading. Hence, it is a pressing matter to design and build a cough simulator with two size ranges, or bimodal cough simulator.

The measurement of droplet size and its transport is another issue. Some breath simulators have been designed by others or conducted similar research (Noti *et al*.,), some for alcohol breath test (Zhang *et al*., 2014; Kang 2017), but none of the existed design meets the requirement for this study. Some are focusing on lung simulation for the breathing velocity (Cecchini *et al*., 2011; Heili-Frades *et al*., 2007), but not including the aerosol measurement capability.

Most studies use optical methods to determine the size, such as Particle Image Velocimetry (PIV), Laser extinction and Laser diffraction method based on Theory of Mie (Vâjâiac, 2014; Sun *et al*., 2012; Martin *et al*., 2010). However, due to the transparency of the droplet, those methods will inevitably have deflection, reflection, droplets overlapping and/or total reflection since it is an optical measurement, and the

smaller the droplet size the bigger the relative error. To estimate the total amount pathogen transport by the aerosol, the total mass of droplets matters. For a 20% error in droplet diameter measurement, which is already not a low level of accuracy for many droplet optical measurements, the error of droplet mass would be $(1.2^3-1)*100\%\approx72\%$, which is a huge error. Hence, a new experiment measurement of droplet size and number is needed to overcome or at least provide additional validation for the optical methods.

Besides the experimental approach, many literatures have shown that numerical simulation can be a very fast and efficient way to study the aerosol/particle transport in indoor environments. Both commercial and self-developed Computational Fluid Dynamics codes are widely used. Unlike the experiments, the numerical approach has its financially affordable and less time consuming advantages, especially for parametric study of an existing framework, since it always takes much more time and costly to adjust parameters for experimental study. However, CFD also has its own limitations. For example, numerical simulation can always provide vivid results as long as the calculation reaches good convergence. Hence it always recommended be validated. In this particular study, due to the low Reynolds number, the flow field is in a region of weak turbulence, which requires careful selection of a turbulence model. To simulate the aerosol, both Eularian (Mazumdar and Chen, 2008 and Yan *et al*., 2009) and Lagrangian (Wan *et al*., 2009; Zhang and Chen, 2006, 2007) approaches can be used. The previous one is for the particle/droplet concentration, while the latter one is for the transport pattern. For steady state simulation, both approaches show little difference, but for unsteady the Lagrangian provides better prediction (Zhang and Chen, 2007). In addition, the coupled discrete phase modeling should also be dealt with caution, as its trajectory and evaporation could

be significantly different by selecting a different model or User-Defined Function (UDF). A droplet evaporation model uniquely for the aerosol transport with evaporation is recommended. Besides, a latent heat model is proposed to bring on the issue of latent heat partition for the evaporation. Based on our best knowledge, the convection effect is rarely considered and also the latent heat partition on droplet and adjacent gas phase has never been studied. The convection should not be totally ignored without justification, since in this study the droplets evaporating in an air circulating environment. The latent heat study is important (He, *et al*., 2013) here because it may greatly affect the droplet temperature, which dictates the saturation pressure of water vapor at its interface.

The scale-up capable and open-flow depressurization system is another challenge. The depressurization can be realized via various pumping techniques (Hanlon, 2003; Chambers, 2005). Generally speaking, for normal mechanical pumps, the efficiency of vacuum pumping decreases significantly with the depressurization. In addition, the energy cost is expected to be more significant as system size increases. For instance, to vacuum a 30-gallon chamber in a minute (as achieved in this study by condensation), it would require a vacuum pumping capacity of 4 CFM that may be easily available. However, a ten-fold scale-up in size (1000 times in volume) would require a vacuuming capacity of 4000 CFM, which may be manageable by optimized condensation but would be a tremendous challenge and power consumption to vacuum pumping. Open flow system is also difficult to realize, for most vacuum pumps working under close system, but for the air-conditioned chamber environment, the flow has to be open system. One alternative approach for chamber depressurization is by condensation. It has long been

realized that condensation in a chamber prefilled with condensable vapor leads to chamber depressurization, and the condensation rate can be cooling controlled.

Despite the apparently simple concept of depressurization by condensation, understanding of this process for the design and control of such a system is far from complete. While the final state of a cooling-controlled depressurization process can be reasonably estimated based on the thermodynamic equilibrium, the dynamic process of depressurization is not only transient but also in thermal non-equilibrium, which is mainly governed by the rate of condensation. The development of a successful dynamic process modeling requires a deeper understanding with appropriate modeling formulation on many complicated coupling mechanisms such as heat and mass transfer in cooling-controlled condensation, the transient nature of non-equilibrium during the process, the complication by the co-existence of non-condensable gas (NCG) within vapor, as well as the complex geometry and material properties of chamber and cooling device involved. So far, few modeling efforts on this topic have been reported, with none covering all mechanisms mentioned above. For instance, some dynamic process models have been developed for the dynamic characteristics in depressurization by gas discharging out of a pressurized vessel without phase change (Zhou *et al*., 1997); some surface condensation models deal with the coupled mass and heat transfer, yet without the inclusion of NCG (Liu *et al*., 2004) nor under the condition of depressurization (Li *et al*., 2011, Li, 2013). Recently some modeling efforts include heat and mass transfer coupled phase change to study only pressure drop in micro-channels (Heo *et al*., 2013). Few modeling approaches, especially via transient and full-field CFD simulations, on depressurization by condensation of vapors with NCG have been reported.

Droplet evaporation also plays a very important role in aerosol transport. First, the remaining size of the droplet affects its trajectory, and secondly, the water content of the droplet may be critical for pathogen vitality and mortality. The existing droplet evaporation mostly deals with single component diffusion controlled evaporation. Based on our best knowledge, the convection effect is rarely considered and also the latent heat partition on droplet and adjacent gas phase has never been studied. The convection should not be totally ignored without justification, since in this study the droplets evaporate in an air circulating environment. The latent heat study is important here because it may largely affect the droplet temperature, which dictates the saturation pressure of water vapor.

1.3 Dissertation Structure and Approaches

In this study, a bimodal cough simulator has been designed, constructed and calibrated to meet the basic ranges of listed features. Our cough simulator consists of a pressurized gas tank, a nebulizer and an ejector, connected in series. It produces coughing gas and droplets through the coordinated action of pressurized gas and droplet generators: the fine droplets by a nebulizer and the coarse droplets by a venturi ejector. The coughing frequency and duration are controlled by programed solenoid shut-off valves. The spray velocity is determined by a dual-beam cross-correlation velocimeter whereas the volumetric air capacity per cough is calibrated by a thermodynamics method over the gas released from compressed gas tank. To calibrate the coarse droplet size PDF, a fibrous collector and image analysis system is employed. To account for the changes in spray characteristics between the spray nozzle exit and the fibrous collector, a parametric

model is established to assess the hydrodynamic effects such as spray evaporation and polydispersion. This parametric modeling is a set of ODEs one-way coupled with a full-field CFD simulation to calculate evaporation and trajectory. The evaporation is modified by a diffusion boundary layer factor. The ambient condition of this parametric model is provided by the numerical simulation, which is performed with the aid of Ansys FLUENT 12.1®. The measured size distributions of coarse droplets are reasonably represented by the Rosin-Rammler distribution in probability density function (PDF), which leads to a bimodal distribution from the overlap with the fine droplet distributions calibrated by the nebulizer manufacturer.

To determine the droplets fate, a breath simulator has been design and built. This device can simulate both inhaling and exhaling by an integrated system of combining two different flow direction one-way duct with a shared opening exit, which plays the function of mouth. The flow is generated by an in-line blower, and the flow velocity and direction can be controlled and switched by a computerized valve system, which consisted of solenoid valves and a reversing valve. To measure the total mass of aerosol inhaled by the breath simulator, a fibrous collector has been mounted inside the mouth section of the breath simulator. A specific design has been made for the mouth section to avoid the blowing effect of exhaling on the fibrous collector. The solution of the saliva for the droplets composes of sodium chloride (NaCl). The collected sample then would be dissolved into distilled water, and then measure by solution conductivity meter to determine the amount of NaCl it collects. Thus, the total amount of inhaled droplets can be found out based on the solution NaCl concentration.

A chamber with dimensions of 7 x 8 x 10 ft. has been designed and built to measure the aerosol transport. The air-conditioned system has been implemented into the chamber. It has three inlets and three outlets. The air circulation rate can be as high as 40 ACH, and the temperature can be controlled to 13 °C the lowest. So far, four chairs have been placed in the chamber, which will be used to simulate as many as four people sitting inside. The cough and breath simulation will be taken into the chamber system and measurement will be conducted.

To provide detailed mechanistic understanding and insights essential to the optimal design and operation of the depressurization by cooling-controlled condensation, a depressurization experimental system by cooling and condensation of pre-filled steam in a confined vessel has been designed. The experiment provides sets of data for both mechanistic understanding and validations of our proposed models. A parametric model consisting of a set of coupled ordinary differential equations has been established, which helps to reveal various parametric effects on the depressurization process. The simplified assumptions in the parametric model include the lumped heat capacity approximations for chamber walls, cooling coils and the gas phase. To further quantify the thermal non-equilibrium characteristics of the dynamic process, a transient and full-field simulation of computational fluid dynamics (CFD) has also been conducted. One important step in the CFD modeling is to development of an appropriate boundary condition on cooling coil surfaces where condensation occurs, which is then implemented through a User-Defined Function (UDF) into the commercial code ANSYS FLUENT. While the majority of gas component in the chamber is condensable steam vapor, there also exists a small amount

of air residue in the gas phase. Hence, both parametric and CFD models regard the gas phase as a mixture of condensable vapor and non-condensable gas (air in our case).

To more efficiently and cost-effectively analyze the pathogen-carrying aerosol transport in this depressurized air-conditioned chamber, a full field numerical simulation has been conducted. This CFD modeling has exactly the geometry of the experiment testing chamber. The simulation is using commercial software ANSYS FLUENT, a Eularian-Lagrangian approach is used. The gas (air-water vapor mixture) and liquid (droplet) phases are treated as continuous and discrete phases, respectively. Different turbulence models have been tested. The evaporation model is set as multi-component with non-evaporative residue model.

The multi-component, diffusion controlled and convection assisted droplet evaporation model is based on traditional d^2–low model. Using boundary layer analysis, the diffusion boundary layer is introduced as a convection factor. The latent heat partition has been discussed and analyzed. This evaporation model will be implemented to the CFD model via User-Defined Function.

1.4 Remaining Challenges and Future Directions

The remaining challenges include the experiment calibration of breath simulator, the measurement of the integrated chamber system with both cough and breath simulators, the parametric study of CFD simulation under different conditions such as different total air circulation per hour (ACH), coughing injection velocity, angle, as well as different turbulence modeling. Other remaining challenges include studies such as better droplet evaporation model and latent heat partition analysis.

The future direction for this study is to link the aerosol transport results with medical model to study the comprehensive model of possibility for coughing-induced disease transmission. Another direction is the large scale open flow system depressurization system, which could be applied on future transportation technology, such as vacuum tube bullet train.

CHAPTER 2

DESIGN AND CHARACTERISTIC DIAGNOSIS OF A BIMODAL COUGH SIMULATOR

2.1 Introduction

Coughing has been studied as a challenging subject (Shaker, M., 2008, Taylor, D.R., 2012, Dryahina, K., 2010), and the urgent need to study coughing for revealing the routes of transmission of those infectious diseases transmission has been discussed in Chapter 1 with though literature survey. This chapter provides details of the bimodal cough simulator for its design, fabricate and calibration to meet the basic ranges of listed features. Our cough simulator consists of a pressurized gas tank, a nebulizer and an ejector, connected in series. It produces coughing gas and droplets through the coordinated action of pressurized gas and droplet generators: the fine droplets by a nebulizer and the coarse droplets by a venturi ejector. The coughing frequency and duration are controlled by programed solenoid shut-off valves. The spray velocity is determined by a dual-beam cross-correlation velocimeter whereas the volumetric air capacity per cough is calibrated by a thermodynamics method over the gas released from compressed gas tank. To calibrate the coarse droplet size PDF, a fibrous collector and image analysis system is employed. To account for the changes in spray characteristics between the spray nozzle exit and the fibrous collector, a parametric model is established to assess the hydrodynamic effects such as spray evaporation and polydispersion. This parametric modeling is a set of ODEs one-way coupled with a full-field CFD simulation to calculate evaporation and trajectory. The evaporation is modified by a diffusion boundary layer factor. The ambient condition of this parametric model is provided by the

numerical simulation, which is performed with the aid of ANSYS Fluent 12.1®. The measured size distributions of coarse droplets are reasonably represented by the Rosin-Rammler distribution in probability density function (PDF), which leads to a bimodal distribution from the overlap with the measured fine droplet distributions by the laser diffraction sensor of Sympatec® HELOS/KR.

2.2 Experiment System

2.2.1 Overview and Key Components

The entire experiment system has three sub-systems, namely, the bimodal cough simulator with a control unit, a velocity measurement system, and a droplet sizing system, as shown in Figure 2.1.

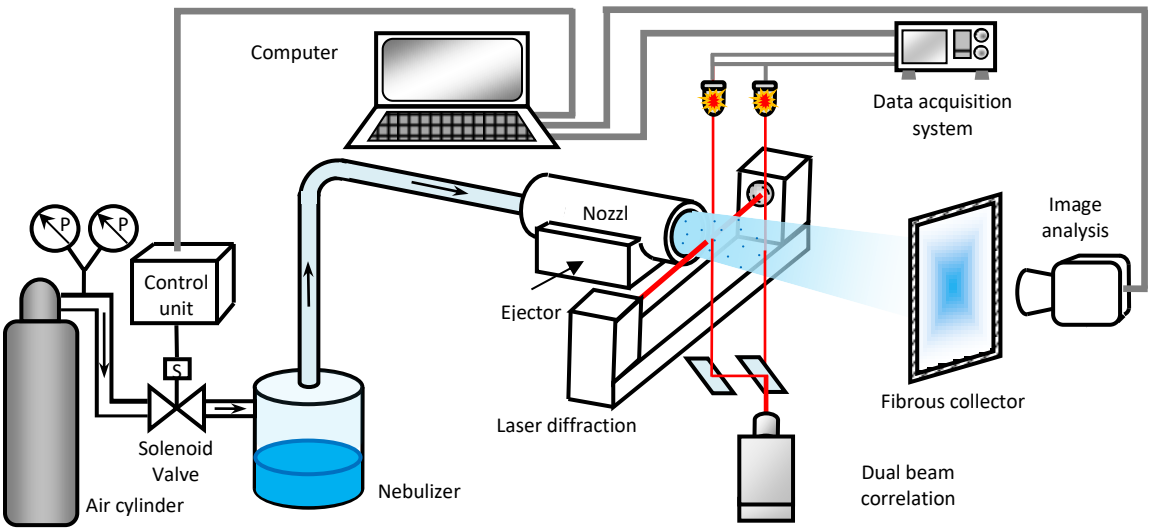

Figure 2.1 Schematic diagram of the experiment system.

The cough simulator consists of a pressurized gas tank, a nebulizer and an ejector, connected in series. The cough air flow is supplied by the pressurized gas tank. The fine

droplets are generated inside a cylinder container by a nebulizer (Mistmakerworld®, MDC01). The coarse droplets are generated by an ejector.

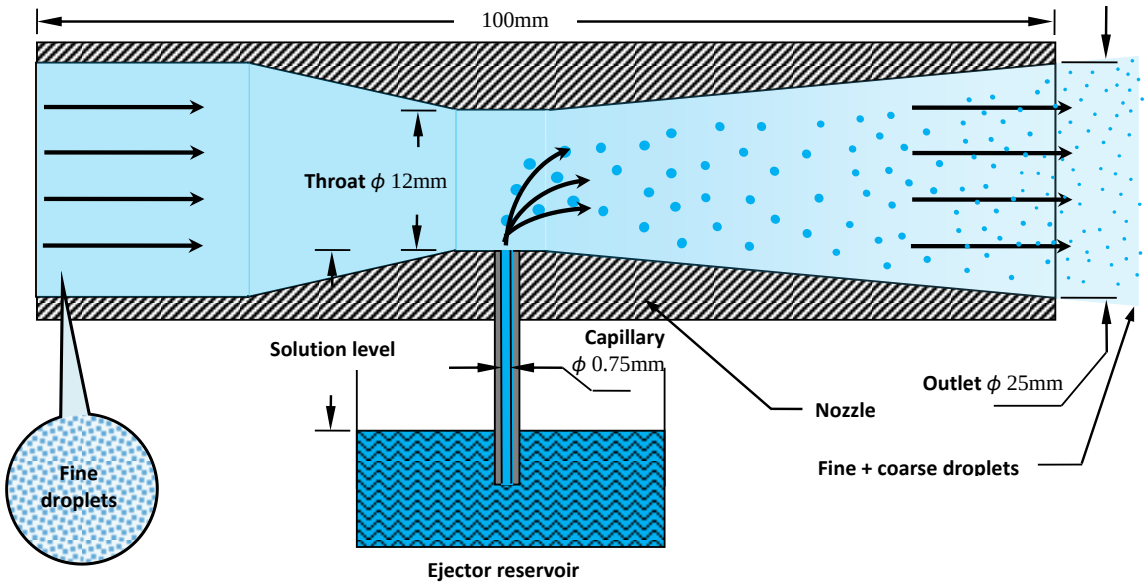

Figure 2.2 Schematic diagram of ejector.

The core of our design is a coarse droplet generator, which is an ejector composed of a venturi nozzle and a reservoir. As shown in Figure 2.2, the coughing air with fine aerosol droplets flows through the venturi nozzle. The solution is sucked up from the reservoir by the negative gauge pressure at the venturi throat, and consequently broken into liquid segments or coarse droplets by the passing air steam. The hydrophobic material of our ejector minimizes the liquid attachment of the solution sucked from the ejector reservoir. For the air humidity of flow, due to the intermittent but repeated generation of fine droplets and breaking up of coarse droplets, the relative humidity of the jet flow is close to saturation. To match with the human body temperature (37 °C), the temperature of the jet flow is controlled between around 35-40 °C by heating the

nebulizer. Some operation conditions and nozzle design dimensions are critical to the droplet generation, including but not limited to: the gas pressure from the air cylinder (around 10kPa), the solution level in the ejector reservoir (7-10mm), as well as the diameters of nozzle outlet (25mm), nozzle throat (12mm) and the capillary (Φ=0.75mm) at throat, as shown in Figure 2.2. A schematic diagram of the cough simulator is shown in Figure 2.3.

The coughing frequency and duration are controlled by programed solenoid shut-off valves. The process logic operations are shown in the Figure 2.4. Based on the published data (Wan et al., 2007; Sze To et al., 2009), each coughing duration is set to be 1 second with an interval of 3 seconds between coughs. The periodic repeated coughing is achieved by automatically switching on/off of the solenoid valve (Grainger, P251SS-120-A), where the whole control system is consisted of an electrical counter, a repeat cycle timer, a time delay relay and a solenoid valve. The dimensions of this cough simulator is about 800x300x300mm, which is much smaller than the one from Lindsley (2013), which is about 1500x700mm (2-D projection). The cough simulator supporting structure is made of steel, the nebulizer container is made of acrylic, and the nozzle is produced by 3-D printing using acrylonitrile butadiene styrene. Other design dimensions can be referred in the Supporting Information, such as in Figure 2.3. The saliva is made of distilled water, glycerin and sodium chloride with a mass ratio of 1000:76:12, referring to the mucus content reported in Nicas et al. (2005). For coarse droplets, we use pure fountain pen ink to replace distilled water. The density of the ink is found to be very close (994 kg/m3) to pure water.

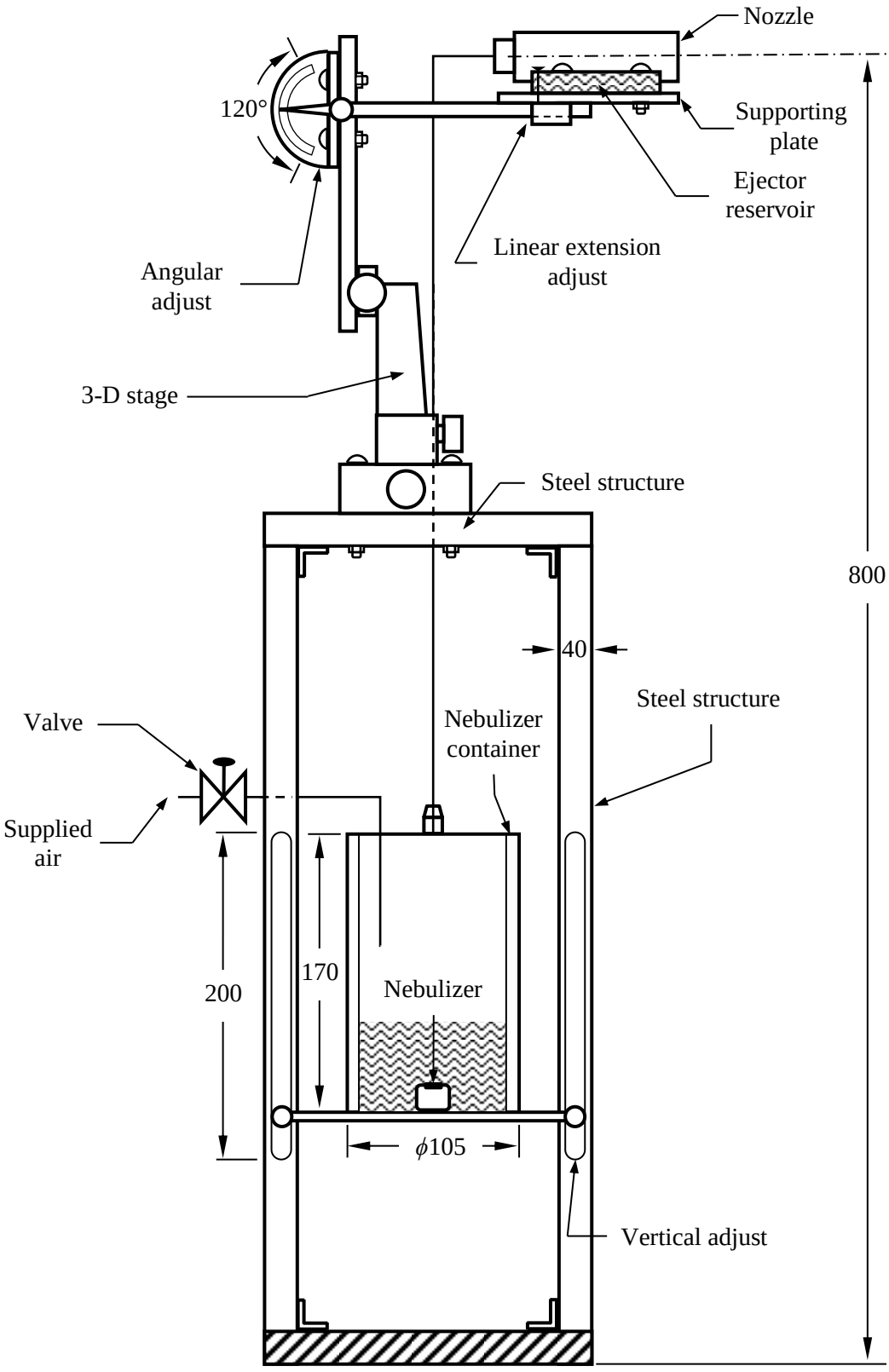

Figure 2.3 Schematic diagram of the cough simulator with major dimensions. (mm)

2.2.2 Control System

The volatile is hard to obtain from the manufacturer, but from our experiment observation that the ink evaporates slower than the distilled water, which makes the volatile property less important since the evaporation model in the later section already shows the evaporation can be ignored for the coarse droplets. There are several limitations of this cough simulator. Firstly, all surfaces are rigid without any surface vibration (which is different from actual human throat, especially during coughing, that the surface vibration can be a major source of droplet generation). Secondly, no special surface coating is applied so that the surface of 3-D printed module may not be hydrophilic at all.

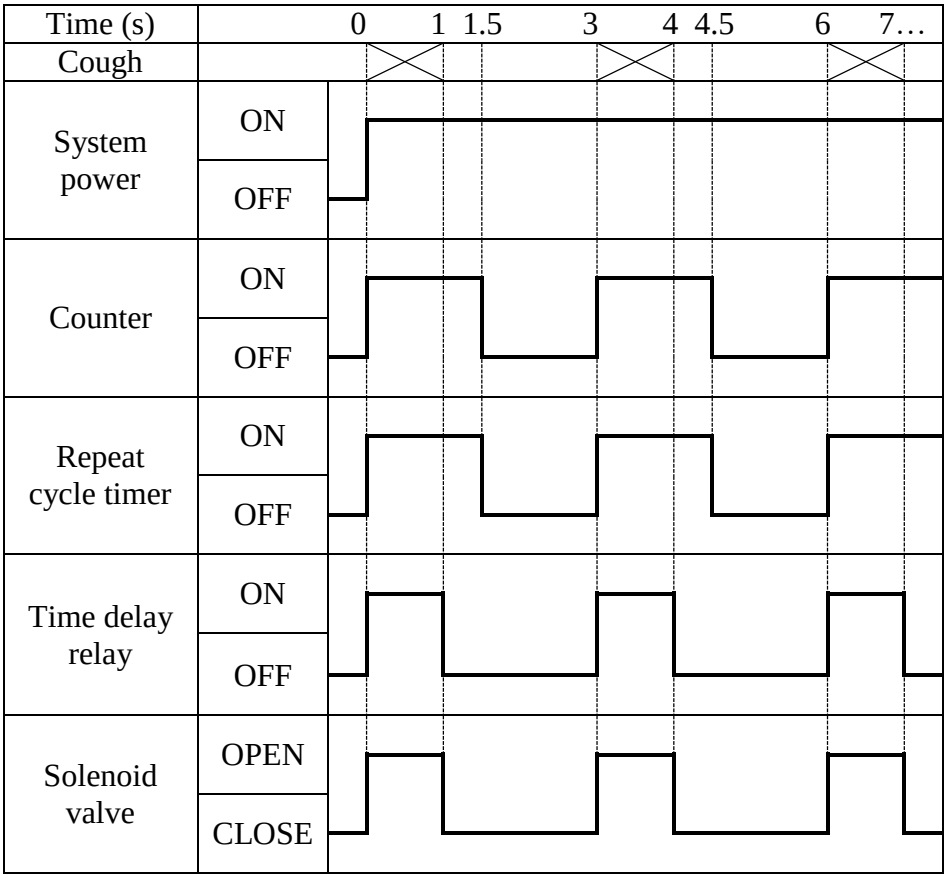

Figure 2.4 Process logic operations of control unit.

2.3 Characterization and Measurement Method

The characterization of this cough simulator includes the determination of coughing velocity, coarse and fine droplet size and size distributions, and air volume per cough. The air flow released per cough can be readily determined thermodynamically over the gas released from compressed gas tank. The averaged air volume per cough is calculated based on the total pressure difference of the air cylinder before and after the experiment, the pressure regulated for air release, and the total number of coughs. The determination of coughing velocity and droplet size are explained in detail below.

2.3.1 Coughing Velocity

The velocity of coughing is difficult to be determined. This is because the transient and non-uniform release of air per cough makes the common "steady-state" types of velocity measurement techniques, such as laser Doppler velocimetry (LDV) and pitot-tube method, inapplicable to our case. Some common "instant-velocity" measurement techniques, such as hot-wire anemometry (HWA) and particle-image velocimetry (PIV), also fail to be applicable. The hot-wire anemometry, whose measurement principle is based on the empirical correlation of convective heat transfer coefficient to Reynolds number over a cylinder, may not be accurate in the presence of fine and coarse droplets from the coughing. The traditional PIV, requiring the temporal tracking of fine droplets in a two-dimensional plane (typically illuminated by a laser sheet), may have difficulties in field and time-domain resolutions, in addition to the required synchronization with the coughing. It is realized that some advanced PIV systems can reach kHz time resolution and the Volumetric Velocimetry (3-D PIV) can also provide certain capability of

capturing a 3-D flow field. However, considering the overall constrains (with respect to the wide ranged droplet size and transient velocity) in size of view field of measurement, spatial resolution, time resolution, synchronization, and other limitations in real-time digital image process, in addition to the facility cost, 3-D PIV may not be an effective or realistic choice for the measurements in this particular application.

The dual-beam cross-correlation method (Zhu *et al*., 1991), which is also economically viable, can be used to characterize the coughing velocity. The basic principle is to best correlate the time-shifting of light scattered by non-uniformly-distributed tracers (droplets in our case) over a given distance along their trajectory path. As shown in Figure 2.5, a laser beam is split by a 50-50 reflection and penetration mirror, and one of two split beams goes through a full-reflection mirror. Thus, a single laser beam becomes two parallel beams. The two laser beams are set at a given separation distance (3 cm in this case) along the spray path close to the nozzle opening (1 cm away in this case). The laser beams are received by two photodiodes, respectively, with light intensity converted into electric signals in terms of current or voltage. During a cough simulation, the transient flow with a mist of fine droplets generated by the nebulizer is flushed out of the nozzle. The change in intensity is then affected by the light scattering by aerosols (mostly droplets) passing through the beams. The received signal from photodiodes is analyzed by cross-correlation method to determine the distance-averaged transient coughing velocity.

The measured coughing velocity most likely represents that of fine droplets, which is also assumed to be the same as gas velocity. This non-slip in velocity between fine droplets and air can be justified since the size of the fine droplets is very small,

which is validated by the laser diffraction measurement, and the corresponding Stokes number (*Stk*=0.154) is much less than unity. The coarse droplets, once passing through the laser beam, also generate light scattering. However, their contribution to the light scattering is believed to be low due to the scarcity in total number of coarse droplets generated per cough, the low fraction of surface area among all droplets, and the wide dispersion in space by their inertia-driven trajectories.

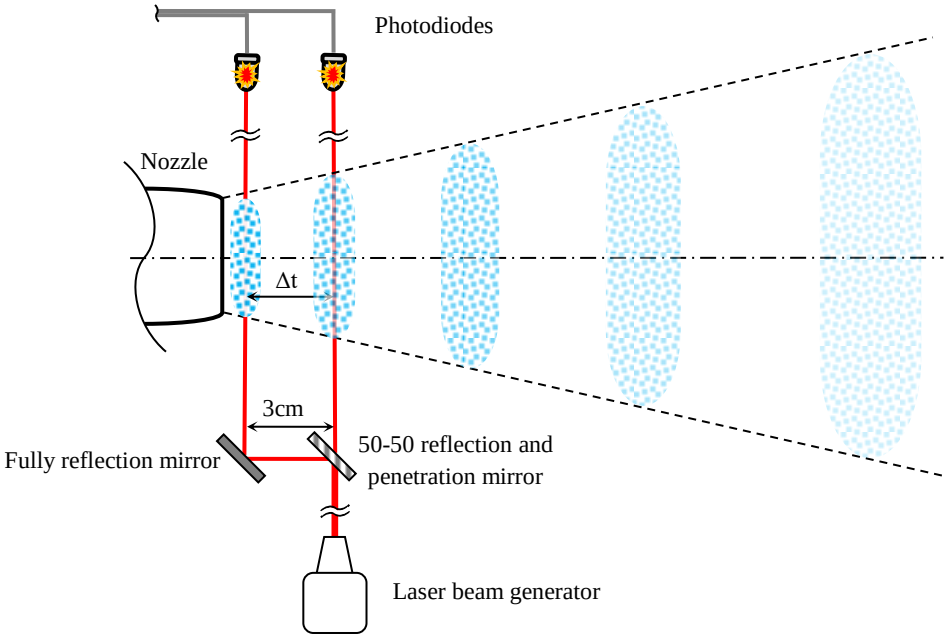

Figure 2.5 Velocity calibration by dual beam cross-correlation system.

Based on the large size of coarse droplets (a few hundred microns), the direct measurement for velocity of coarse droplets may be achievable by image-streaking technique in an illuminated plane (typically by laser sheet). However, the number of coarse droplet generated per cough is too scarce, and the wide dispersion in space makes the image capture and streaking track in a 2-D plane to be very difficult if not impossible. Hence in this study, the velocity of coarse droplets is indirectly estimated by the

acceleration of coarse droplets from their formation site (location of sucking channel from reservoir inside ejector) to the nozzle opening, driven by the coughing air.

2.3.2 Coarse Droplets Size vs Number Distribution Calibration

Our cough simulator has two distinctively different mechanisms for droplet generation: fine droplets generated by ultrasonic membrane vibration in a nebulizer, and coarse droplets generated by flow instability and shearing in the nozzle ejector. Based on our measurements, there is little overlap in size range between fine droplets and coarse droplets. The fine droplet size and size distributions are measured by the principle of laser diffraction using a commercial instrument (Sympatec®, HELOS/KR) at the outlet of nozzle, whereas the coarse droplet size and its size distribution are determined by a fibrous collector and image analysis system developed in this study. The HELOS/KR has a measuring range of 0.1-8790 μm, and the absolute accuracy is typically within ±1%. The measurement setup is illustrated in Figure 2.1. The following is focused on the design and measurement principles of our method for the size determination of coarse droplets by coughing.

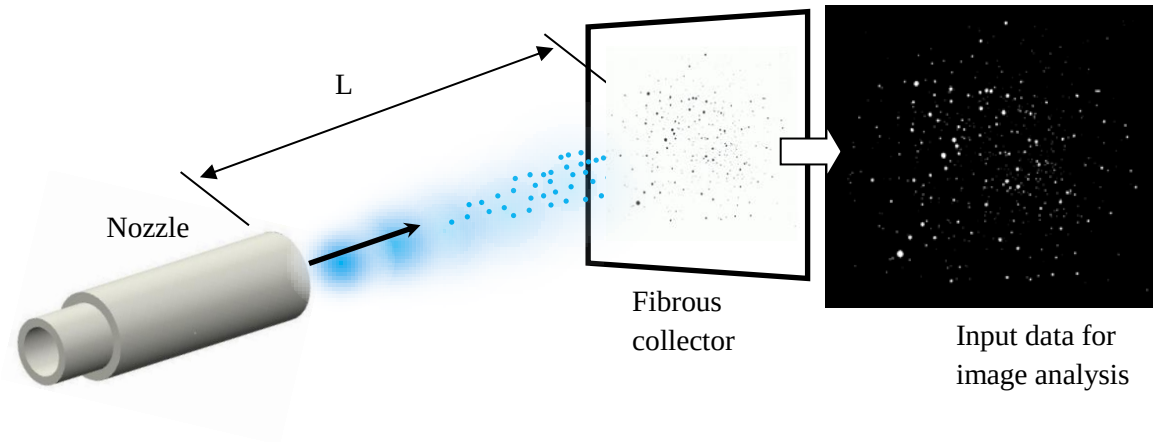

Figure 2.6 Self-compiled image analysis program.

Figure 2.6 shows the schematic diagram of a collector of coarse droplets and the subsequent image of wetted spots for droplet size analysis. This collector of coarse droplets is a water-absorbing paper made of hydrophilic fibers (in our case, we use a reed-based calligraphic paper, DoubleDeer®, Xuan). To enhance the visibility for image analysis, some dyes (fountain pen ink) are added into the cough liquid. The fibrous collector is located in front of the nozzle opening at a short distance L, which is designed to allow the fine droplets to be averted from direct collision while trap the coarse droplets by inertia impaction without overlapping of collected coarse droplets. The size of collector is also large enough to capture all coarse droplets. The captured droplets are soaked into the collector by the capillary effect but kept locally by the surface tension. The image of wetted spots is then digitally analyzed to yield droplet size and size distributions.

The image analysis method is based on the mass conservation of individual droplets and the total mass conservation. As schematically shown in Figure 2.6, once a droplet is collected and soaked into the fibrous collector, the spherical shape of droplet

becomes a round disc, with a typically slightly larger wetted image (A_a) on the collision-front surface and a slightly smaller area (A_b) in the back surface. For the *ith* droplet, we have

$$m_i = \rho_d \alpha_i \delta_i A_i \equiv K_i A_i \tag{2.1}$$

where m, δ, α, A and ρ represent mass, thickness, voidage, droplet soaking area and density of droplet, respectively, and the area A_i is given by

$$A_i = \left(\frac{A_{iA} + \sqrt{A_{iA} A_{iB}} + A_{iB}}{3} \right) \tag{2.2}$$

where A_{iA} and A_{iB} are two size of the paper. Consequently, the total mass of collected droplets can be determined by:

$$\Delta m_T = m_{T1} - m_{T0} = \sum_i m_i = \sum_i \rho_d A_i \delta_i \alpha_i \tag{2.3}$$

where the subscript *T*, *0*, *1* stands for total, before and after the collection, respectively. Assuming thickness δ and voidage α of the fibrous collector are constant, and the density of droplet is known (which can be measured easily), the equation (2.3) becomes:

$$\Delta m_T = \rho_d \bar{\delta}_i \bar{\alpha}_i \sum_i A_i = K A_T \tag{2.4}$$

where the parameter can be easily determined by the measured total mass and wet area:

$$K = \frac{\Delta m_T}{\sum A_i} \tag{2.5}$$

For a single droplet, its mass can be determined by individual wet area and parameter *K*:

$$m_i = \frac{\pi}{6} d_i^3 \rho_d = K A_i \tag{2.6}$$

Thus, combining (2.5) and (2.6), the size of a single droplet can be correlated by the total mass, individual wet area, and liquid density by:

$$d_i = \sqrt[3]{\frac{6\Delta m_T}{\pi \rho_d}\left(\frac{A_i}{\sum A_i}\right)} \tag{2.7}$$

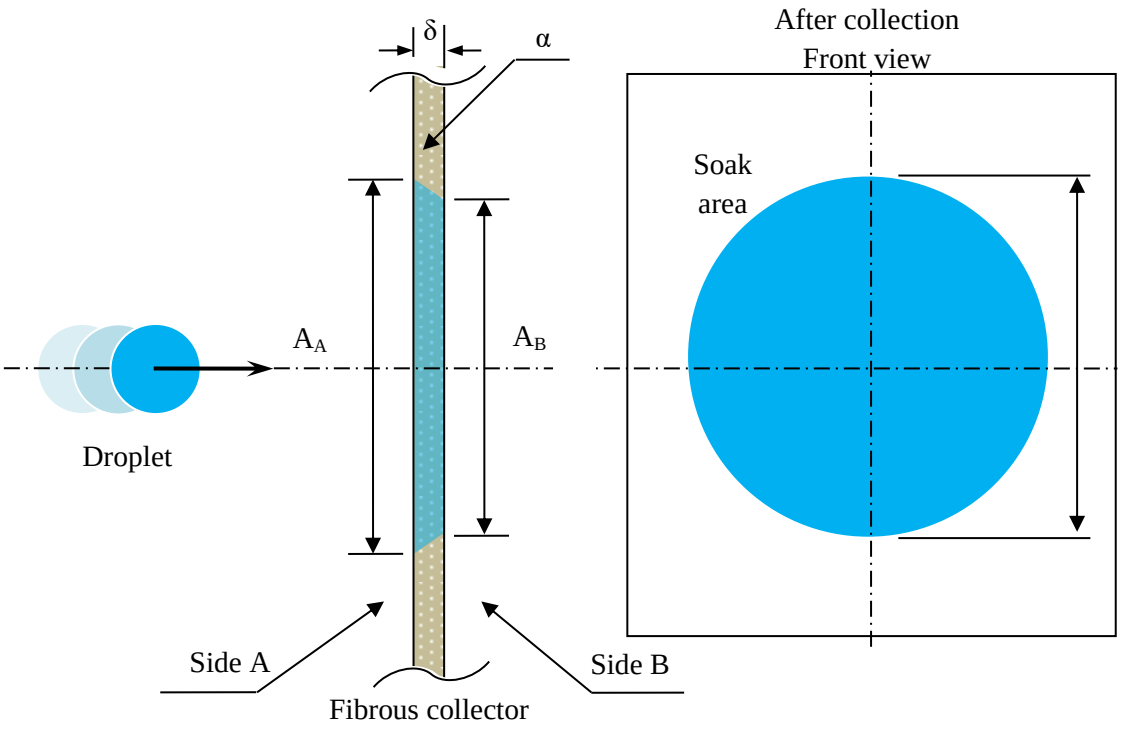

Figure 2.7 Image definition of soaked droplet on fabrous collector.

Consequently, the size distribution can be obtained by including all droplet sizes. Each and every wet areas A_i can be analyzed by a self-developed image analysis program.

The developed method above is based on an important assumption that no droplet break-up or rebounding by the impingement of droplets on the fibrous collector. To verify this, a calibration using a dripping-tube has been conducted, as shown in Figure 2.8. The height of dripping should exceed the distance required to generate the equivalent impact velocity by gravity, which is a convenient approach under the condition that the impact velocity is less than the terminal velocity of the droplet. For the size range of droplets in this study (up to 700 μm from our measurements), the terminal velocity is up to 3 m/s, which is comparable to the measured impact velocity of coarse droplets on the

fibrous collector. The corresponding height of dripping is less than 2 m. Hence, we performed the test with a height range between 0.5 m and 2 m.

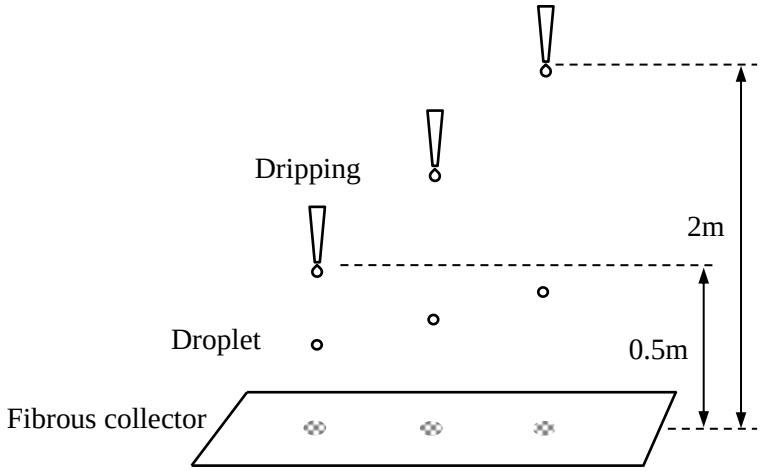

Figure 2.8 Testing of droplet splashing and breaking.

The results of this experiment show undetectable droplet breaking and splashing, even with the dripping of 1-2 mm droplets. Hence, the effect of bounce-back or break-up of droplets is considered to be extremely insignificant under our current experiment conditions. The comparison between the droplet mass calculated by (2.6) and its true mass shows a good match with very minor discrepancy (<1%). The uniformity in *K* value of the fibrous collector and the direct comparison between true droplet size and the size calibrated by the proposed method have been presented in the section of 2.5 Results and Discussion.

While the fine and coarse droplets are very much independently generated by nebulizer and ejector, respectively, there could be some coupling effects such as coagulation of fine droplets into larger droplets or break-up of coarse droplets. However, the coagulation of fine droplets can be ignored here. This is because, to form a coarse

droplet of 50 μm (lower bound in coarse size distribution) from the coagulation of 5 μm (medium-size) of fine droplets, it would require a continuous collision of about 103 times, which is nearly impossible with our low volumetric concentration of fine droplets and very low relative velocity among the fine droplets to make such collisions. The break-up of coarse droplet, if any, would likely to be at the same order of magnitude of the original mother droplet, i.e., the daughter droplets are unlikely to be in the same size range of fine droplets, nor would affect the mass conservation of coarse droplets if some break-up are indeed in the size range of fine droplets. Hence, the coupling effects on mass or size redistribution of fine droplets and coarse droplets are neglected in both modeling analysis and experimental data analysis.

In our study, each collector is used for only one cough sample, hence it is unlikely to have the sever overlapping of droplets, especially with a sampling distance far enough from the coughing nozzle origin ($L/D > 10$). Another concern is the effect of droplet evaporation during the droplet travels between the nozzle exit and the fibrous collector. The evaporation effect, which turns out to be insignificant in our study, will be detailed in the following section.

2.4 Evaporation on Droplet Evaporation

In the previous section introduces a method to determine the size and size distribution of droplets collected at the distance of L from the nozzle. The question is: how does the droplet evaporation affect the droplet size at the nozzle exit by the droplet size measurement at a downstream distance? Since a direct measurement of this evaporation effect is very difficult, we adopt a modeling approach. The modeling effort also helps to

determine the required size of droplet collector to be used in the experiment. The detailed derivation is explained in Chapter 6.

Due to the transient nature of coughing (Zhu *et al*., 2006; Chao *et al*., 2010; VanSciver *et al*., 2011), the ambient gas velocity and humidity of each individual coarse droplet have to be obtained through a CFD simulation. This transient, multi-component and turbulent flow is simulated between the mouth and the droplet collector, using ANSYS Fluent 14.5. Specifically, the species transport model is set active for the gas mixture of air and water vapor. The turbulence model is selected as realizable k-ε model, for its accurate prediction for spreading rate of round jets (ANSYS Inc., 2009). For simplification, the coughing is regarded as axisymmetric. In addition, the contribution of fine droplets evaporation to the ambient humidity is ignored. This assumption is not only for simplifying our simulation but also for allowing the maximum evaporation of coarse droplet in a drier environment without the humidification from fine droplet evaporation. The impact of ignoring fine droplet evaporation to the ambient gas velocity is considered small due to the insignificant amount of fine droplets in mass (<1%) comparing to that of gas per cough.

The simulation domain includes a mouth opening and a trap surface to represent the fibrous collector, with all geometric dimensions identical to those in the experiment. The total cell number of mesh is 4900. A grid-independency study of 14,200 cell shows almost identical result of flow field and the biggest difference of cough flow entrainment area is less than 3%. Thus, the cell number is chosen as 4900 in this study. A summary of model selection, boundary condition, initial condition and governing equations are listed as Table 2.1. Such combined approach of CFD and experiment measurements may also

be an effective method to obtain a reliable flow field in determining dispersion characteristics, especially for a transient flow such as coughing.

Table 2.1 Details of CFD Model

CFD model selection	
Steady/Unsteady	Unsteady
Geometry	2-D axisymmetric
Turbulence model	Standard *k*-ε
Multi-component model	Species transport
Boundary conditions	
Nozzle opening	Velocity inlet (10m/s)
Trapping paper	Wall (Standard wall function)
Default condition	Pressure outlet (P_{gauge}=0)
Initial conditions	
Temperature	298 K
Multi-component model	50% Relative Humidity
Major governing equations	
Continuity	$\frac{\partial}{\partial t}(\rho Y_i) + \nabla \cdot (\rho \mathbf{U} Y_i) = -\nabla \cdot \mathbf{J}_i$
Momentum	$\frac{\partial}{\partial t}(\rho \mathbf{U}) + \nabla \cdot (\rho \mathbf{U}\mathbf{U}) = -\nabla p + \nabla \cdot \boldsymbol{\tau}$
Energy	$\frac{\partial}{\partial t}(\rho E) + \nabla \cdot \left[\mathbf{U}(\rho E + p)\right] = \nabla \cdot \left[k \nabla T - \sum_i h_i \mathbf{J}_i + (\boldsymbol{\tau} \cdot \mathbf{U}) \right]$
Diffusion flux	$\mathbf{J}_i = -\rho D_{i,m} \nabla Y_i$
Turbulence k	$\frac{\partial}{\partial t}(\rho k) + \nabla \cdot (\rho k \mathbf{U}) = \nabla \cdot \left[\left(\mu + \frac{\mu_t}{\sigma_k} \right) \nabla k \right] + G_k + G_b - \rho \varepsilon - Y_M$
Turbulence ε	$\frac{\partial}{\partial t}(\rho \varepsilon) + \nabla \cdot (\rho \varepsilon \mathbf{U}) = \nabla \cdot \left[\left(\mu + \frac{\mu_t}{\sigma_\varepsilon} \right) \nabla \varepsilon \right] + C_{1\varepsilon} \frac{\varepsilon}{k} (G_k + C_{3\varepsilon} G_b) - C_{2\varepsilon} \rho \frac{\varepsilon^2}{k}$

2.5 Results and Discussion

2.5.1 Calibration for Measurements of Coarse Droplets

The calibration of coarse droplet measurement is performed using a dripping tube experiment in which the mass of individual droplet and the corresponding wetted areas on fibrous collector can be independently measured. This experiment is designed to

check the possibility in droplet bounce or break-up during the droplet collection, the uniformity in K, and the calibration of droplet size.

It is noted that the accuracy of our proposed method is closely related to the uniformity in K value, where K is defined as the product of droplet density, thickness and porosity of fibrous collector. To check this, a number of droplet collection locations on the fibrous collector have been randomly chosen so that the individual K_i (from equation 2.1 or 2.6) of the i^{th} droplet location can be calibrated in terms of ratio of K_i over the averaged K value (from equation 2.5), as illustrated in Figure 2.9. This sample calibration shows that the individual K_i value is reasonably uniform, with a discrepancy within 7% to the averaged K value.

The true droplet size of an individual droplet is obtained, based on equation 2.6, from the measurement of mass of that droplet. The collected droplet size of the same individual droplet is calculated, based on equation 2.7, from the measurement of overall mass of all droplets, wetted area of the individual droplet in concern, and wetted areas of all droplets collected. A direct comparison between the true droplet sizes and those calculated is illustrated in Figure 2.10, which shows a very good agreement with a discrepancy less than 2.5%.

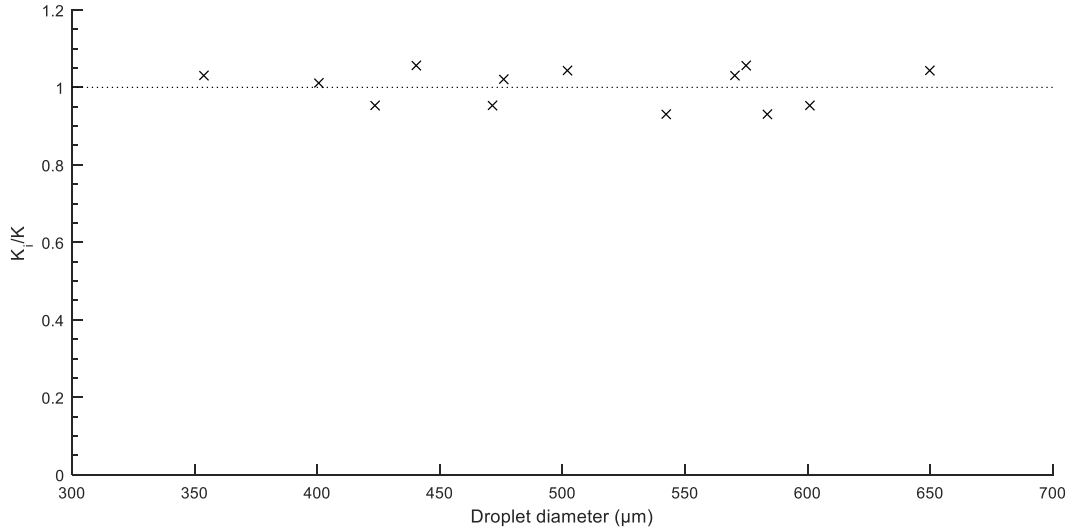

Figure 2.9 Calibration of K uniformity.

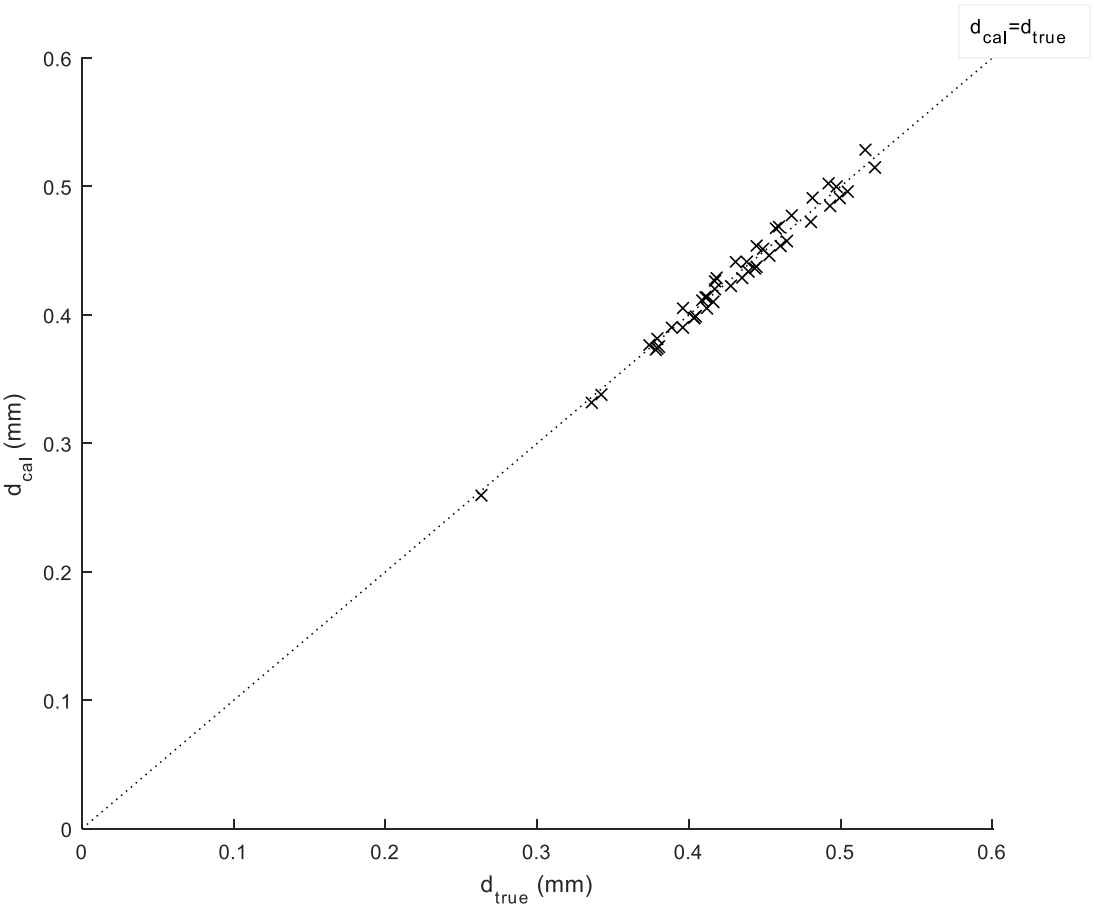

Figure 2.10 True droplet size vs calculated droplet size.

2.5.2 Calibration in Coughing Characteristics

Table 2.2 lists the major coughing parameters calibrated in this study in comparison with those reported from literatures. These parameters include the coughing duration, volume capacity per each cough, total mass/volume of cough droplets per cough, area of mouth opening, size range of coarse droplets, size range of fine droplets, and maximum coughing velocities of gas and droplets at mouth opening. The comparison in Table 2.2 shows the major coughing parameters of our designed coughing simulator match quite well to most of the reported data. For instance, from the experiment measurement of more than 10 times of test runs for the dual-beam correlation velocimeter, the velocity of this cough simulator has a range of 5.3-10.6 m/s, which is within the range of reference data (VanSciver *et al*. 2011, Zhu *et al*. 2006). As for the coarse droplets velocity, it has the range of 1.9-4.2 m/s in accordance of the gas-phase velocity (5.3-10.6 m/s). The range for the velocity of the cough simulator can be further expanded upon specific application. The volume capacity is measured from 0.25 to 3.82 L/cough, which covers the reference data (Wan *et al*. 2007, Sze To *et al*. 2009, Gupta *et al*. 2009b). The references also show this volume capacity varies significantly among different subject, such as different gender, age, or simply different individual. Overall, our simulator provides the most complete features in the coughing characteristics, with a dual-size distribution of droplets.

Table 2.2 Major Coughing Parameters

Reference	Δt (s)	ΔV_{air} (L)	Δm_d (mg)	A_{mouth} (cm^2)	$D_{d,big}$ (μm)	$D_{d,small}$ (μm)	$u_{j,max}$ (m/s)	u_d (m/s)	droplet size range (μm)
Duguid 1946	-	-	-	-	-	-	-	-	5-2000
Wan *et al.* 2007	1	0.4	-	-	137.5	45	-	-	-
Chao *et al.* 2010	-	-	-	1.77	-	-	-	-	2-2000
VanSciver *et al.* 2011	-	-	6.7	3.5	-	-	1.5-28.8	-	-
Zhu *et al.* 2006	-	-	-	-	-	-	6-22.0	-	-
Sze To *et al.* 2009	1	0.4	75	-	-	-	-	-	2-2000
Gralton *et al.* 2011*	-	-	-	-	-	-	-	-	<0.1-500
Gupta *et al.* 2009b	-	0.25-1.6	-	m:4±0.95 f:3.37±1.4	-	-	-	-	-
This study	1	0.25-3.82	10.2-53	5	77-737	1-16	5.3-10.6	1.9-4.2	1-737

2.5.3 CFD Results and Impact of Droplet Evaporation on Size Measurement

Figure 2.11 shows the velocity vector and mass fraction of water vapor. It can be observed that the jet flow reaches the trap wall in about 0.05 s. Based on the CFD results of velocity and mass fraction of water vapor in the mixture, these parameters could be represented as functions of position and time. To better apply those parameters, a dimensionless velocity u^* is defined as the ratio of absolute velocity u to nozzle outlet velocity u_0. Based on the CFD results, u^* can be represented as a function of dimensionless x-position x^*, which is defined by the ratio of absolute position x to maximum distance along x axis x_{max} (0.2m):

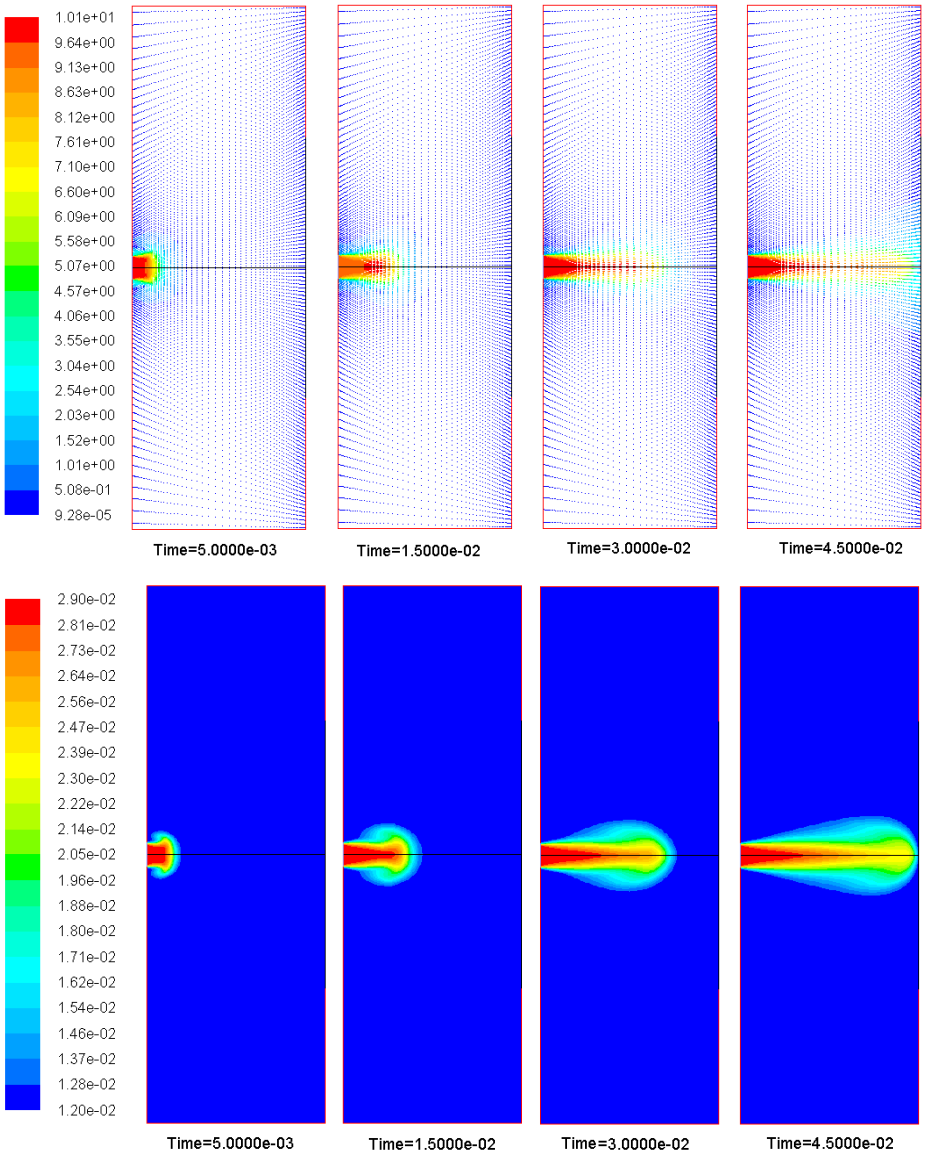

Figure 2.11 velocity vector and mass fraction of water vapor.

$$u^* = \frac{u}{u_0} = \begin{cases} \sum_{i=0}^{2} A_i x^{*i} & x^* < E_1 t^{*2} + E_2 t^* + E_3 \\ \sum_{i=0}^{1} B_i x^{*i} & E_4 t^{*2} + E_5 t + E_6 > x^* > E_1 t^{*2} + E_2 t^* + E_3 \\ \frac{u_c^*}{x_c^* - 1} x^* - \frac{u_c^*}{x_c^* - 1} & x^* > E_4 t^{*2} + E_5 t + E_6 \end{cases} \quad (2.11)$$

where the section dividing criteria and parameters such as E_i, u^*_c and x^*_c could also be determined by a function of dimensionless time, which is defined as the ratio of absolute time t to maximum time of transport t_{max} (set as 0.05 s):

$$x_c^* = E_4 t^{*2} + E_5 t + E_6 \tag{2.12}$$

$$u_c^* = \sum_{i=0}^{2} B_i \left(E_4 t^{*2} + E_5 t + E_6 \right)^i \tag{2.13}$$

$$B_i = \sum_{j=0}^{2} b_{ij} t^j \qquad i = 0,1,2 \tag{2.14}$$

All coefficients A_i ,b_{ij} and E_1-E_6 from Equation 2.12-2.15 can be determined by a curve fitting method based on CFD simulation results, as shown in Tables 2.3, 2.4 and 2.7 in the appendix.

Similarly, relative humidity can also be correlated as a function of dimensionless position x^* and dimensionless time t^*, as:

$$Y^* = \frac{Y}{0.012} = \begin{cases} \sum_{i=0}^{3} C_i x^{*i} & x^* < E_7 t^* + E_8 \\ \sum_{i=0}^{3} D_i x^{*i} & E_9 t^{*2} + E_{10} t^* + E_{11} > x^* > E_7 t^* + E_8 \\ 1 & x^* > E_9 t^{*2} + E_{10} t^* + E_{11} \end{cases} \tag{2.15}$$

where the section dividing criteria and parameters such as D_i could also be represented by a function of dimensionless time (ratio of absolute time t to maximum time of transport t_{max}, which is set as 0.05 s in this study):

$$D_i = \sum_{j=0}^{2} d_{ij} t^{*j} \qquad i = 0,1,2,3 \tag{2.16}$$

All coefficients C_i ,d_{ij} and E_7-E_{11} from Equation 2.11-2.15 can be determined by a curve fitting method based on CFD simulation results, as shown in Tables 2.3, 2.4 and 2.5.

Table 2.3 CFD Parameters of A_i

I	2	1	0
A_i	-0.3422	0.0521	1

Table 2.4 CFD Parameters of B_{ij}

B_{ij} i \ J	3	2	1	0
1	-9.0835	3.4834	3.847	-5.5016
0	11.778	-12.653	7.6908	0.6321

Table 2.5 CFD Parameters of C_i

I	3	2	1	0
C_i	0.8811	-1.6978	0.3043	2.4078

Table 2.6 CFD Parameters of D_{ij}

D_{ij} I \ j	3	2	1	0
3	-7298.8	25232	-18199	4060.8
2	32920	-23606	2822.8	1109
1	44219	-41681	11881	-711.1
0	-17007	17036	-5084.3	390.75

Table 2.7 CFD Parameters of E_i

i	1	2	3	4	5	6
E_i	-0.3194	1.3383	-0.0853	-0.6761	1.5931	0.1022
i	7	8	9	10	11	
E_i	1.0859	-0.0241	-0.5306	1.5388	0.0523	

Thus, ambient parameters of gas phase velocity and relative humidity are able to be represented by a function of dimensionless position x^* and dimensionless time t^*. These ambient parameters can be used as input ambient conditions for the parametric model.

Figure 2.12 shows the mass residual of droplet along x (up to L) for droplets of different initial sizes. The results suggest that, for coarse droplets (*e.g.*, 500 μm), the evaporation can be ignored since the total evaporation is small (*e.g.*, Δme <1%). Hence, no modifications of evaporation effect on coarse droplet measurements are needed in this study. Figure 2.12 also suggests that, for fine droplets (*e.g.*, 5 μm), the evaporation is relatively significant (>16% for Δme). However, since our size measurement of fine droplets is performed very close to the nozzle, there is also no need to take the evaporation effect into account on the fine droplet measurements. Another observation is

that, for fine droplets, the evaporation rate is faster at the beginning, which might be due to the relatively large cooling from the initial droplet temperature of human body temperature that is higher to the ambient temperature. In addition, for very fine droplets (say < 5 μm), they may evaporate quite fast near the nozzle exit region, hence the evaporation rate may affect their hydrodynamic transport and humidification performance in that region, as suggested by Chen and Zhao (2010) and Gupta *et al*. (2011). However, since this paper is mainly focused on the coarse droplet generation and size measurement, the evaporation effect of very fine droplets has little impact on our results.

2.5.4 Size Distribution of Droplets

Table 2.8 gives an example of the bin size distribution of coarse droplets. It can be seen that, after reaching the peak between 137~197 μm, the number of droplets decreases as its size increases. It also shows the diameters of peak droplets are around 70-190 μm, which are comparable to those in Duguid (1946). Since the primary objective of this paper is to present a new development methodology of cough simulator, no attempt is made in the experiments to obtain results that can be the best fit to any existing data such as reported by Duguid (1946).

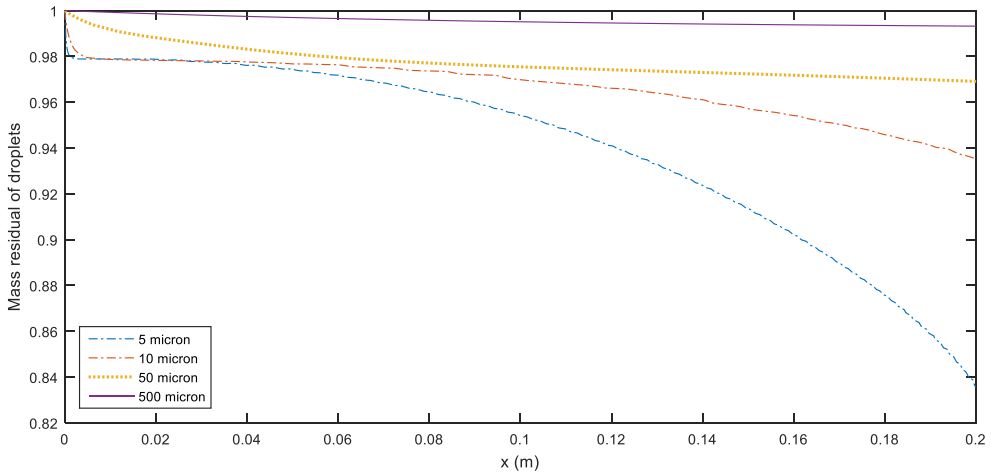

Figure 2.12 Dimensionless droplet diameter varies with time.

For different initial sizes of 100 μm and 300 μm, Figure 2.12 shows the dimensionless droplet diameter (d^*) varies with distance (up to $x=L=0.2$m). Based on predicted data here, it can be observed that all sizes of droplet evaporate extremely slowly along the trajectory. The evaporation rate is affected by the ambient condition, which is implemented by the results of CFD model. The evaporation rate is slower at the beginning, which might be due to the fact that the droplets are still in the core region of the jet flow. Hence, it could be assumed that for coarse droplets, the evaporation can be ignored since the total evaporation is small ($\Delta m_e<0.4\%$), but for fine droplets, the evaporation should be taken into the consideration as suggested by Chen and Zhao (2010) and Gupta *et al*. (2011).

2.5.5 Coarse Droplet Size Distribution

Table 2.8 gives an example of the bin size distribution of coarse droplets. It can be seen that, after reaching the peak between 137~197 μm, the number of droplets decreases as its size increases. It also shows the diameters of peak droplets are around 70-190 μm,

which are comparable to those in Duguid (1946). Since the primary objective of this paper is to present a new development methodology of cough simulator, no attempt is made in the experiments to obtain results that can be the best fit to any existing data such as reported by Duguid (1946).

Table 2.8 Bin data of coarse droplet measurement

Droplet diameter (μm)	<77	(77,137]	(137,197]	(197,257]	(257,317]	(317,377]	(377,437]	(437,497]	(497,557]	(557,617]	(617,677]	(677,737]
Total number	177	542	756	406	322	184	90	42	23	12	6	3

The residual probability of droplet size could be expressed as a number-based Rosin-Rammler distribution:

$$P(X > x) = \exp\left[-\left(\frac{x}{\alpha_C} \right)^{\beta_C} \right] \tag{2.17}$$

where the x is in unit of μm. The corresponding PDF can be yielded as:

$$f_{N,C}(x) = \frac{d}{dx}(1-P) = \frac{\beta_C}{\alpha_C}\left(\frac{x}{\alpha_C} \right)^{\beta_C - 1} \exp\left[-\left(\frac{x}{\alpha_C} \right)^{\beta_C} \right] \tag{2.18}$$

where the constants α_C and β_C can be determined by the least-square method, and the subscripts N and C represent number-based and coarse, respectively. For the data set in Table 2.8, these constants are calculated as:

$$\alpha_C \approx 224.6$$
$$\beta_C \approx 2.092$$

Figure 2.13 shows a good agreement in the accumulative distribution between the fitted Rosin-Rammler curve and experimental data.

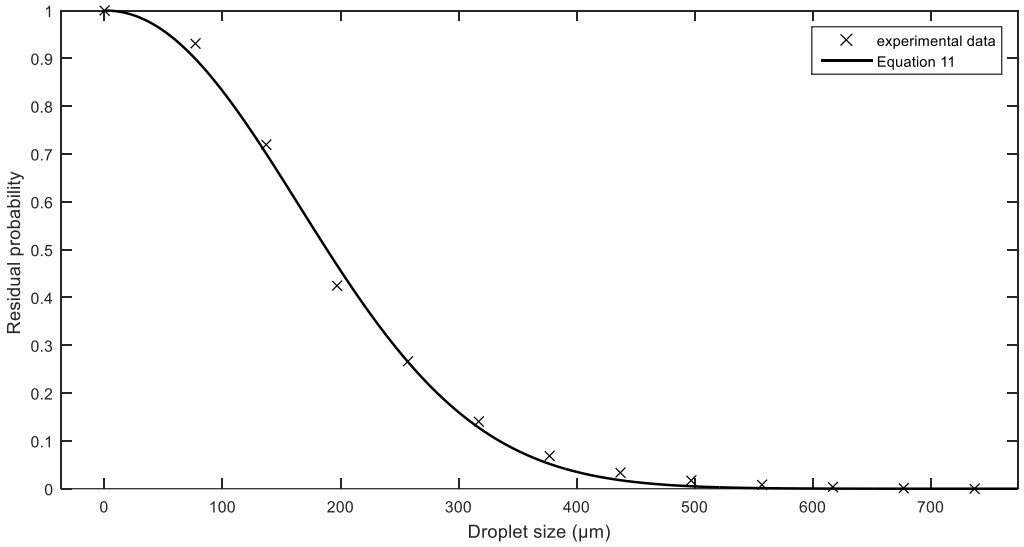

Figure 2.13 Experimental data of droplet size distribution.

Aforementioned number-based droplet size distribution can be converted into a mass-based function by:

$$f_M(x) = \frac{\pi \rho_d}{6} \frac{N_T}{m_T} x^3 f_N(x) \tag{2.19}$$

where m_T, N_T, ρ_d represent total mass, total number and droplet density. And $f_N(x)$ is expressed by equation (2.19), hence the mass-based PDF for coarse droplets can be derived as:

$$f_{M,C}(x) = \frac{\pi \rho_d N_T \beta_C}{6 m_T \alpha_C} x^3 \left(\frac{x}{\alpha_C} \right)^{\beta_C - 1} \exp\left[-\left(\frac{x}{\alpha_C} \right)^{\beta_C} \right] \tag{2.20}$$

The droplet size range of fine droplets, generated by nebulizers, varies depending upon the different temperature and solution concentration conditions (Steckel and Eskandar, 2003). In this study, the droplet size and size distribution of fine droplets are measured by laser diffraction using Sympatec® HELOS/KR.

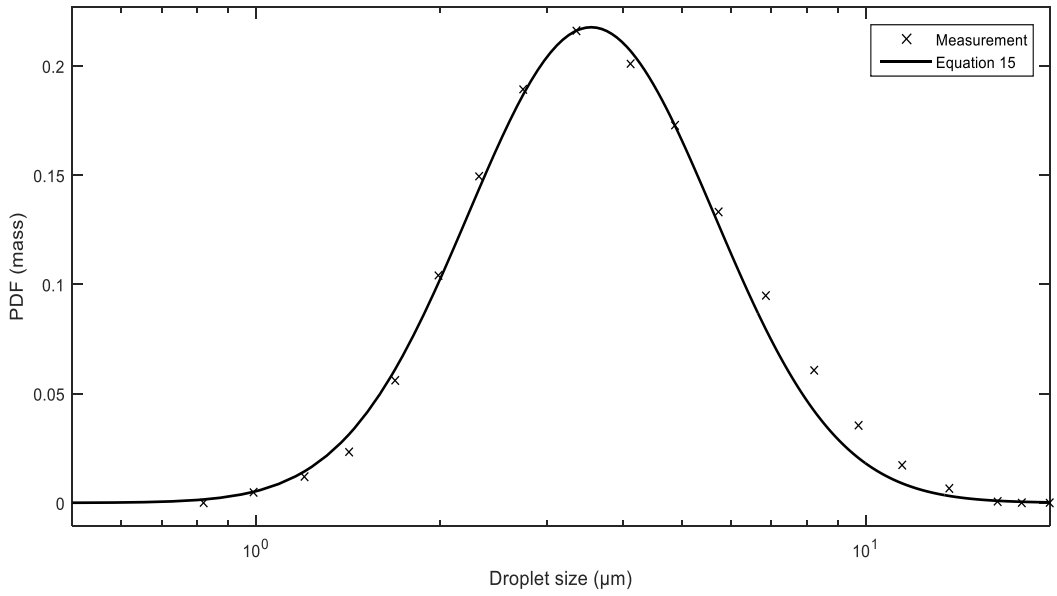

Figure 2.14 Curve fitting of fine droplet pdf.

Figure 2.14 shows a mass-based distribution with a mean of 4.69 μm and a range between 0.8-16 μm. This result matches the specification of similar nebulizers under the operation of the same conditions (Justnebulizers, 2015), which shows the droplet size of a mean diameter around 5 μm and a size range around 0.1-15 μm. The distribution in Figure 2.14 is also in a good agreement with several similar studies reported (Shen *et al.*, 2008; Kuhli *et al.*, 2009; Beck-Broichsitter *et al.*, 2014). The measurement of this fine droplet PDF has been fitted by a log-normal distribution function:

$$f_{M,F}(x) = \frac{1}{\sqrt{2\pi}\alpha_F x} \exp\left[-\frac{1}{2}\left(\frac{\ln x - \beta_F}{\alpha_F} \right)^2 \right] \tag{2.21}$$

where the constants α_F and β_F can be determined by the least-square method. For the data set in Figure 2.14, these constants are calculated as:

$$\alpha_F \approx 0.4643$$
$$\beta_F \approx 1.481$$

Since there is no overlap of mass-based PDF between coarse droplets and fine droplets, a combined mass-based PDF can be expressed by the linear relation of the two fractions (equation 2.20 and 2.21) with different weights for fine and coarse droplets:

$$f_M(x) = \frac{m_F}{m_T} f_{M,F}(x) + \frac{m_C}{m_T} f_{M,C}(x) \tag{2.22}$$

where the m_F, m_C and m_T represent mass of fine droplets, mass of coarse droplets and total mass, respectively. In this study, the mass percentages of fine and coarse droplets are: 53.8% and 46.2%. Hence a combined mass-based PDF, with a partition of total mass fraction for each individual PDF of fine and coarse droplets, can then be plotted based on equation 2.22, as shown in Figure 2.15. It shows two clear peaks of droplet mass PDF, one for fine droplets, and another for coarse droplets. This correctly represents the two major mechanisms of droplets generation from human coughing. In summary, the bi-modal cough simulator has the most complete hydrodynamics parameters and, more importantly, two main size ranges of droplets.

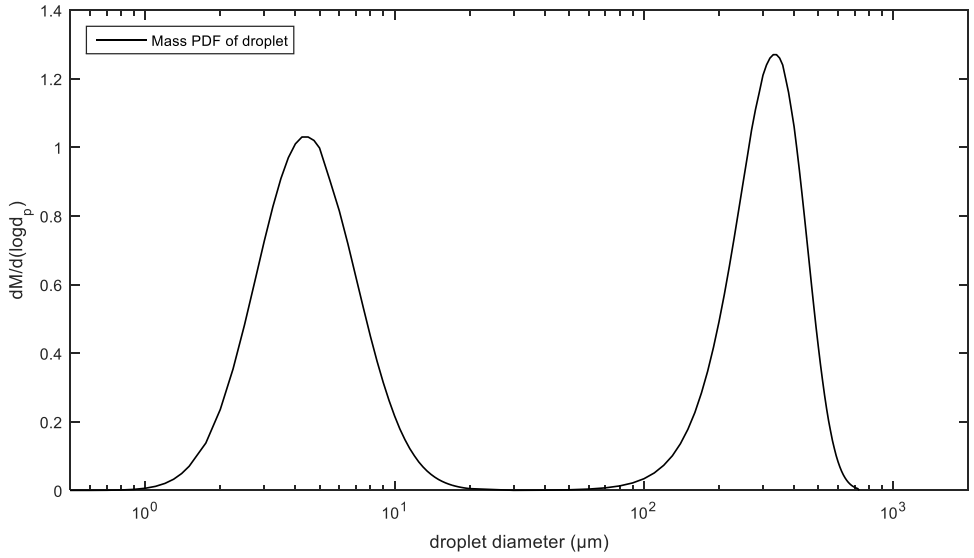

Figure 2.15 Residual probability function comparison between exp. data and Rosin-Rammlar function.

2.6 Conclusion and Relevance to Other Chapters

A bimodal cough simulator has been successfully designed and constructed, which meets all basic features desired for human coughing characteristics. The cough velocity has been measured by a dual-beam cross-correlation method. The coarse droplet size distribution has been determined by an innovative method combining the first principles of mass-balance and image analysis, while the fine droplet size distribution has been measured by a commercial laser diffraction sensor. This cough simulator can generate droplet size from sub-micron to about 800 μm. The resulted PDF is reasonably fit to a mass-based combined function consisting of a traditional Rosin-Rammler distribution for coarse droplets and a log-normal distribution for fine droplets with no overlap in between. To evaluate the evaporation effect on the spray transport, a parametric model is established with its ambient conditions predetermined from a CFD simulation. The results show that, the evaporation effect is negligibly small for large droplets with relatively short distance of trajectory. However, for the micron size droplets, the evaporation could be significant and needs to be taken into consideration.

CHAPTER 3

DESIGN AND MEASUREMENT OF THE BREATH SIMULATOR

3.1 Introduction

To determine the aerosol transport, a collection method should be employed. As mentioned previously, the coughing-induced disease transmission starts from exhaling of pathogen carrying-agents from an infected person, and ends at inhaling the aerosol by a susceptible person or depositing on floor or garments. The inhaling of aerosol determines the mount of pathogen a potential risk for a studied individual exposed in such an environment. Similar as cough, there are major characteristics of breath, such as breath duration and transient velocity.

The receiving system of the aerosol collection is very difficult to design, due to the extremely small size of droplets and tiny amount of aerosol could be collected. Most studies use optical method to determine the size, such as Particle Image Velocimetry (PIV), Laser extinction and Laser diffraction method based on Theory of Mie (Vâjâiac, 2014). However, due to the transparency of the droplet, those methods will inevitably have deflection, reflection, droplets overlapping and/or total reflection since it is an optical measurement, and the smaller the droplet size the bigger the relative error. For estimate the total amount pathogen transport by the aerosol, the total mass of droplets matters. For a 20% error in droplet diameter measurement, which is already not a low level of accuracy for many droplet optical measurement, the error of droplet mass would be $(1.2^3-1)*100\% \approx 72\%$, which is a huge error.

Hence, a new experiment measurement of droplet size and number is needed to overcome or at least provide additional validation for the optical methods. And breath simulator has been design and built. This device can simulate both inhaling and exhaling by an integrated system of combining two different flow direction one-way duct with a share opening exit, which plays the function of mouth. The flow is generated by an in-line blower, and the flow velocity and direction can be controlled and switched by a computerized valve system, which consisted of solenoid valves and a reversing valve. To measure the total mass of aerosol inhaled by the breath simulator, a fibrous collector has been mounted inside the mouth section of the breath simulator. A specific design has made for the mouth section to avoid the blowing effect of exhaling on the fibrous collector, which will has an impact of losing already captured aerosols on the filter. The solution of the saliva for the droplets composes of sodium chloride (NaCl), glycerin. The collected sample then would be dissolved into distilled water. The saliva solution has two non-evaporative components: NaCl and glycerin. The electrical conductivity of saliva solution is calibrated by a conductivity meter. With the calibrated relation of electrical conductivity and saliva concentration, the totally amount of aerosol captured is determined by dissolving the measurement sample into distilled water of 20 mL.

This chapter is for the design, calibration and actually measurement of a breath simulator to determine the aerosol transport from the cough simulator.

3.2 Feasibility Evaluation

Since this proposed aerosol measurement method has never been realized ever before, a feasibility evaluation needs to be conducted before the design of the breath simulator, to

test if this method can indeed measure the tiny amount of aerosol with reasonably good sensitivity.

First of all, the device of measuring solution electrical conductivity needs to be calibrated. The measurement device (EC400 Conductivity Meter, Extech®) has a measuring range of 0-19.99 mS/cm with a temperature range of 0-65 °C. This conductivity meter is shown in Figure 3.1.

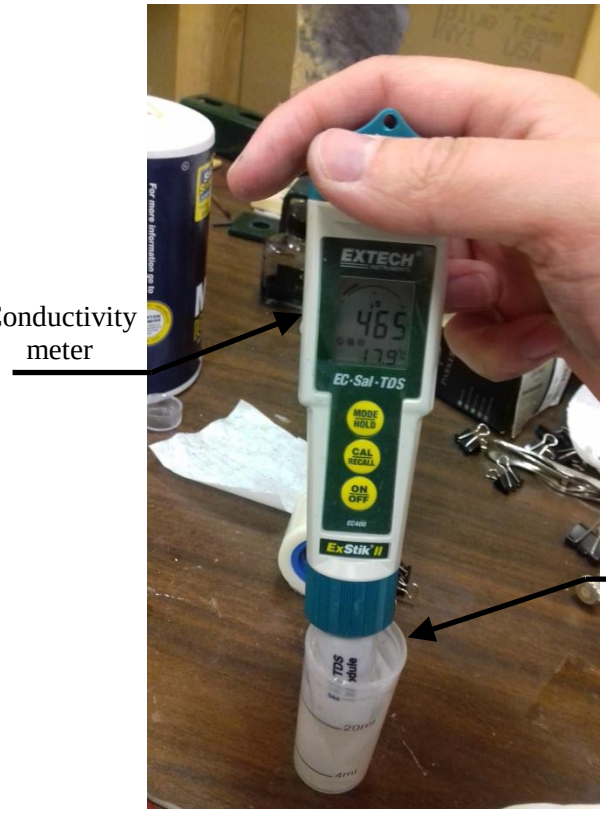

Figure 3.1 Electrical conductivity calibration of iodine salt with literature data.

For the convenience of obtain and relative good sensitivity, the iodinated sodium chloride (NaCl) and distilled water solution have been chosen to form the aqueous solution for this calibration. A set of data has been obtained based on different solution

concentration, a comparison with literature data (Weast 1989, Wolf 1966) is shown in Figure 3.2.

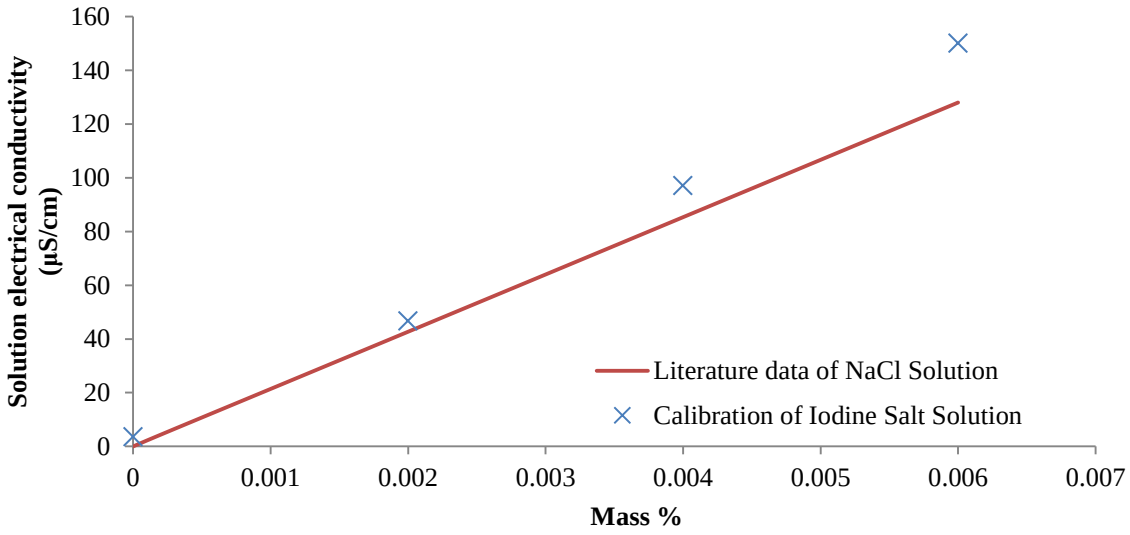

Figure 3.2 Electrical conductivity calibration of iodine salt with literature data.

The calibration result of the electrical conductivity shows good matching with reference. The difference that the experiment calibration result is a little bit higher than the literature maybe due to the fact that it has other minor components such as iodine. But overall it shows good accuracy and sensitivity for the electrical conductivity meter.

Though with the assistance of accurate device, the measurement range of this study also needs to be tested that if it's within the range of device measurement with reasonable sensitivity, as well as the filter collection efficiency. As Figure 3.2 shows, a pre-cleaned fibrous filter (4.5 × 4.5 cm^2, High-Efficiency Panel Air Filters, McMaster®) has been mounted at a distance of 30 cm from the nozzle outlet along the nozzle opening direction. The size of filter supposes to be big enough to cover all incoming aerosol. Then turn on the cough simulator for 10 times of coughing, and hence the aerosol can be

almost fully collected on the fibrous filter. After the collection, the filter was put into a test container of 20 mL distilled water to measure the solution electrical conductivity with the collected aerosol/droplets fully dissolved. The result shows the electrical conductivity to be 91.3 μs, which is within the range of calibration with good sensitivity. Hence, this method should be capable to conduct the breath simulator experiment measurement of aerosol collection efficiency, which has also been tested. Based on the mass balance between the injected aerosol, the dropping residual and the mass collected on the filter, the result show the collection efficiency is about 96%. Different filters have been used in this study too, for instance scientific lab use filter paper (Filter Paper, SEOH®) and microfiber filter (C5500 Borosilicate Glass Microfiber Filter, Thomas®). Theoretically microfiber filter has best efficiency but require a lot more pressure head than the fibrous filter.

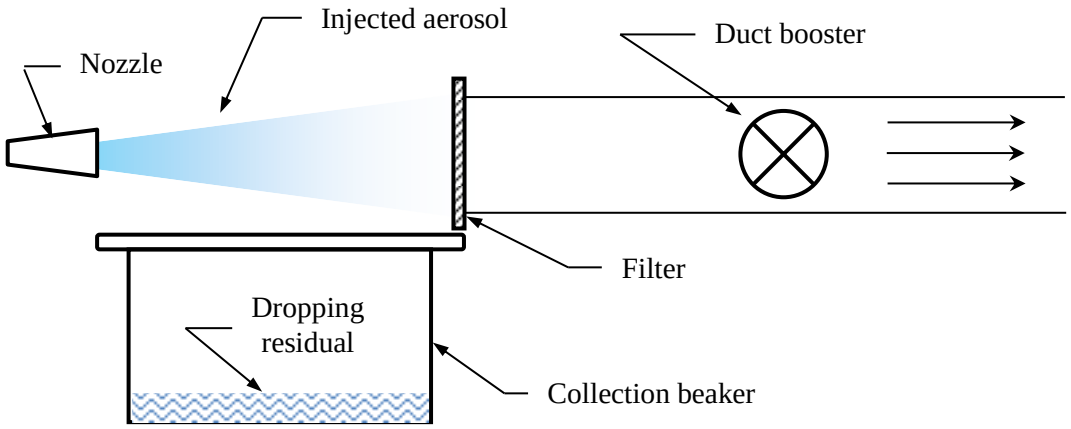

Figure 3.3 Test of measurement sensitivity and calibration of filter collection efficiency.

The saliva solution for this study has been made with the mass ratio 1000:76:12 of distilled water, glycerin and NaCl. Its property of electrical conductivity needs to be calibrated, and the range should cover the range of interest. Figure 3.4 shows the result of

calibration covering the range from 0-60% of saliva mass percentage for the relation between measured relative solution electrical conductivity (σ/σ^*) and saliva percentage (S). The σ^* is set as 1mS/cm. More measurements have been conducted in low percentage range, which might be the range of interest for this study.

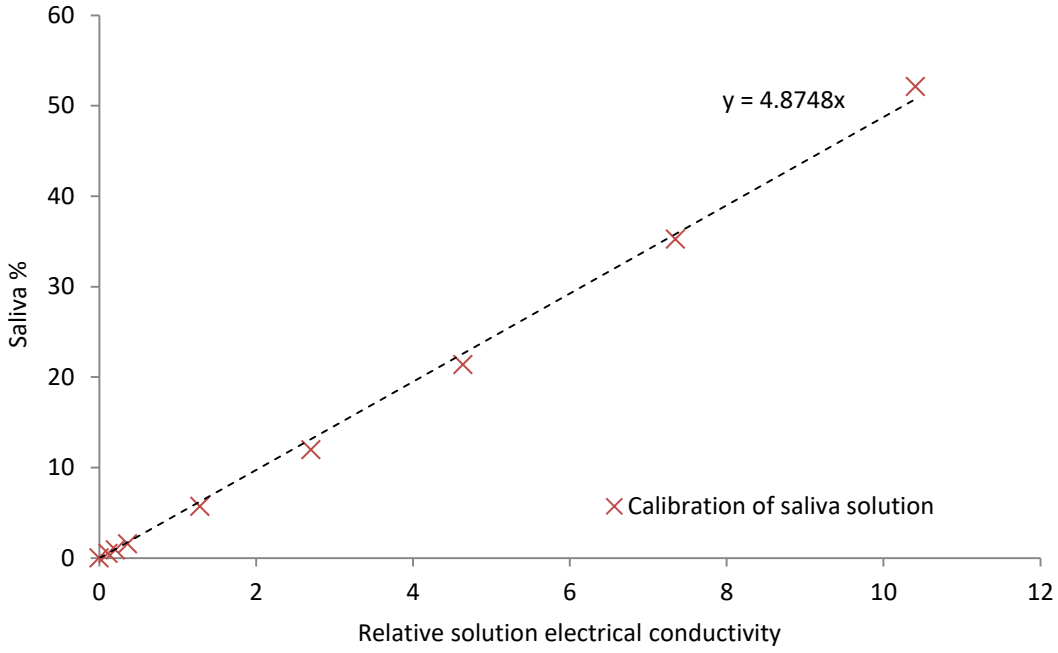

Figure 3.4 Test of measurement sensitivity and calibration of filter collection efficiency.

The result is fitted by a least square method to represent within the testing liquid, which contains the dissolved aerosol collected. This relation can be represented by a linear function, which is in similar manor for most aqueous solution (Behrends, *et al*., 2006):

$$S = 4.875\frac{\sigma}{\sigma^*} \tag{3.1}$$

Therefore, based on the method aforementioned, by measuring the electrical conductivity of the aerosol dissolved solution sample, the amount of aerosol collected by the breath simulator can be determined.

3.3 Design of Breath Simulator

3.3.1 Design Principle

For the purpose of measuring aerosol transport, the breath simulator is designed based on the following principles:

1) It can effectively collect aerosol. 2) It's geometry, principle, fluid and/or solid mechanics characteristics reasonably match the ones of human breath, such as similar opening area of human mouth, as well as the similar controllable flowrate/velocity, etc. 3) The breath similar should be able to have both inhaling and exhaling functions.

Hence, based on three principles aforementioned, three different design plans have been proposed for the breath simulator as shown in Figure 3.5.

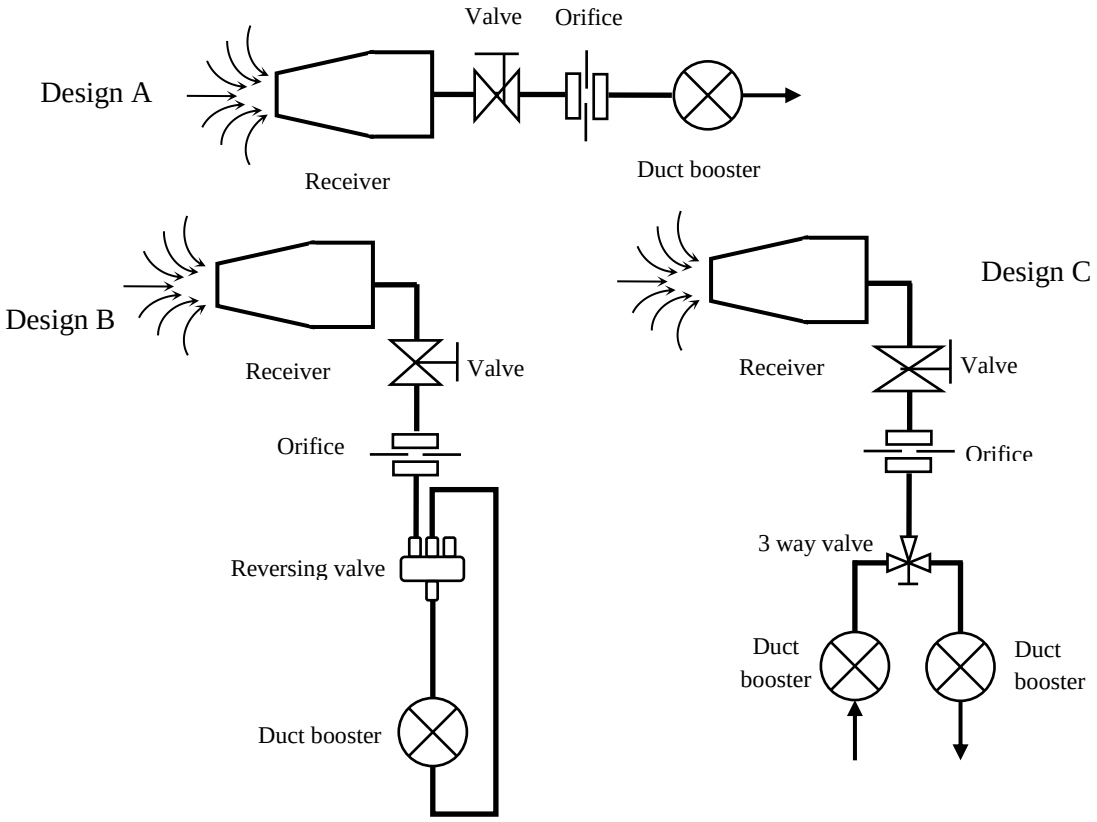

Figure 3.5 Schematic diagrams of different designs of breath simulator system.

The typical set of major components for breath simulator includes a receiver, a control valve for flowrate, an orifice and a duct booster (design A). The duct booster provides the flow work driving ambient air flowing through receiver to realize the function of inhaling. The aerosol would be captured in the receiver which has a filter inside. The flowrate can be controlled by the valve and monitored by the orifice. Design B and C extend the ability of the system further to include exhaling functions. For design B, a reversing valve is employed into the loop to make one single duck booster can deliver air flow for both directions. For the same purpose, design C uses two boosters instead of one to make the breath simulator functions of inhaling and exhaling realizable and the flow direction is controlled by a three way valve.

The inhaling pathogen carried by aerosol from human breathing has significant random nature and sensitive by the synchronizing of coughing and breathing. Hence in this study, for the simplicity and cost effectiveness, design A is chosen to build the real experiment system, as shown in Figure 3.6. For left to right, the whole system is consisted of a receiver to collect aerosol, a valve to control the flowrate, an orifice to monitor the flowrate, a duct booster to provide the driven force of the flow, besides a supporting structure serves as a base for the whole breath simulator.

3.3.2 Actual Experiment System and Design of Receiver

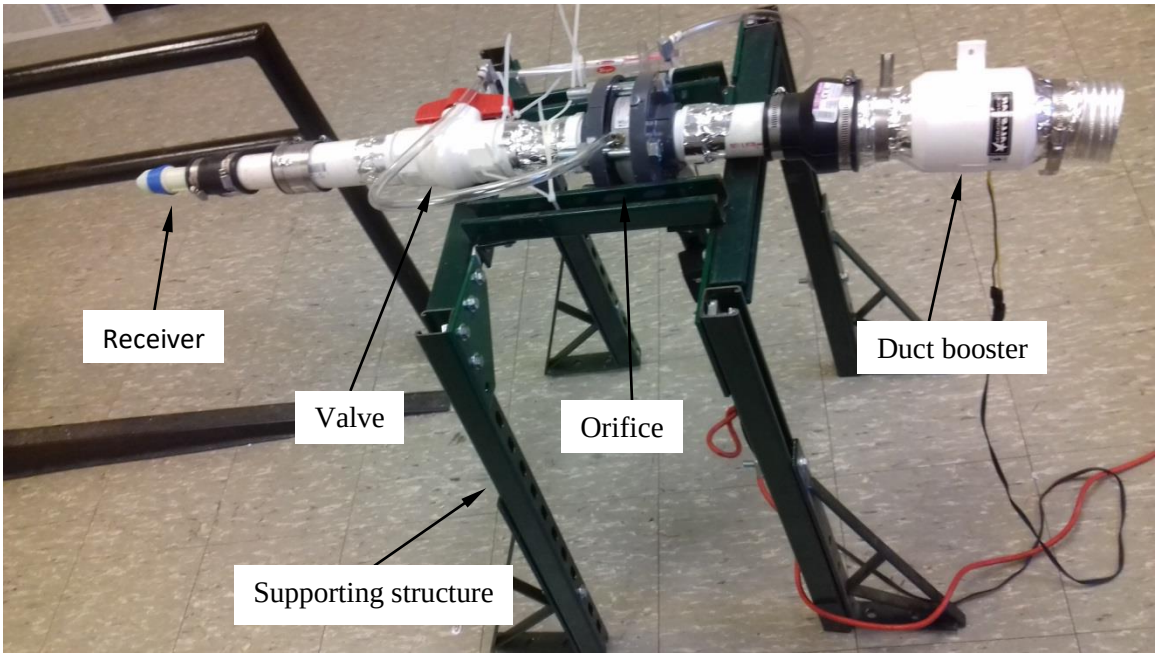

Figure 3.6 Real system of the breath simulator.

For the components and devices selection, the valve is 1-1/2 diameter PVC Solvent Socket Ball Valve (S-600, LEGEND VALVE®). The orifice plate flow meter has measuring range of 0-372.09 SCFM (PE-F-3, Dwyer®) with accuracy of ±0.7% full scale.

Duct booster is 3” in diameter and 8” in length with a capacity of 170 CFM (ALL13008, Allstar®). The supporting structure is constructed by standard steel basic structures (Unistrut®). The most critical component is the receiver, which is dedicatedly designed with the assistance of computer aided design (CAD) software Creo Parametric 2.0 and then produced by 3-D printer of material of acrylonitrile butadiene styrene (ABS). The CAD design and some major dimensions are shown in Figure 3.6.

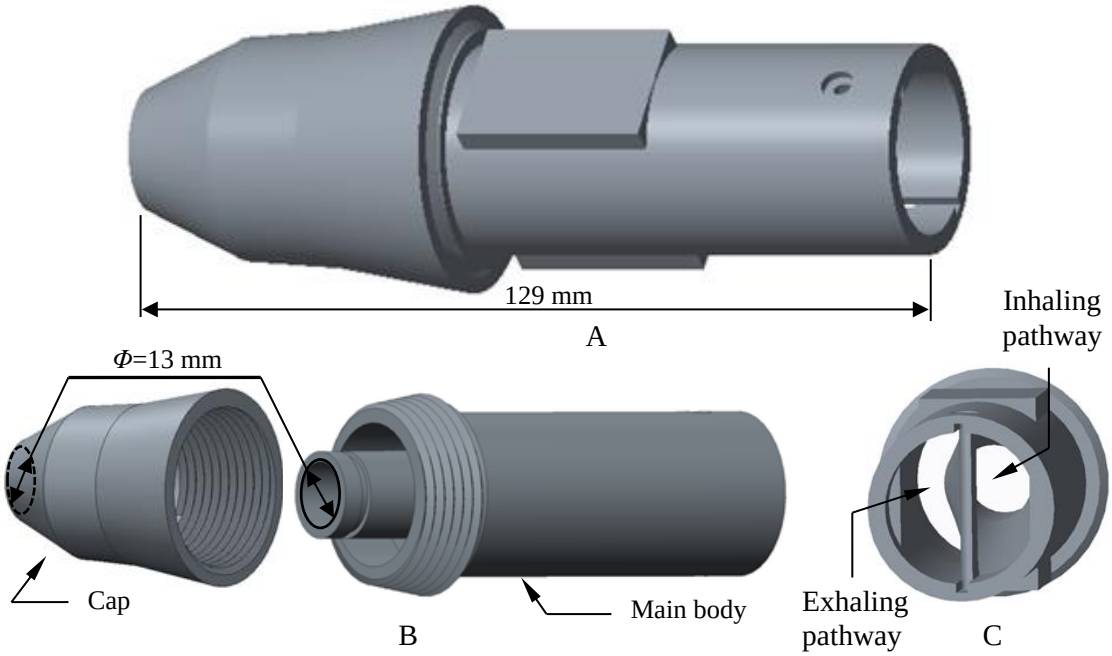

Figure 3.7 CAD design of the receiver.

The receiver is designed to realize basic functions including both inhaling and exhaling with the equivalent hydrodynamic diameter of human nostril area (Gupta *et al*., 2009a). The breath simulator is designed into two parts, one is the cap the other is the main body, which has two one-way flow path ways to simulate both inhaling and exhaling. Part A of Figure 3.7 shows the assembly of the designed receiver. Part B is the

exploded view showing the connection between cap and main body is designed as angled thread sealing. It has good sealing performance and easy to disassemble to place or retrieve filter. And part C shows the details for the two pathways of inhaling and exhaling. The whole breath simulator system can simulate transient periodic breathing of both inhaling and exhaling by switching the reversing valve (or switch to different duct booster depends on which design in Figure 3.4). The openings at both the cap and the main body are 13 mm in diameter, and the total length of the receiver is 129 mm, which is about the size of human head in horizontal direction. When doing the experiment, air flow will be coming into the receiver through the cap opening, and further going through only the opening of the main body since the inhaling pathway is open and exhale pathway is closed. For the exhaling function, the air flow will be going through the exhaling pathway only but not the inhaling pathway since the inhaling pathway is closed and exhaling pathway is open, and hence the flow bypasses the opening of the main body and eventually exits from the opening of the cap. This function is designed and shown in Figure 3.8.

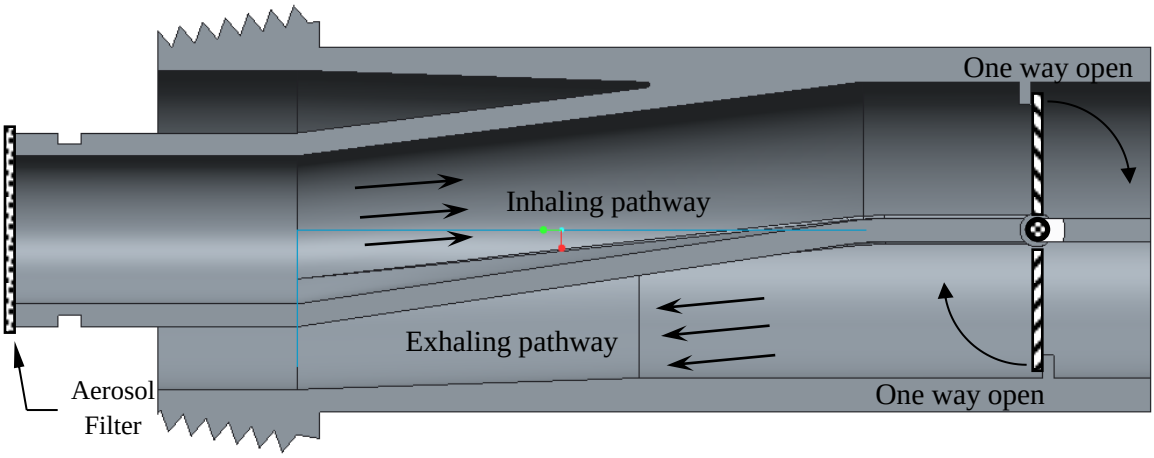

Figure 3.8 Section view of the main body of the receiver design.

The two-pathway function is controlled by two blocks at the end of the main body. When the flow is in inhale direction, the exhale block closes automatically while the inhale block turn to open position, and vice versa for the exhaling flow. The aerosol is collected during the inhaling operation. Hence, the filter is mounted at the opening of the main body. The real receiver is shown in Figure 3.9.

Figure 3.9 Receiver produced by 3-D printer.

In Figure 3.9, part A and B are the assemble system and dissemble parts. The geometry is exactly same as the CAD design. The material is hydrophobic, and material is the same although it has different color. Part C shows the filter mounted on the opening of the main body.

3.4 Experiment Measurement

3.4.1 Experiment Setup for Capturing Aerosol by Breath Simulator

To test the actually capability of capturing aerosol for the design breath simulator, an experiment measurement has been conducted. The experiment system has a cough simulator periodically and continuously generating coughing aerosol, meanwhile the breath simulator operating to capture any aerosol floating near the receiver of the breath simulator. The vertical level of both cough simulator and breath simulator are the same of 1 m, which is chosen comparing a typical sitting height of an average human. The distance between cough simulator and breath simulator is various between 0.5 m to 1.7 m. The schematic diagram of the experiment system is illustrated in Figure 3.10.

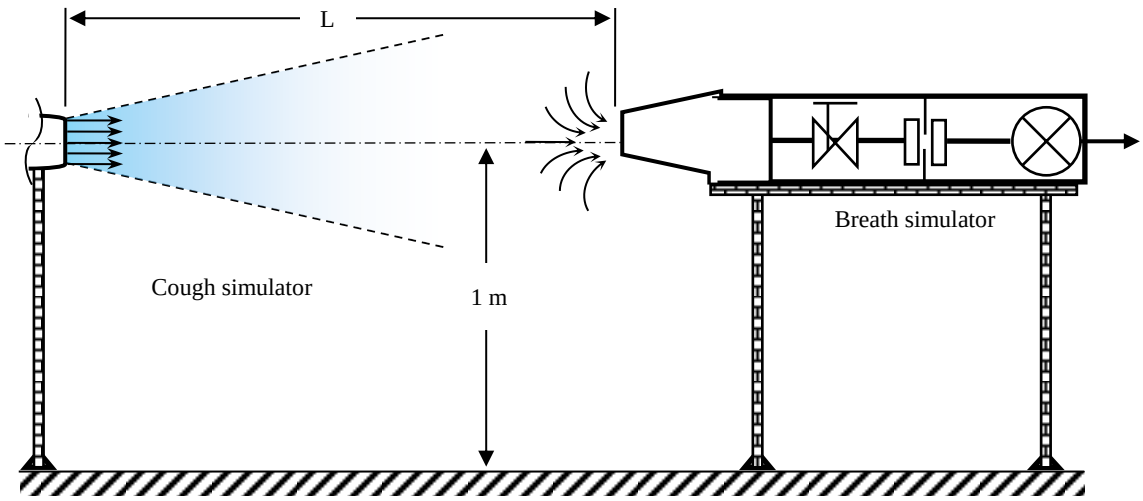

Figure 3.10 Measurement setup for cough and breath simulators.

Each set of experiment last between 100 to 300 times of coughing, the coughing duration is 1 second and the interval time between each coughing is 3 seconds. The filter

is used only for one set of experiment. After each set, the sampling filter is placed into a 20 mL volume bottle to fully dissolve any captured aerosol with lab scale 20 mL distilled water. The filter needs to be pre-cleaned by distilled water before the experiment measurement and calibrated with the conductivity meter to make sure the filer is “clean” enough. Besides, the conductivity meter needs to be cleaned by distilled water every time before each measurement.

3.4.2 Experiment Measurement Result and Analysis

The experiment measurements have been conducted under various conditions for several times, as shown in Table 3.1. Measurements including two different distance 0.5 m and 1.7 m. Number of coughs varies from 100-300 times. The volume of solvent for distilled water is 20 mL for all cases. The last column on the right is the measured electrical conductivity in unit of μS/cm after long enough time for all captured aerosol dissolves.

Table 3.1 Original Measurement Data

No.	distance (m)	coughs (N)	solvent mL	Measured E.C. μS/cm
1	1.7	100	20	16.2
2	0.5	100	20	13.1
3	0.5	200	20	32.1
4	0.5	205	20	29
5	0.5	300	20	27.7
6	0.5	300	20	27.6

The raw data from Table 3.1 needs further calibrated to eliminate the system error, which is the base electric conductivity. Because the solution electrical conductivity is a linear function of saliva mass percentage, it’s able to use the following equation to eliminate the system error:

$$\sigma = \sigma_{raw} - \sigma_{base} \tag{3.1}$$

The σ_{base} can be different value among different filters used in this study, usually it's around 5-15 μS/cm. Then by applying equation 3.1, the percentage of the aerosol captured by the breath simulator can be determined, as shown in Figure 3.11.

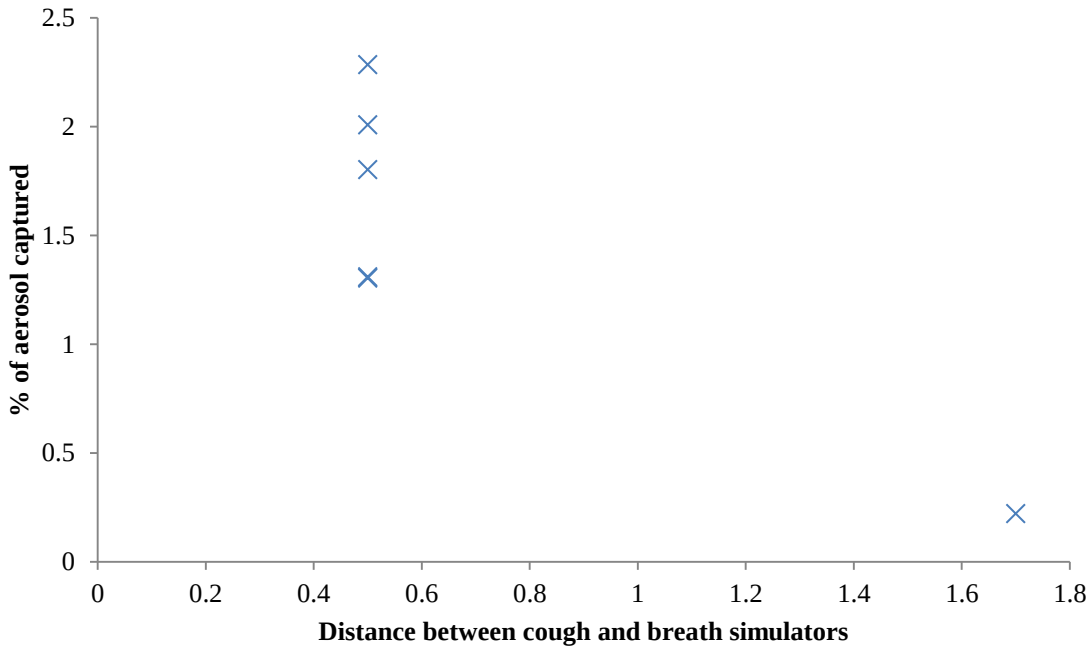

Figure 3.11 The percentage of the aerosol captured by the breath simulator.

The result shows that the aerosol transport has certain degree of randomness, which is also true for the nature of human coughing itself. Even so, it still shows at farther distance (1.7 m), the collected aerosol by the breath simulator is about one magnitude smaller than the closer distance (0.5 m). This result will be used as reference for the validation of the CFD simulation.

3.5 Conclusion and Relevance to Other Chapters

A novel method of capturing and measuring aerosol transport has been proposed and experimentally validated. A whole set of measurement procedure has been created. It proves that this method has reasonable accuracy with good sensitivity within the range of study interest.

A flowrate controllable breath simulator has been designed and built. The inlet of the receiver has similar dimension of human nostril and the breathing flowrate is designed equivalent as literature data. The receiver is delicately designed by CAD software and 3-D printed. It has the capability of functioning both inhaling and exhaling through a single outlet.

An experiment measurement of coughing aerosol transport by the designed breath simulator has been conducted. Valid data has been obtained and will be used as reference for validation of CFD simulation in the following chapter.

Same as the cough simulator, this breath simulator is a critical device for this study of the experimental approach. The coupling of breath simulator and cough simulator can be installed in many indoor scenarios to experimentally determine the coughing-induced aerosol transport. The measurement result can also be used as reference to validated numerical simulation.

CHAPTER 4

DESIGN AND BUILD OF THE AIR-CONDITIONED CHAMBER SYSTEM

4.1 Introduction

To study the aerosol transport inside an A/C chamber, such a chamber needs to be built in the first place. The dimension of this A/C chamber is carefully selected with the design of air-conditioned system. This chamber should have a typical size for coughing-induced aerosol transporting within.

The reason for the experimental study of aerosol transport in the A/C chamber is to assist numerical simulation, which has many advantages but at the same time it has flaws. The numerical simulation can always provide vivid results as long as the calculation converges. However, due to the current development of computational fluid dynamics theory, physical model selection remains unclear for example for weak turbulence and weak buoyance. In the particular study, the coughing from human mouth and the chamber inlet flow from the A/C system may well fit in the range of weak turbulence, while the temperature difference between the human body and the air around may result in but a weak buoyance. Via the experiment measurement of aerosol transport inside an A/C chamber, a lot of information can be provided to the CFD model for numerical simulation purpose for model selection as well as boundary condition.

A chamber with dimension of 7x8x10 fts has been designed and built to measure the aerosol transport. Four chairs have been placed with equal distance among each other inside the chamber. The air-conditioned system has been implemented into the chamber. It has three inlets and three outlets. The air circulation rate can be as high as 40 ACH, and

the temperature can be controlled to 13 °C the lowest. So far, four chairs have been deployed in the chamber, which will be used to simulate as many as four people sitting inside. The cough and breath simulation will be taken into the chamber system and measurement will be conducted. With the experiment system (A/C chamber), flow pattern can be determined inside such as by measuring temperature and oxygen concentration.

This Chapter is to provide the environment of the experiment system. Hence coupling with cough and breath simulators the aerosol transport within can be measured.

4.2 Design and Build of the Air-Conditioned Chamber System

4.2.1 General Design Consideration and Major Parameters

As aforementioned, the size of the chamber is carefully selected according to the research focus, lab space availability and cooling capacity. The research focus for application includes small standard room, small school bus and hospital ward. Hence, the chamber, designed using Pro/Engineer®, is built with room dimension (inside) of 10x8x7 ft^3. The chamber base of support is made of steel structure; whereas the rest of parts such as floor, wall and ceiling structure are made of lumber and poly-wood broad. The ProE® design with dimensions is shown in Figure 4.1. And the actual picture is shown in the following Figure 4.2. Though it could be observed from outside, four chairs have been placed inside the chamber.

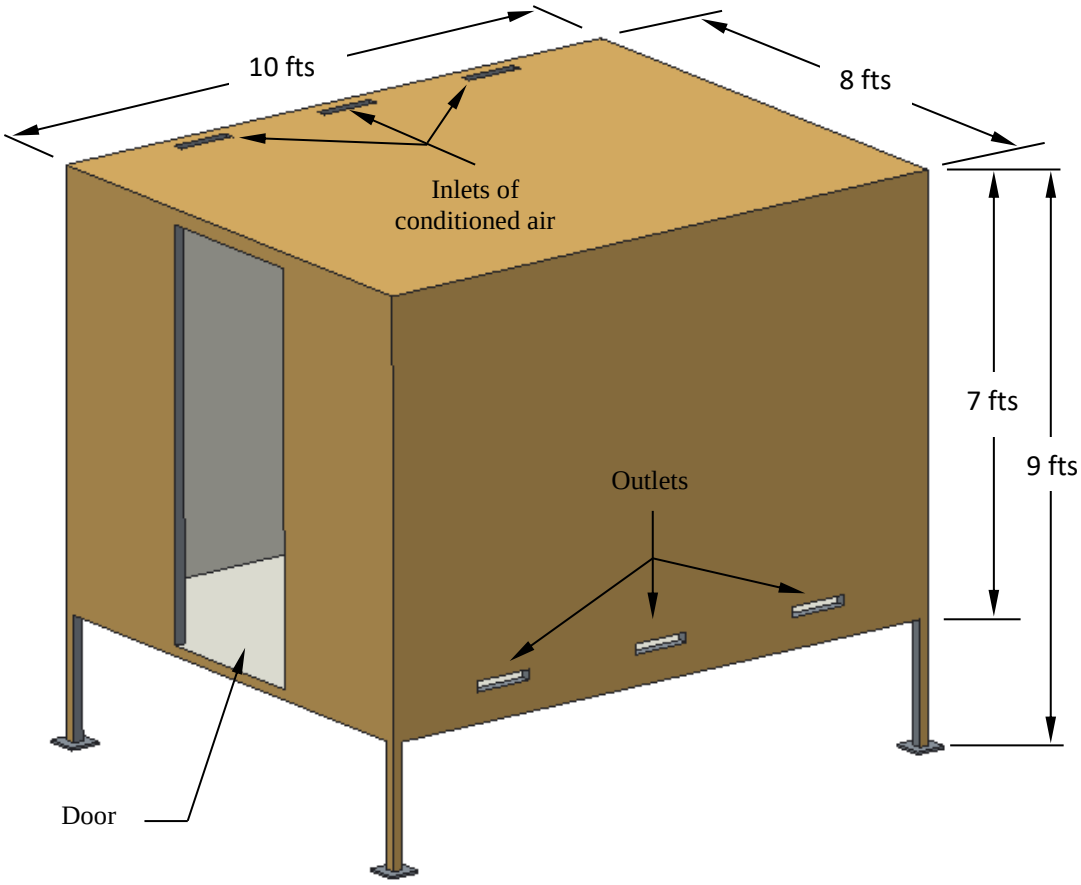

Figure 4.1 Design and key dimensions of A/C chamber.

Figure 4.2 Actually experiment system of A/C chamber.

4.2.2 Flow Pattern Design and Air Supply System

Except the size of the chamber, air circulation rate and air flow pattern also need to be dealt carefully and reasonably based on the reference data. Neither too small nor too huge of air circulation rate would meaningfully represent the indoor environment in real cases. There are several parameters need to be considered for the design: (1) air circulation rate per hour (*ACH*), (2) inlet velocity (U_{in}), (3) size of inlet (*A*), (4) inlet air flow angle (θ), (5) inlet temperature (T_{in}). Among these parameters, *ACH*, U_{in} and *A* are not independent with each other. If the temperature difference between the inlet and chamber is significant, then T_{in} could also be a factor affecting ACH. From some literatures data, the target range of design for these parameters of the chamber has been selected, as listed in Table 4.1.

Table 4.1 Chamber Design with Dimension

Variables	Value from Reference
ACH	5.6 in similar sized chamber; 12~20 in hospital; 25~40 airplane cabin
U_{in}	2.88m/s for cabin
Inlet size (Area = a x b)	Depends on ACH and U
θ	N/A, probably 0°
T_{room}, T_{inlet}	22±1°C in room, air supplied at 16°C

Besides, the air circulation pattern also needs to be determined, because the effect of conditioned air movement on the aerosol transport needs to be studied. The air circulation pattern should be able to go through the majority space of the chamber. Hence two design plans have been proposed, as shown in Figure 4.3, which is the front view of the chamber. Design A has an inlet on the top left, meanwhile an outlet on the bottom right. Hence, the air could circulate across majority space of the chamber. Another more complicated design B shows a second inlet on the top right and a second outlet near the bottom left. This makes the circulation of air can be more thorough and complex with more mixing and diffusion for heat and mass transfer inside the chamber. In this study, design A is chosen to start with, while design B remains its potential in further development for the experiment approach.

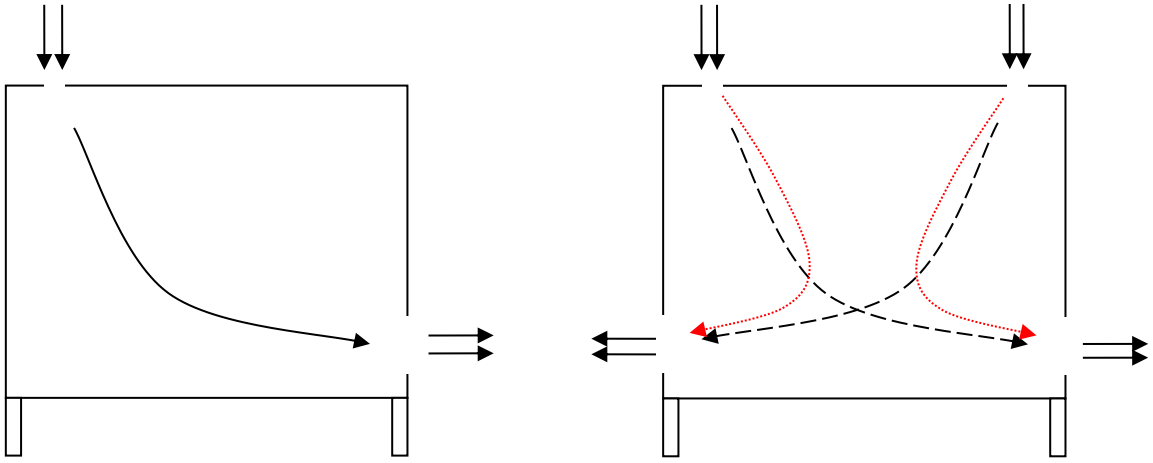

Figure 4.3 Design of flow pattern of A/C chamber.

The actual design of inlet and outlet number is three for both with equal distance between neighboring inlet/outlet. To make the direction of airflow controllable, an equal shape and size distributor is mounted at each and every inlets and outlets. The size for the distributor is 2x12 in^2. Distance between neighboring distributors is 20 inches. Distance from outlet to the floor is 4 inches in vertical direction, same for the distance from inlets to the side wall in horizontal direction. The angle of inlet air can be regulated between 0 to 90°. The actual picture can be seen in Figure 4.4.

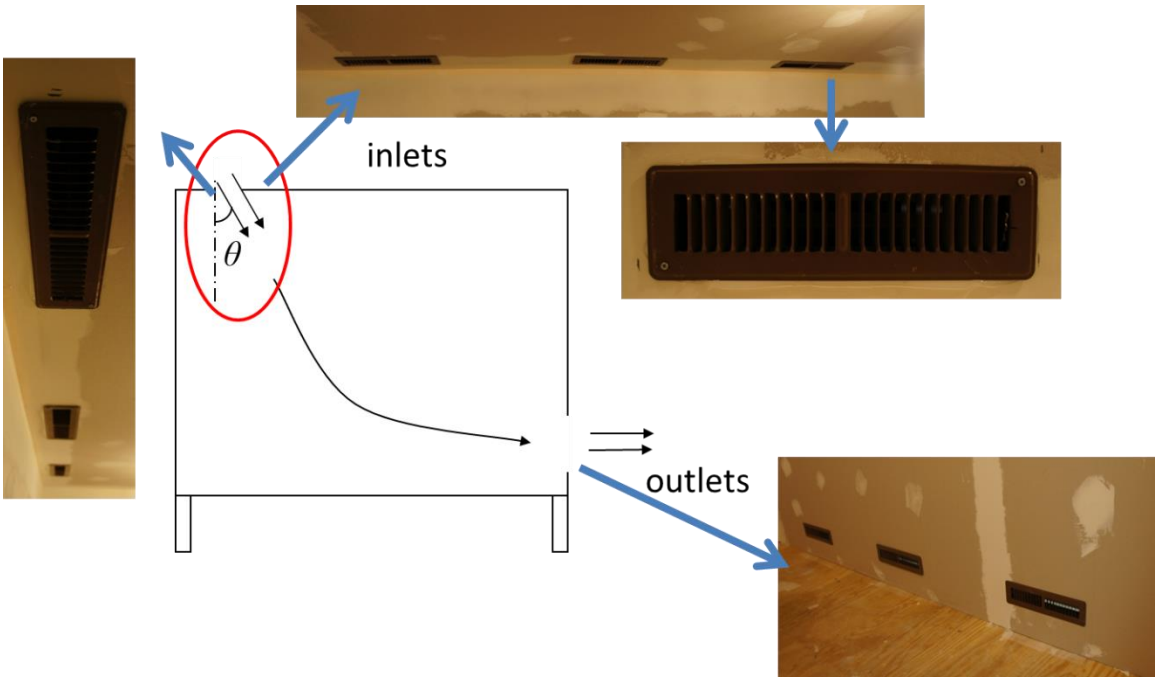

Figure 4.4 Design of inlets and outlets.

To ensure the desired cooling capacity as well as the air circulation rate, an A/C unit and a blower are installed into the system as cooling and air flow supplier, the schematic diagram of top view is illustrated in Figure 4.5. The power of A/C unit is 10,000 BTU/hr with a lowest temperature working capacity of 60 °F (900 W, LG), and the blower has a maximum capacity of 390 CFM with two different working shifts (1.32 kW, Toro Super Blower Vac).

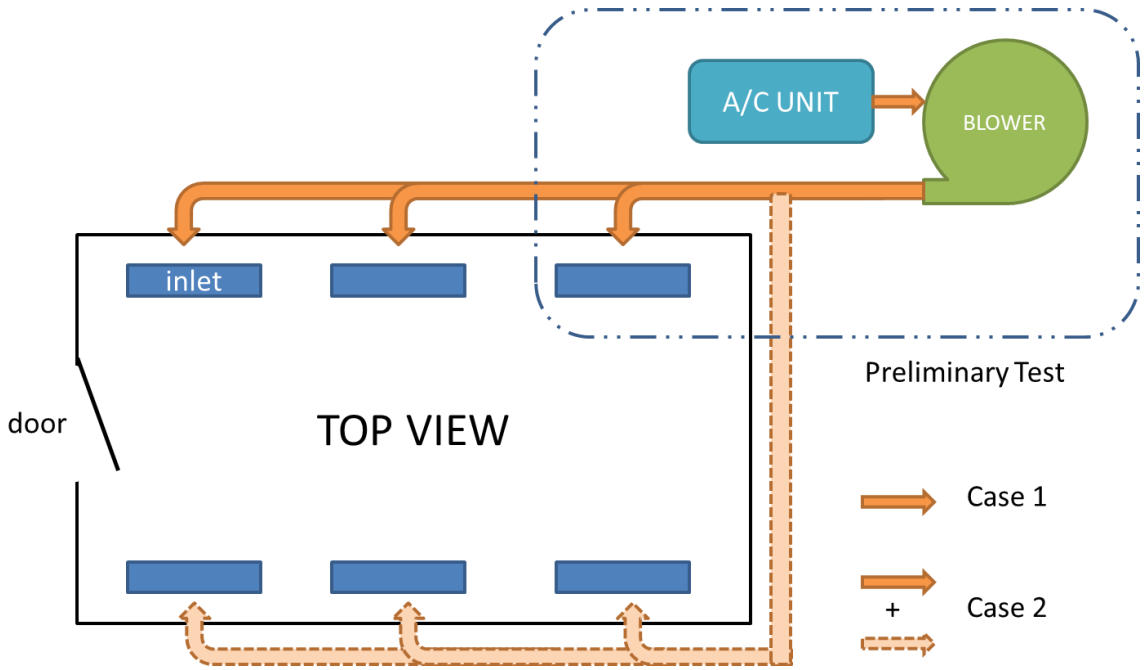

Figure 4.5 Design of air supply system.

The air coming out of the A/C unit is boosted by the blower to the piping system of the chamber air circulation. For design A the conditioned air is supplied to three inlets with flowrate control of each branch, which regulates all three inlets to either have equal flowrate or individually controllably different. For the piping system, the main stream pipe connecting to the blower is 4” in diameter, and all three branches have a diameter of 2”. The adapter between branch pipe and diffuser is 2” to 4” with shape change from circular to rectangular, which fits the shape of the inlets. The actual picture of the A/C unit, blower and the piping system is presented in Figure 4.6.

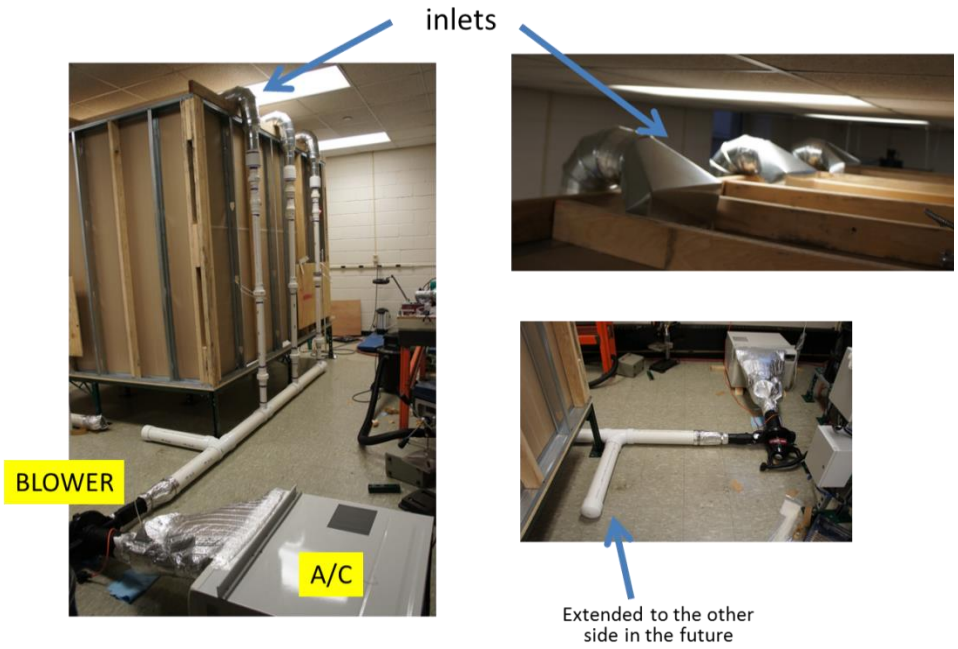

Figure 4.6 Actual picture of the experiment chamber for air supply system.

4.3 Measurement of Chamber Capacity and Key Parameters

4.3.1 Experiment Setup for Measurement of Temperature and Air Exchange Rate

The temperature is measured by type T/K thermocouple (KMQSS-020G-12, Omega®) with data acquisition system connected to computer. The thermocouple has OD of 0.02" and the response time is about 0.03 s, which is fast enough for this study. The data acquisition broad is 8/16-Channel Thermocouple/Voltage Input USB Data Acquisition Module (OM-DAQ-USB-2401, Omega®), has 8 differential or 16 single-ended analog inputs, and 24 bit resolution with up to 1000 samples/sec, it's user programmable for type J, K, T, E, R, S, B, N thermocouple or voltage input. For air exchange rate, it has been measured by inline orifice plates at each and every branch of the pipe system. The PVC orifice plate flowmeter has 2" for line size, 1.450" bore, with air capacity of 372.09

SCFM at 14.7 PSIA (PE-F-3, Dwyer®). The detailed installation and actual picture can be referred in Figure 4.7.

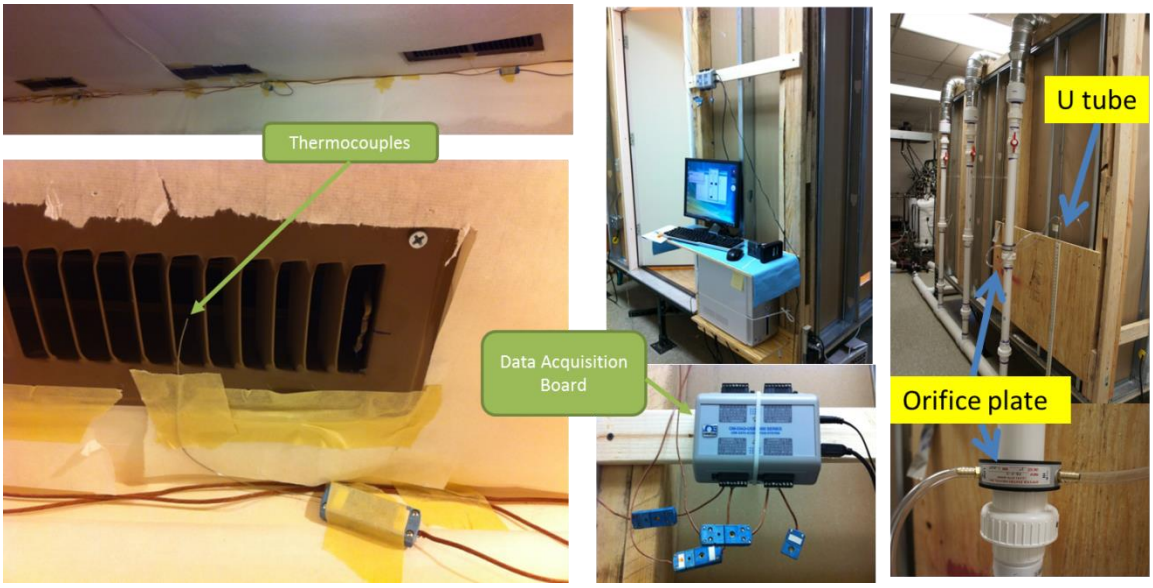

Figure 4.7 Actual picture of the experiment chamber of measurement details.

Hence, the temperature and the air flow rate/air circulation per hour have been calibrated with the aforementioned devices after turning on the A/C unit and blower for certain amount of time to make the whole system operating steadily. Then taking the reading from the U-tube connected orifice for the flowrate and recording the temperature data by the computer. The experiment measurement was running under different conditions for different switches of the blower, while the A/C unit was running at its maximum cooling capacity. For the experiment results, the supplied flow rate can be up to 40 ACH, with corresponding temperature controllable from 59 to 76 °F. The minimum ACH is 26, which is still high enough with a reasonable low temperature (76 °F/22 °C). The maximum controllable range may also be depended on the ambient temperature of

the lab environment. The inlet flow angle can be regulated between 0 and 90°. The details are listed in Table 4.2.

Table 4.2 Targeted Design Parameters for Air-Conditioned Chamber

Capacity	Min	Max
Air Exchange Rate	246.5 SCFM 26.4 ACH	346.5 SCFM 39.6 ACH
Temperature	59 °F 13 °C	76 °F 22 °C
Inlet flow angle	0°	90°

The blower has two switches, low and high capacity. The temperature and flow rate at each inlet have been calibrated for both switches of blower. As illustrated in Table 4.3, the temperature and air flow rate is relatively even among three branches (inlets), the temperatures go low because more heat is generated for high capacity operation of the blower. This shows a trade-off between cooling capacity and flow rate capacity. Branches 1 and 2 are for the study of ventilation near corners, whereas Branch 2 represents a middle inlet with minimum effects of corner walls.

Table 4.3 Measured Data in Individual Branch under Different Blower Switches

Blower switch	Parameter	Branch 1	Branch 2	Branch 3	TOTAL Q
Low	Q (SCFM)	83.4	83.4	79.7	246.5
	ACH	-	-	-	26.4
	T (˚C)	13.0	12.2	13.0	-
High	Q (SCFM)	116.5	115.2	112.8	344.5
	ACH	-	-	-	36.9
	T (˚C)	15.3	14.4	14.9	-

4.3.2 Air Tracing Measurement Using Oxygen Sensing Device

Except the temperature, oxygen concentration can be another useful indicator for tracing the air flow inside the chamber, hence provide valid information to verify the CFD simulation. A oxygen cylinder has been used as a source to provide additional oxygen. To match the original inlet temperature at chamber inlets, separate cooling of oxygen (from oxygen cylinder) is necessary, which is achieved via a cooper-based heat exchanger coil submerged in a batch of icing water. The oxygen is provided only in the middle pipeline and so being released via the middle inlet (inlet 2). The schematic diagram is shown in Figure 4.8.

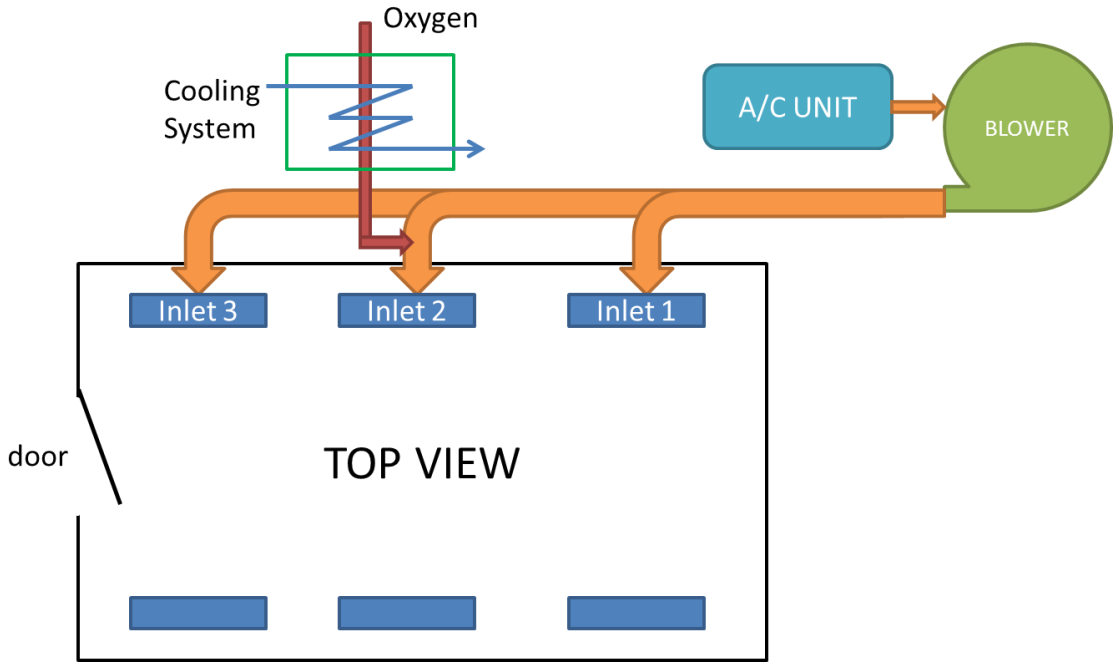

Figure 4.8 Design of oxygen measurement for the A/C chamber.

The oxygen cylinder is regulated at supplying pressure of psig(). And the oxygen concentration at each inlet is measured by the High Resolution Oxygen Analyzer (O2L,

Oxigraf, Inc.). For additional cooling capacity of oxygen gas, Ice water is used for cooling substance in the heat exchanger. The flowrate of each branch of the pipe system is measured by the plate orifice. The actually experiment setup picture is illustrated in Figure 4.9.

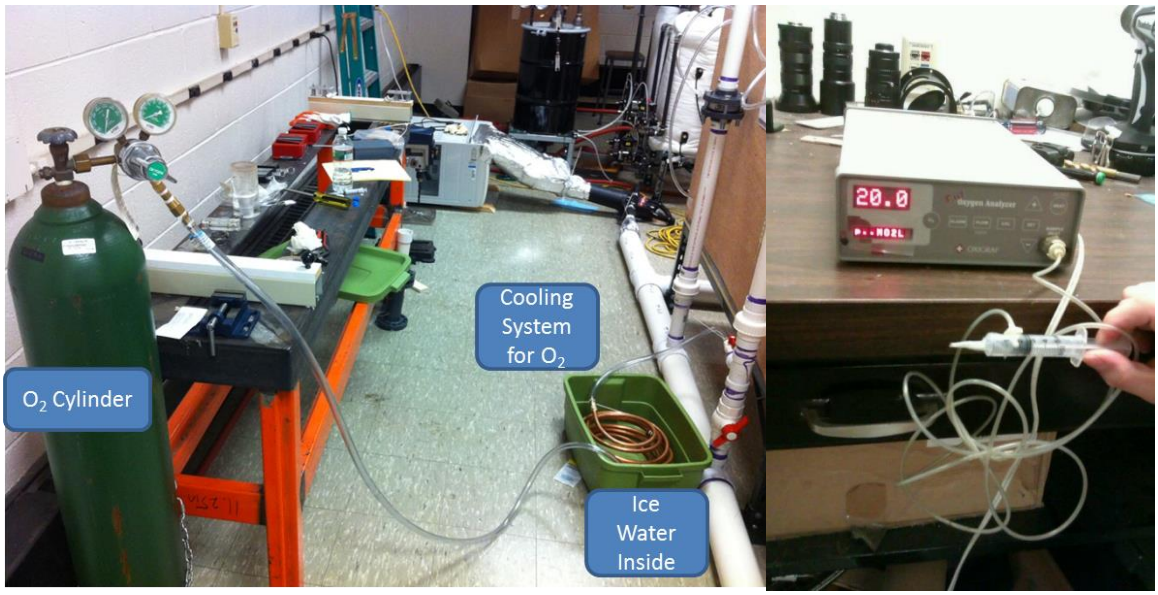

Figure 4.9 Actual picture of the oxygen measurement.

The measurement results show that the oxygen concentration in the middle inlet (inlet2) could be in a range of 42.7~52.3% based on the current experiment configuration. The oxygen concentration can be further increase if necessary by employing more or higher capacity oxygen cylinders. Meanwhile the total air exchange rate is under 38.9 ACH rather than 36.9 ACH. The increased amount of ACH should be the oxygen flow from the oxygen cylinder. The details of the experiment measurement for oxygen concentration at each inlet are shown in in Table 4.4. It shows that comparing to the other two inlets (1 and 3), oxygen concentration at inlet 2 could be more than double (52.3%).

It proves that by measuring oxygen concentration in the chamber, the air flow can be traced and hence using the experiment data to validate CFD modeling.

Table 4.4 Oxygen Measuring in Three Branches

	Branch 1	Branch 2 (O_2)	Branch 3	TOTAL
Q (SCFM)	134.9	95.5	132.4	362.8 (38.9 ACH)
T (˚C)	14.3	14.1	14.2	
O_2 %	23.6	42.7~52.3	23.1	

4.4 Measurement of Aerosol Transport by Coughing in the Air-conditioned Chamber

4.4.1 Measurement of Coarse Droplets

To test how the coarse droplets transport varies under different ACH, an experiment setup has been installed and conducted. The cough simulator is placed at one chair inside the chamber for continuous operation (coughing), while turn on the A/C system. By changing different ACH, different experiment measurement has been conducted and the results have been compared. In this study, the cough simulator is placed on the chair near the door on the left. The air circulation rate has been switched between 26-37 ACH. The cough simulator operation duration is 75 times for each set of measurement. Every cough lasts for one second, three-second is the time interval between each cough. The height of the cough simulator nozzle is about 1 m from the chamber floor. The actually picture of the experiment is illustrated in Figure 4.10. To show the fate of every coarse droplet, all surfaces inside the chamber have been covered by fibrous paper with excellence

absorption ability (very hydrophilic). And the solution of the coarse droplets is made of tap water and fountain pen ink.

Figure 4.10 Actual picture of the experiment on coarse droplet transport under different ACH.

The coarse droplets burst into the chamber space and land on the floor in front of the cough simulator under different ACH. Due to the nature of coarse generation, which is highly case by case if not completely random, the trajectory of each droplet should not be expected the same. However, as the number of the amount of droplets increases, certain pattern should emerge. For this study, the results show that no significant difference of pattern for coarse droplets transport. A sample of the measurement is illustrated in Figure 4.11. This result may due to the fact that for coarse droplet, its inertia is too big for the ambient air to influence. The momentum transfer is not big enough from the ambient air to coarse droplets. Hence, no significant difference is found between various ACH.

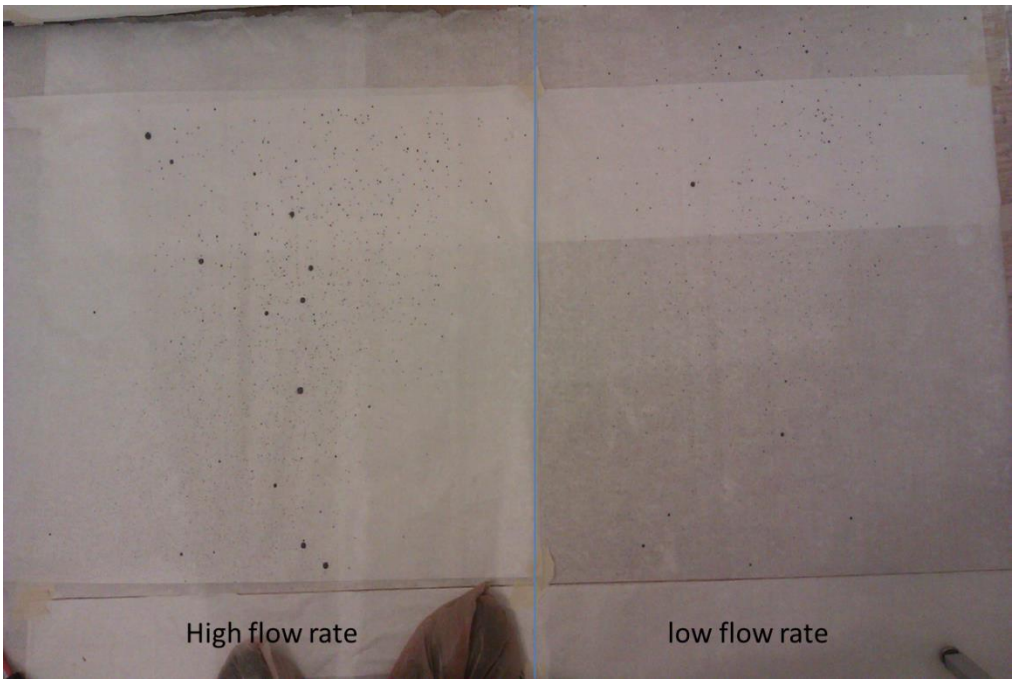

Figure 4.11 Result the experiment on coarse droplet transport under different ACH.

4.4.2 Measurement of Aerosol/Fine Droplets

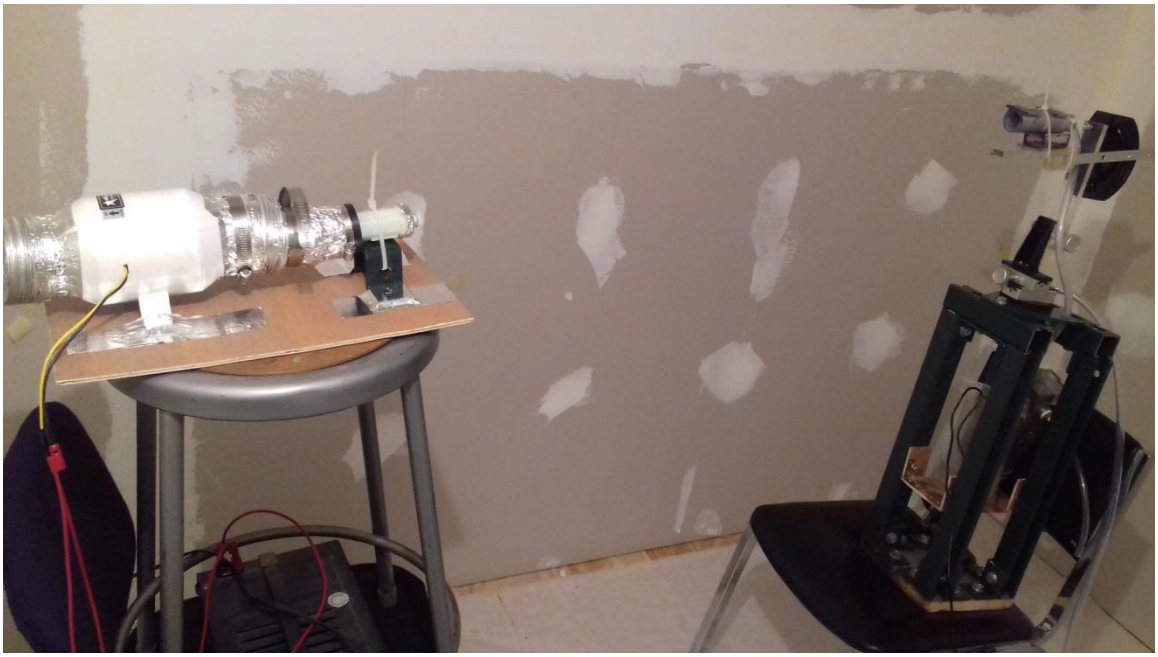

Figure 4.12 Result the experiment on fine droplet transport under different ACH.

Table 4.5 Measurement of Aerosol Transport in the A/C Chamber

No.	ACH	coughs (N)	solvent (mL)	% aerosol
1	26.4	100	20	0.37
2	39.6	150	20	0.21

As shown in Figure 4.12 aerosol transport under A/C condition. Two different air circulation rates have been applied in the chamber. The distance between the cough and inhaling simulators is 1.2 m. The results in Table 4.5 show that higher ACH tends to reduce the aerosol transport from a coughing person to others.

4.5 Summery and Next Step Plan

To provide validation for the CFD simulation, an experiment system of air-conditioned 7*8*10 ft^3 chamber has been built. The air circulation rate and cooling capacity have been calibrated. Temperature and oxygen concentration measurement have been conducted and proved good sensitivity. Coughing induced aerosol transport experiment measurement has been conducted. This experiment system can provide vital information for the CFD simulation validation.

CHAPTER 5

DYNAMIC PROCESS MODELING ON COOLING-CONTROLLED DEPRESSURIZATION IN A CLOSED CHAMBER

5.1 Introduction

Creating a sub-atmospheric pressure environment in a chamber is essential to some industrial processes such as negative pneumatic conveying and vacuum heat treatment. The depressurization can be realized via various pumping techniques (O'Hanlon, 1989; Chambers, 2005). Generally speaking, for normal mechanical pump, the efficiency of vacuum pumping decreases significantly with the depressurization. One alternative approach for chamber depressurization is by condensation. It has long been realized that condensation in a chamber prefilled with condensable vapor leads to chamber depressurization, and the condensation rate can be cooling controlled. Comparing to vacuum pumping, the condensation approach can remove many intermediate processes in energy conversions as conceptually illustrated in Figure 5.1. Consequently, the depressurization by condensation presents a great potential in having a much higher efficiency than traditional vacuum pumping whose overall efficiency conceptually is the product of efficiencies of many individual mid-processes:

$$\eta_{condensation} >> \prod \eta_{traditional} = \eta_{boiler} \cdot \eta_{turbine} \cdot \eta_{generator} \cdot \eta_{transformer} \cdot \eta_{pump}$$

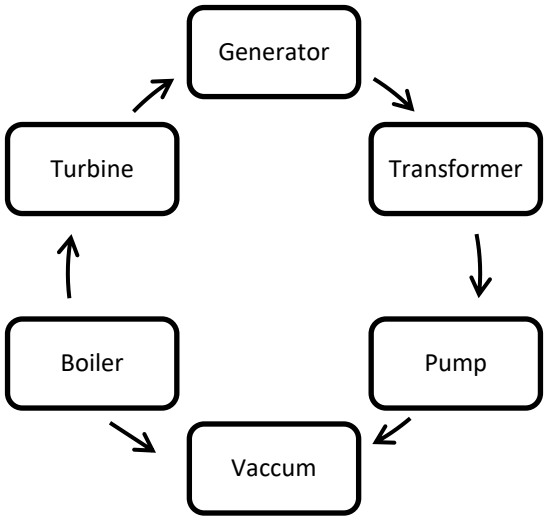

Figure 5.1 Energy-conversion processes of vacuuming by pumping or by condensation.

In addition, this method of depressurization has unique advantages of simple structure without any moving parts, as well as being noiseless and easier for system volume scale-up. The energy saving is expected to be more significant as system size increases. For instance, to vacuum a 30-gallon chamber in a minute (as achieved in this study by condensation), it would require a vacuum pumping capacity of 4 CFM that may be easily available. However, a ten-fold scale-up in size (1000 times in volume) would require a vacuuming capacity of 4000 CFM, which may be manageable by optimized condensation but would be a tremendous challenge and power consumption to vacuum pumping. Although the condensation-induced depressurization needs some small mechanical accessories such as a coolant pump, the energy penalty from those accessories is expected to be small compared to the overall saving.

Despite the apparently simple concept of depressurization by condensation, understanding of this process for the design and control of such a system is far from

completed. While the final state of a cooling-controlled depressurization process can be reasonably estimated based on the thermodynamic equilibrium, the dynamic process of depressurization is not only transient but also in thermal non-equilibrium, which is mainly governed by the rate of condensation. The development of a success dynamic process modeling requires a deeper understanding with appropriate modeling formulation on many complicated coupling mechanisms such as heat and mass transfer in cooling-controlled condensation, the transient nature of non-equilibrium during the process, the complication by the co-existence of non-condensable gas (NCG) within vapor, as well as the complex geometry and material properties of chamber and cooling device involved. So far, few modeling efforts on this topic have been reported, with none covering all mechanisms mentioned above. For instance, some dynamic process models have been developed for the dynamic characteristics in depressurization by gas discharging out of a pressurized vessel without phase change (Zhou *et al.*, 1997); Some surface condensation models deal with the coupled mass and heat transfer, yet without the inclusion of NCG (Liu *et al.*, 2004) nor under the condition of depressurization (Li *et al.*, 2011; Li, 2013). Recently some modeling efforts include heat and mass transfer coupled phase change to study only pressure drop in micro-channels (Heo *et al.*, 2013). Few modeling approaches, especially via transient and full-field CFD simulations, on depressurization by condensation of vapors with NCG have been reported.

This study is aimed to provide detailed mechanistic understanding and insights essential to the optimal design and operation of the depressurization by cooling-controlled condensation. A depressurization experimental system by cooling and condensation of pre-filled steam in a confined vessel has been designed. The experiment

provides sets of data for both mechanistic understanding and validations of our proposed models. A parametric model consisting of a set of coupled ordinary differential equations has been established, which helps to reveal various parametric effects on the depressurization process. The simplified assumptions in the parametric model include the lumped heat capacity approximations for chamber walls, cooling coils and the gas phase. To further quantify the thermal non-equilibrium characteristics of the dynamic process, a transient and full-field simulation of computational fluid dynamics (CFD) has also been conducted. One important step in the CFD modeling is to development of an appropriate boundary condition on cooling coil surfaces where condensation occurs, which is then implemented through a user-defined function (UDF) into the commercial code FLUENT. While the majority of gas component in the chamber is condensable steam vapor, there also exists a small amount of air residue in the gas phase. Hence, both parametric and CFD models regard the gas phase as a mixture of condensable vapor and non-condensable gas (air in our case).

5.2 Experimental System of Depressurization

The objective of this experimental approach is to quantify the transient characteristics of pressure change in the cooling-induced depressurization process. Besides, the simultaneous measurements of temperature at several monitoring locations are also needed to investigate the dynamic change and non-uniformity of temperature distribution over the depressurization chamber. Thus, the experimental system of depressurization is designed to include a thermally-insulated chamber containing saturated condensable gas,

a cooling coil through which coolant passes, and various flow control and measurement devices, as shown in Figure 5.2.

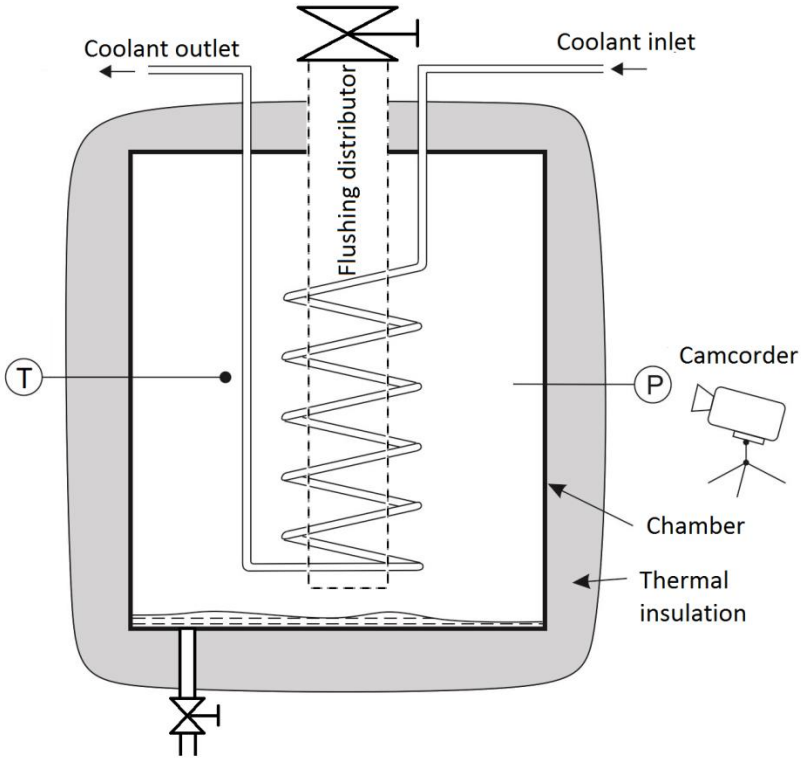

Figure 5.2 Schematic experimental system of condensation-induced depressurization.

The chamber is a stainless-steel cylindrical container with an inner volume of 0.11 m^3 and a mass of 12.7 kg. Saturated steam at 373 K is prefilled into the chamber, with a small amount of residual air as non-condensable gas (NCG). The cooling coil, inserted inside the chamber, is a 15.24 meters long copper tube with 12.7mm-O.D. and 9.5mm-I.D. Cold water at an inlet temperature of 15°C, used as coolant, is fed through the cooling coil while steam condensation occurs on the outer surface of the cooling coil. The mass flow rate of water can be controlled in a range from 0 to 0.35 kg/s. A vacuum

pressure gauge, made by NOSHOK with a gauge pressure range from -101 kPa to 101 kPa, is used to monitor the chamber pressure. The pressure gauge readability is 1.7kPa or ±1% of full scale. A digital camcorder is used to record the dynamic change in vacuum pressure readings during the depressurization process. Type-K grounded thermocouples (4.8mm in diameter; made by OMEGA) are used to monitor the transient change of temperature and provide some validation information for the CFD study of thermal non-uniformity. The thermocouples are connected to a computerized data acquisition system to monitor the transient changes in temperature. The dash-lined part in Figure 5.2 is a tubular distributor for steam-filling from boiler.

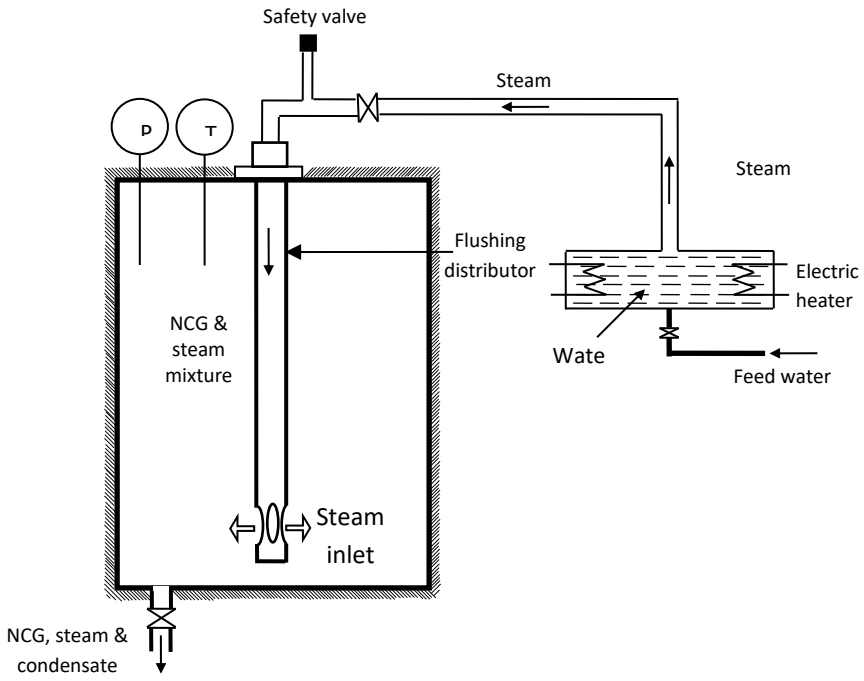

Figure 5.3 Steam filling and NCG flushing system.

The NCG flushing and steam-filling system, schematically shown in Figure 5.3, has been previously developed by our research team (Patel *et al.*, 2011) and is used in this study to pre-fill the saturated steam into the chamber before the depressurization. The steam can be continuously generated from a water boiler and then discharged from the flushing steam tubular distributor located in the center of the chamber to replace the mixed steam and NCG by pure steam. This provides the initial condition for our depressurization process.

5.3 Theoretical Modeling of Depressurization

The depressurization rate in the chamber is governed by the condensation rate of vapor on the cooling coil, which affects in turn on the condensation rate by limiting the boundary-layer cooling rate and vapor availability to the cooling surface. Hence, the determination of either depressurization rate or cooling rate has to involve the transient decrease in pressure, the two-way coupling of mass and heat transfer on the cooling coil surface with vapor condensation, the coolant flow rate and inlet conditions, the motion of vapor towards cooling coil surface, the thermal storage effects of chamber wall and internals, and non-uniform field in vapor temperature, and the effect of NCG.

The primary objectives of theoretical modeling are to explore and quantify the mechanistic effects of thermal non-equilibrium and various key parameters on the transient characteristics of condensation-induced depressurization. In this study, two modeling approaches are developed: (1) a sub-lumped parametric model to provide quick predictions of some major parametric effects on rate of depressurization, and (2) a

transient full-field numerical simulation to explore the phase transport and field non-uniformity during the depressurization process.

5.3.1 Parametric Model

Optimal design and operation of a system calls for quick predictions of major parametric effects on targeted system performance. To this end, we have developed a simple parametric model for the quantitative analysis on dynamic characterization of depressurization, without omitting any dominating system elements. To simplify the problem, the following major assumptions are introduced, which include (1) instant thermal and component equilibrium in gas-phase mixture of vapor and air, (2) neglect of the volume occupied by condensate, (3) instant thermal equilibrium between condensate and cooling system (coolant and cooling coil), (4) neglect of any thermal radiation by participating gases, (5) ideal gases for both vapor and air, and (6) lumped heat capacity model of chamber wall and internals. Consequently, there are four different characteristic temperatures, representing sub-lumps of gas mixture, cooling coil, flushing distributor, and chamber.

The total mass and energy of vapor, condensates and air in the chamber are conserved during the depressurization, which can be expressed as

$$\frac{d}{dt}(m_v + m_l + m_a) = 0 \tag{5.1}$$

$$\frac{dm_a}{dt} = 0 \tag{5.2}$$

The change of energy of vapor and air is contributed by the heat transfer with the chamber wall and internals (such as flushing distributor), energy loss to the coolant and latent heat released from condensation. Thus the energy balance of vapor mixture yields,

$$\frac{d}{dt}\left[\left(m_v c_{vv} + m_a c_{va}\right)T\right] = q_{ch} - q_p + q_{FD} + h_v \frac{dm_v}{dt} - h_{fg} \frac{dm_v}{dt} \tag{5.3}$$

where the first three terms on the right hand side are the heat transfer with chamber wall, cooling coil, and flushing distributor (with condensate), respectively,

$$q_{ch} = h_{ch} A_{ch} \left(T_{ch} - T\right) \tag{5.3-1}$$

$$q_p = h_p A_p \left(T - T_p\right) \tag{5.3-2}$$

$$q_{FD} = h_{FD} A_{FD} \left(T_{FD} - T\right) \tag{5.3-3}$$

The last two terms in Equation (5.3) stand for the enthalpy and latent heat from phase change. It should be noticed that, under the condition of steady-state film condensation, the convective heat transfer from cooling surface equals the amount of latent heat released.

The determination of heat transfer coefficients at condensation surface (h_p) is critical to the accuracy of transient results. The most commonly-used convective heat transfer coefficient in film condensation is originally proposed by (Nusselt, 1916).

However, the Nusselt's solution is based on many assumptions (*e.g.*, pure vapor, steady state with unlimited vapor condensation, latent heat carried away immediately after generated) that have to be modified in our case in order to target the transient nature of depressurization with limited amount of vapor and the presence of air (NCG). Based upon the Nusselt's approach and assumptions of instant pseudo-equilibrium and film condensation during the depressurization, we propose a time-dependent heat transfer coefficient h_p(t):

$$h_p(t) = \frac{k_l}{\delta(t)} \tag{5.3-4}$$

where $\delta(t)$ is the averaged thickness of condensate film, defined by

$$\delta(t) = \frac{m_l(t)}{\rho_l A_p} \tag{5.3-5}$$

where A_p is the outer surface area of cooling coil. Combining Equations (5.3-4) and (5.3-5) gives rise to

$$h_p(t) = \frac{k_l}{m_l(t)} \rho_l A_p \tag{5.3-6}$$

The presence of even a small amount of air (NCG) can significantly affect the condensation rate e.g., (Minkowycz and Sparrow, 1966; Sparrow *et al.*, 1967; Collier, 1994). Thus, a non-condensable correction factor (C_{NC}) is included to modify Equation (5.3-5.6) so that,

$$h_p(t) = C_{NC} \frac{k_l}{m_l(t)} \rho_l A_p \tag{5.3-7}$$

In this study, C_{NC} is taken as 0.012 as suggested by Collifer and Thome (1994).

Convective heat transfer coefficients at the inner chamber wall and flushing distributor (FD) are estimated, respectively, by

$$h_{ch} = \frac{Nu_{ch} \cdot k_v}{L_{ch}} \tag{5.3-8}$$

$$h_{FD} = \frac{Nu_{FD} \cdot k_v}{L_{FD}} \tag{5.3-9}$$

where the Nu numbers for both equations 5.3-8 and 5.3-9 are calculated from the empirical correlation (Churchill and Chu, 1975):

$$\overline{Nu_L} = \left\{ 0.825 + \frac{0.387 Ra_L^{1/6}}{\left[1+\left(0.492/\mathrm{Pr}\right)^{9/16}\right]^{8/27}} \right\}^2 \tag{5.3-10}$$

The lumped heat capacity model for the cooling coil and condensate can be expressed by

$$\frac{d}{dt}\left[\left(m_p c_p + m_l c_l\right) T_p\right] = -q + q_p + q_{r,p} + h_l \frac{dm_l}{dt} \tag{5.4}$$

where the first two terms in the right hand side indicate the heat discharged to the coolant, and heat absorbed from the gas phase lump, respectively. The last term on the left indicates the mass-transfer-induced energy gain from condensate. The heat discharged to the coolant is expressed as:

$$q = \dot{m}_c c_c \left(T_{co} - T_{ci}\right) \tag{5.4-1}$$

where T_{co} can be calculated by:

$$T_{co} = \left(288 - T_p\right) e^{-\frac{h_c A_p}{\dot{m}_c c_c}} + T_p \tag{5.4-2}$$

The energy equation for chamber and flushing distributor can be expressed, respectively, as,

$$\frac{d}{dt}\left(m_{ch}c_{ch}T_{ch}\right) = -q_{ch} + q_{r,ch} \tag{5.5}$$

$$\frac{d}{dt}\left(m_{FD}c_{FD}T_{FD}\right) = -q_{FD} + q_{r,FD} \tag{5.6}$$

The radiation among coil, flushing distributor and chamber wall is considered as surface-to-surface radiation, with all three surfaces assumed to be diffusive and grey. The radiation heat transfer and the associated view factors are given as:

$$q_{r,i} = \sum_{j=1}^{3} \frac{\sigma(T_j^4 - T_i^4)}{\left(\frac{1-\varepsilon_i}{\varepsilon_i A_i} + \frac{1}{A_i F_{ji}} + \frac{1-\varepsilon_j}{\varepsilon_j A_j}\right)} \tag{5.6-1}$$

$$F_{ij} = \begin{pmatrix} 0 & 0.548 & 0.452 \\ 0.047 & 0.907 & 0.046 \\ 0.474 & 0.474 & 0.051 \end{pmatrix} \tag{5.6-2}$$

where subscripts 1, 2, 3 are denoted for flushing distributor (*FD*), chamber wall (*ch*) and cooling coil (*p*), respectively. Since the low-pressure gas can be practically regarded as ideal gas, according to the Dalton's law, the total pressure is the sum of partial pressures of vapor and air components:

$$p = p_a + p_v \tag{5.7}$$

And

$$m_v = \frac{p_v V}{R_v T} \tag{5.8}$$

$$m_a = \frac{p_a V}{R_a T} \tag{5.9}$$

It is further assumed that the steam vapor maintains saturated during the condensation, so the Clapeyron-Clausius equation can be applied independently to relate its partial pressure to the temperature,

$$\frac{dp_v}{dT} = \frac{p_v h_{fg}}{R_v T^2} \tag{5.10}$$

In summary, the parametric model consists of ten independent equations (Equations. 5.1-5.10) and ten independent variables (m_v, m_l, m_a, p_v, p_a, p, T, T_{FD}, T_{ch}, T_p). Hence, the problem is closed. With the proper initial conditions, these time-dependent variables become solvable.

5.3.2 Transient Full-field Model and Simulation

The determination of condensation rate (and hence depressurization rate) depends upon the accurate account of the local heat transfer rate and vapor flow rate to the cooling coil surface, which has to be determined from the transient and locally-coupled field distributions of transport properties such as temperature, velocity and concentration of the gas phase. In reality, an instant thermal equilibrium or uniform temperature distribution of the vapor and air mixture within the chamber cannot be ensured during the depressurization process. Consequently, it is needed to understand if and how temperature measurement devices (such as thermal couples) can be used to monitoring the transient depressurization.

To explore the transient and field distributions in temperature, velocity and concentration of vapor-air mixture by the cooling-induced condensation and resulted depressurization, a transient full-field simulation of the depressurization process is conducted. Besides the governing equations and boundary conditions in the general computational fluid dynamics (CFD) modeling, additional constitutive equations for the surface condensation and resulted phase transfer also need to be developed, which are then implemented to modify the boundary conditions on the cooling coil surface. From coding point of view, we take the advantage of the commercial CFD code of ANSYS FLUENT (version 12.1) and modify it by use of the user-defined function (UDF) as source term in a thin boundary layer for the surface condensation, which is based on the condensation model developed in this study. For simplification, the system is approximated as axial-symmetric with laminar flow (based on CFD result and chamber

size, the maximum Re number is around 200). Besides, Species Transport Model without reaction is enabled for the multi-component gas. The buoyancy effect is also included.

To ensure the computational efficiency without losing any major mechanisms and accuracy, several assumptions are made with the following justifications. (1) The temperature of coil surface is uniform, due to the high thermal capacity and flow rate of coolant as well as the high thermal conductivity of cooling coil. (2) The depressurization chamber is assumed to be thermally insulated without any heat loss to the surrounding. (3) The gas mixture is transparent to thermal radiation without any irradiative absorption or scattering. (4) Due to the much lower temperature on coil surface comparing to the surrounding gas, any latent heat released from condensation is considered transferring to the cooling coil only. A summary of major assumptions is listed in the following:

- Ignore the liquid phase of condensation water;
- Vapor is considered as saturated ideal gas;
- No turbulence occurs during the depressurization process;
- Temperature of coil surface equals coolant inlet temperature;
- Thermal insulated chamber wall has no heat loss to its surrounding;
- Ignore any thermal radiation by participating gases;
- Latent heat attributes only to the cooling coil.

In the confined chamber with condensate discharge, the decreased mass of steam equals to the amount of condensate generated while the energy loss of steam is balanced by the net of heat taken away by coolant and latent heat released from condensation formation and its discharge out of chamber. Hence, the conservation equations of mass,

momentum and energy on each micro unit of vapor and air could be expressed, respectively,

$$\frac{\partial}{\partial t}(\rho Y_i) + \nabla \cdot (\rho \mathbf{U} Y_i) = -\nabla \cdot \mathbf{J_i} + S_i \tag{5.11}$$

$$\frac{\partial}{\partial t}(\rho \mathbf{U}) + \nabla \cdot (\rho \mathbf{U}\mathbf{U}) = -\nabla p + \nabla \cdot \boldsymbol{\tau} + S_v \mathbf{U} \tag{5.12}$$

$$\frac{\partial}{\partial t}(\rho E) + \nabla \cdot \left[\mathbf{U}(\rho E + p)\right] = \nabla \cdot \left[k \nabla T - \sum_i h_i \mathbf{J_i} + (\boldsymbol{\tau} \cdot \mathbf{U})\right] + S_h \tag{5.13}$$

where the subscript of *i* can be either *v* or *a*, representing the species of steam vapor or air. Species conservation yields，

$$\sum Y_i = 1 \tag{5.14}$$

Diffusive flux of species *i*, $\mathbf{J_i}$, is related to concentration gradients by,

$$\mathbf{J_i} = -\rho D_{i,m} \nabla Y_i \tag{5.15}$$

S_h is volumetric heat source, and S_i is the mass source for the i^{th} species. Obviously, the mass of air (as NCG) keeps the same along depressurization,

$$S_a = 0 \tag{5.16}$$

whereas, for vapor, there is a negative mass source, representing the condensation rate per unit volume. The condensation is implemented as a source term in conservation equation. Most film condensation models *e.g.* (Dhir and Lienhard, 1971; Incropera and DeWitt, 2011) are developed for condensation from pure vapor without NCG. Since a small portion of NCG can reduce the overall heat transfer rate significantly, non-condensable factor must be included into this study. Thus, a revised unit length condensation rate with NCG effect is proposed based on existed model for horizontal tube (Incropera and DeWitt, 2011), as,

$$S_v = -Coe \cdot \frac{0.729\pi}{L_{coil}} \left[\frac{g\rho_l \left(\rho_l - \rho_v\right)}{N\mu_l} \right]^{\frac{1}{4}} \left[\frac{Dk_l \left(T_{sat} - T_w\right)}{h_{fg}} \right]^{\frac{3}{4}} \tag{5.17}$$

where Coe is a coefficient account for the presence of NCG, which may be related to the concentration (or mass fraction) of NCG as (Kim and Corradini, 1990; Anderson *et al.*, 1998),

$$Coe = \left[1 - 0.964 Y_{NCG} + 4.989 Y_{NCG}^2 - 4.135 Y_{NCG}^3 \right] \cdot \frac{1 - Y_{NCG}}{1 + 15.48 Y_{NCG}} \tag{5.18}$$

To close the problem, the equation of state is further included according to the ideal gas assumption of the vapor and air mixture:

$$\frac{p}{\rho} = R_g T \tag{5.19}$$

For chamber wall and flushing distributor, the governing equations of energy conservation equation are:

$$\frac{\partial}{\partial t}\left(\rho_j h_j\right) + \nabla \cdot \left(\mathbf{U}\rho_j h_j\right) = \nabla \cdot \left(k_j \nabla T_j\right) + S_{h,j}, \quad j = ch, FD \tag{5.20}$$

The second term in the right hand side of equation 20 includes radiation simulated by Surface to Surface (S2S) model within the ANSYS-Fluent software.

In summary, there are total nine unknowns (ρ, p, Y_v, Y_a, T, $\boldsymbol{U}(2)$, S_v, T_{ch}, T_{FD}) and nine independent equations (5.11(2), 5.12(2), 5.13, 5.14, 5.19, 5.20(2)) in this CFD model, hence the problem is closed.

The temperature of condensation surface of cooling coil is varying and set to be the same value as the coolant. The variation time is calculated based on coolant flow rate, coil inner diameter and coil length. The outside surface of chamber wall is set as thermal insulated boundary (i.e., q_w=0).

$$T = \begin{cases} 373 - \dfrac{85}{3.096} t, & t < 3.096s \\ 288, & t \geq 3.096s \end{cases}\Bigg|_{@coil\ surface} \quad ;\ \dot{q} = 0\Big|_{@\text{chamber outside surface}}$$

The initial conditions include all zones at a temperature of 373 K, and the mole fraction of NCG is 0.1. (This value is selected to be identical with experimental condition, referring to *Operating Conditions* section.)

$$T_{Gas} = T_{ch} = T_{FD} = 373K, Y_{NCG} = 0.1\Big|_{t=0}$$

The source terms (mass, momentum and energy) are applied to an annulus region over the outer boundary of cooling coil with 2 mm of thickness (a typical size of a water droplet). With the above boundary and initial conditions, these PDEs are solvable.

Geometric complexity can drag down the computing speed without providing more convincing results relating to the main purpose of CFD modeling, which is exploring the non-uniformity of temperature and other field properties. Thus, several geometric simplifications are made as conceptually shown in Figure 5.4-a: (1) Axial-symmetric is assumed; (2) Spiral cooling coil is simulated as an array of rings with the equivalence to the total surface areas and number of spirals; (3) Flushing distributor is simplified as a solid rod with its total thermal capacity unchanged. The mesh distribution used in this study is displayed in Figure 5.4-b, with total number of about 18000.

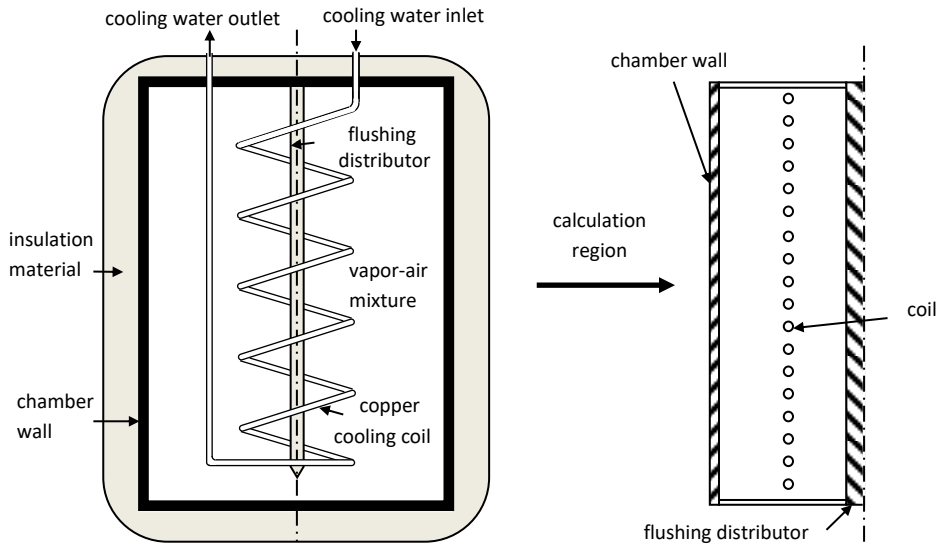

Figure 5.4-a Geometry simplification and simulation domain.

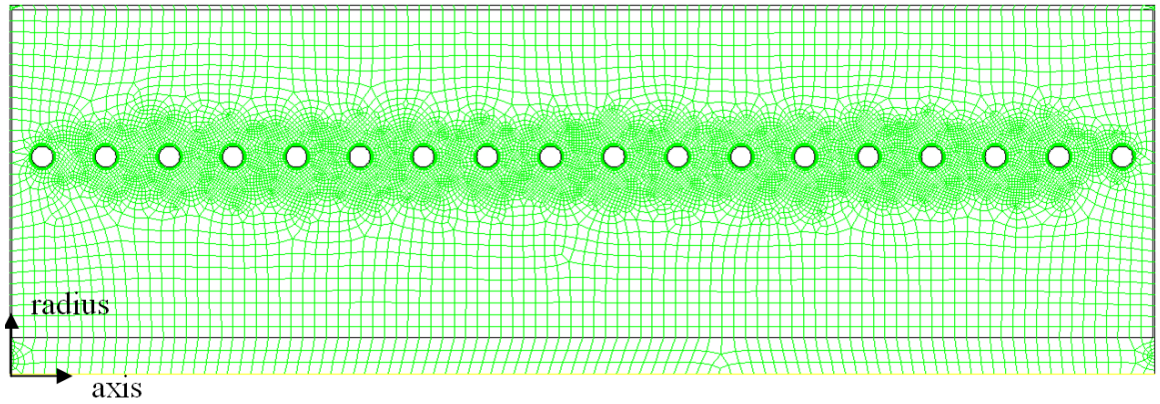

Figure 5.4-b Mesh distribution of computational domain.

5.4 Results and Discussion

Both parametric and CFD models are solved with proper boundary and initial conditions. The former (with ODEs) is solved numerically via 5th Runge-Kutta method, while the latter (with PDEs) is solved via commercial code (ANSYS Fluent 12.1) with UDF coupling. To validate these models, identical operating conditions with the experiment

are applied. Meanwhile, parametric studies on key parameters have been conducted through the parametric model. These results and discussions are stated in the following sub-sections.

5.4.1 Operating Conditions

The volume flow rate of coolant, with room temperature (288 K), is set as 21 L/min. Initially, the steam vapor and NCG mixture is at atmosphere pressure (101 kPa) and its temperature is 373 K. Based on the experiment data of final stage pressure, the volume fraction of NCG is estimated at approximately 10%. The non-condensable correction factor (C_{NC}) in parametric model is thus taken the value as 0.012 for 10% of NCG as suggested by Collifer and Thome (1994). The properties of related material are listed:

Table 5.1 Material Property

	ρ (kg/m^3)	Cv (J/kgK)	ε	K (W/mK)
Chamber wall (steel)	8030	490	0.79	16.27
Flushing distributor (cast iron)	7200	460	0.78	55
Cooling coil (copper)	8978	390	0.65	387.6
Vapor	Ideal gas law	1410.8	N/A	0.0261
NCG/air	Ideal gas law	716.7	N/A	0.0242

5.4.2 Model Validation

Figure 5.5 shows the comparison of the pressure variation during depressurization process between experiment, parametric and CFD models. The experiment result shows pressure sharply decreasing at beginning and gradually slowing down. In the end, the

pressure falls on the asymptotic value which indicates the partial pressure of NCG. The results of parametric and CFD model agree with experiment data reasonably well either for dynamic or asymptotic characteristics. It can be observed that both models have a quicker depressurization rate than the experiment data. Consider the pressure gauge response time (although is very small) and the challenges in both modeling and the measurements, the discrepancies between both models and experiment are in general still reasonably small.

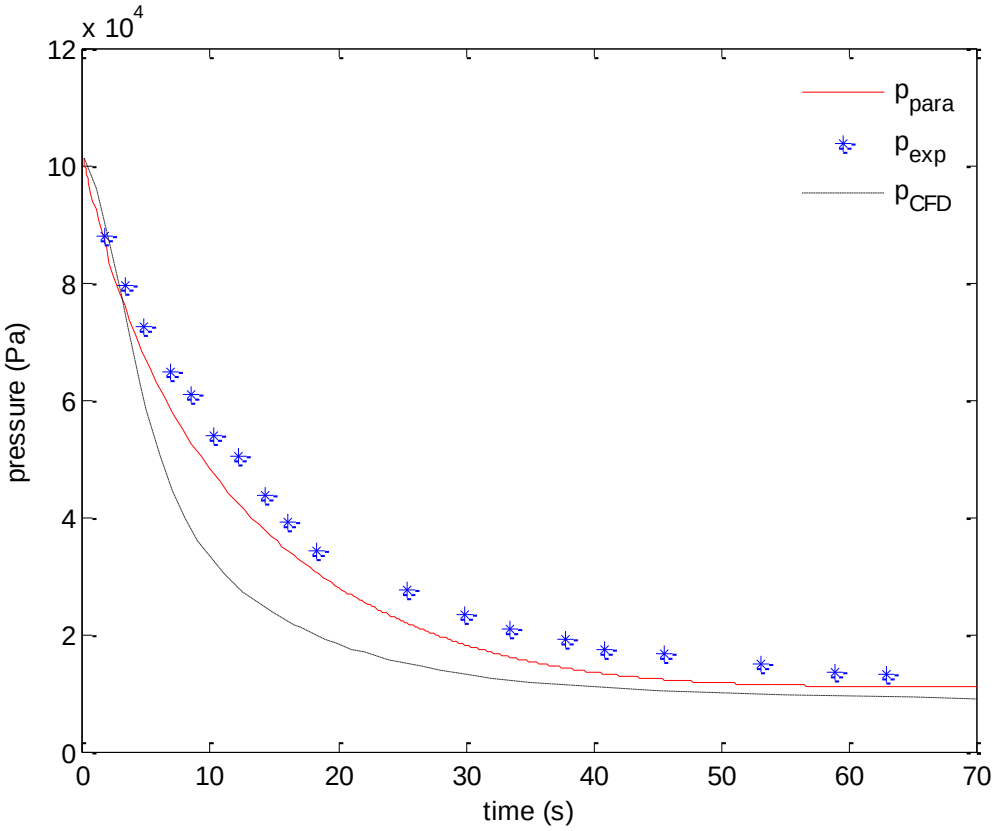

Figure 5.5 Variation of pressures.

Figures 5.6 and 5.7 illustrate distributions of temperature and NCG mass fraction during the depressurization at 5, 25 and 60 seconds. The temperature and NCG concentration contours clearly show inhomogeneous characteristic of temperature and

NCG and reveal the mass and energy diffusion along the depressurization. The temperature inhomogeneous distribution and transition may due to two main reasons: 1, heat transfer from cooling coil and chamber wall, which is a more dominated factor around all solid surfaces; 2, gas state change, which is for the whole field and due to the gas pressure and density change described by ideal gas law. The temperature is higher near the chamber wall and flushing distributor due to the thermal storage effect and also higher at top because of the gravity.

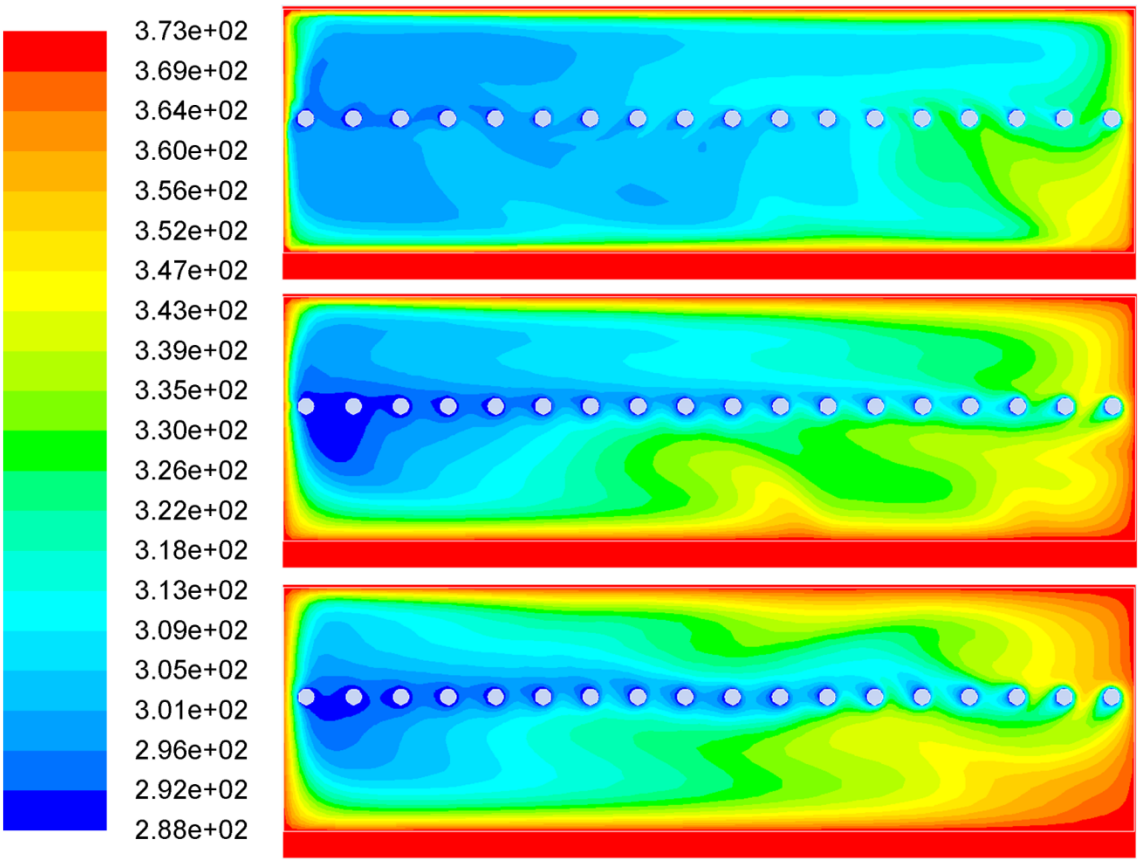

Figure 5.6 Variation of temperature distribution (K), time from top to bottom: 5, 25, 60s.

As reflected in Figure 5.7, Accumulation of NCG around coil surface decelerates the condensation rate. And steam residual is trapped in the center space of the top around

the flushing distributor due to the gravity effect. As the depressurization commences, the mole fraction of NCG becomes dominant everywhere inside the chamber, which is a good reflection of the degree of condensation.

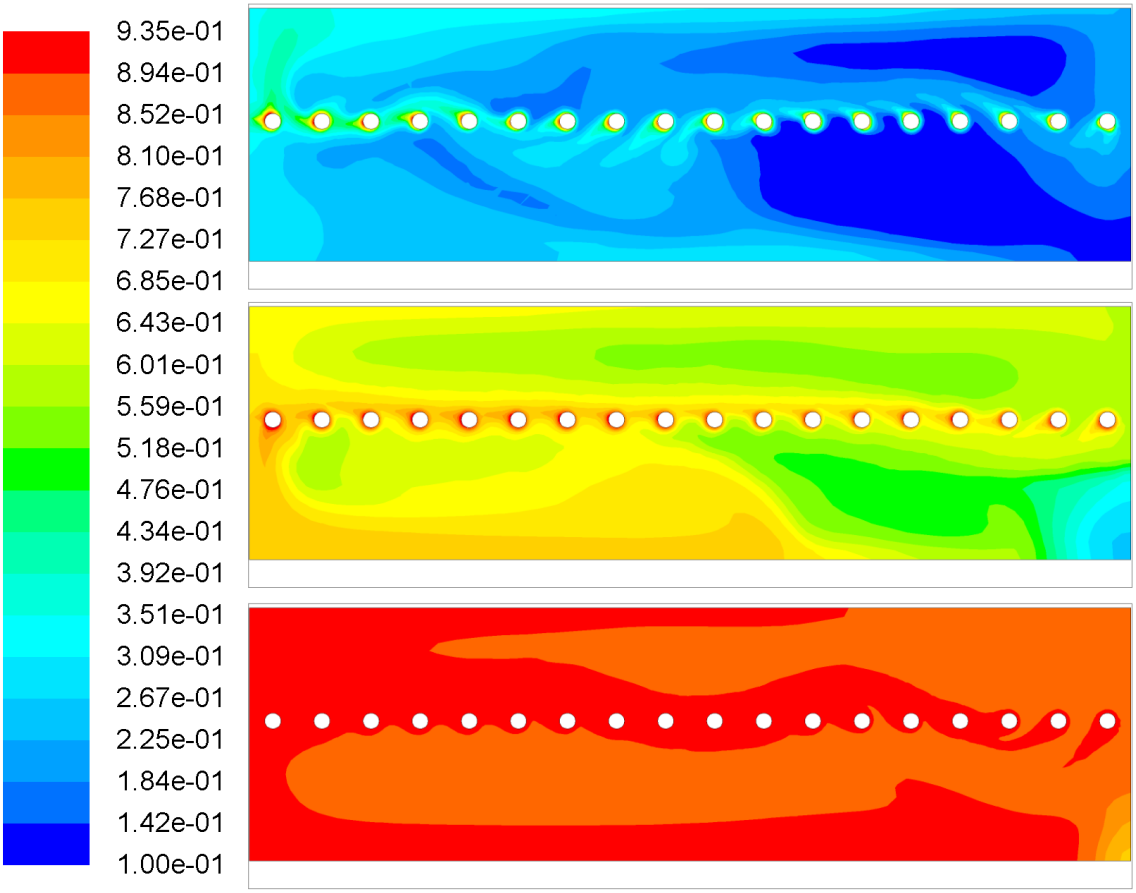

Figure 5.7 Variation of NCG mass fraction distribution.

Figure 5.8 depicts temperature variation during depressurization for experiment, saturated value based on experiment and parametric model, plus other variables such as temperatures of chamber and cooling coil, respectively. The result of parametric model matches experiment value reasonably well in the earlier stage which is in a saturated state. For later stage the results show larger difference due to non-saturated state and the thermal non-equilibrium effect. For the temperature of the CFD result, since the

temperature field is never homogeneous, it is impractical to compare experiment or parametric model result to any "averaged" CFD result. The detailed nature of non-uniformity in temperature with localized condensation is further investigated by the CFD model as shown previously. Figure 5.8 also depicts quite different time scale of cooling period for coil and chamber comparing to gas mixture. It can be seen that the cooling time scale for coil is within seconds and for gas mixture is in 10s of seconds. It may take hours for chamber to fully cool down because of its large heat storage and small leakage. The black dash line separates condensation stage from after-condensation stage, telling us that the depressurization process is happening in condensation stage within a very small time-scale.

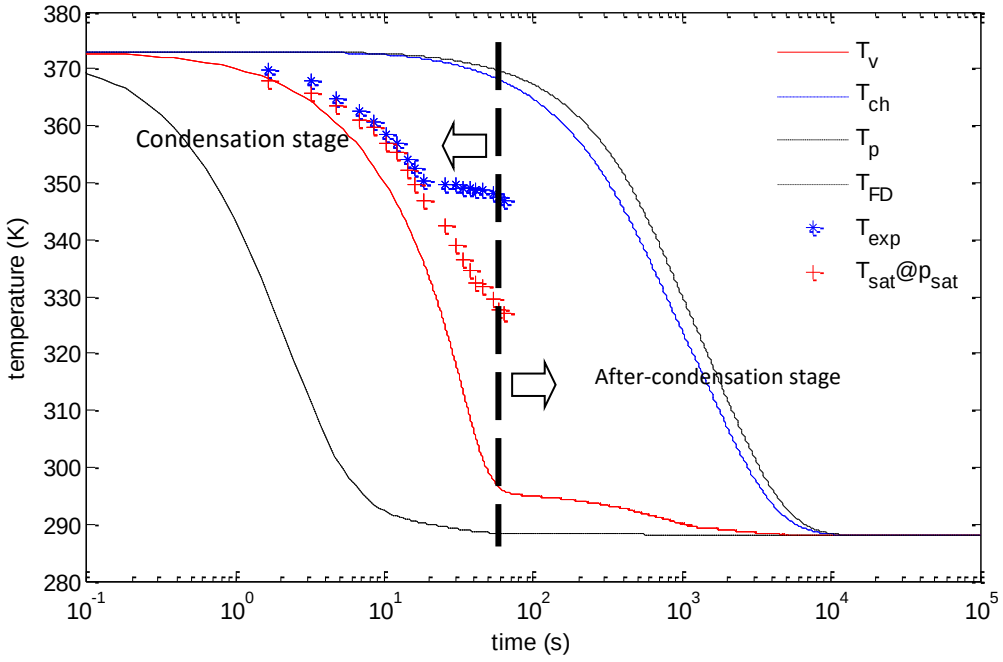

Figure 5.8 Variation of temperatures.

Figure 5.9 shows the vector of velocity nearby cooling coil, and reflects the existence of condensation-induced suction and buoyancy effect, which enhances convective heat transfer under the condensation and gravity effects. It also indicates the maximum velocity is only in a scale of decimeter per second, which ensures the flow has a small Re number (Re_{max}~200), and is within laminar regime as we assumed.

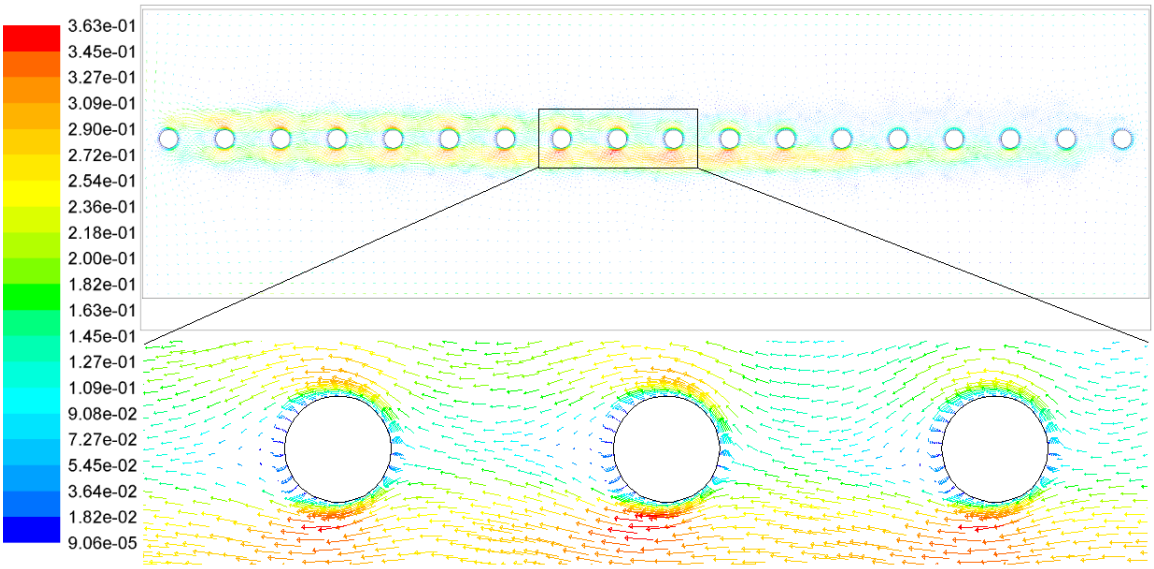

Figure 5.9 Velocity field vector at t=1.0 s (unit, m/s) .

Figure 5.10 shows the variation of gas phase density and condensate mass per unit volume. It can be seen that the mass of gas keeps transferring into mass of liquid as condensation continues, and the total mass is balanced as shown in Figure 5.11.

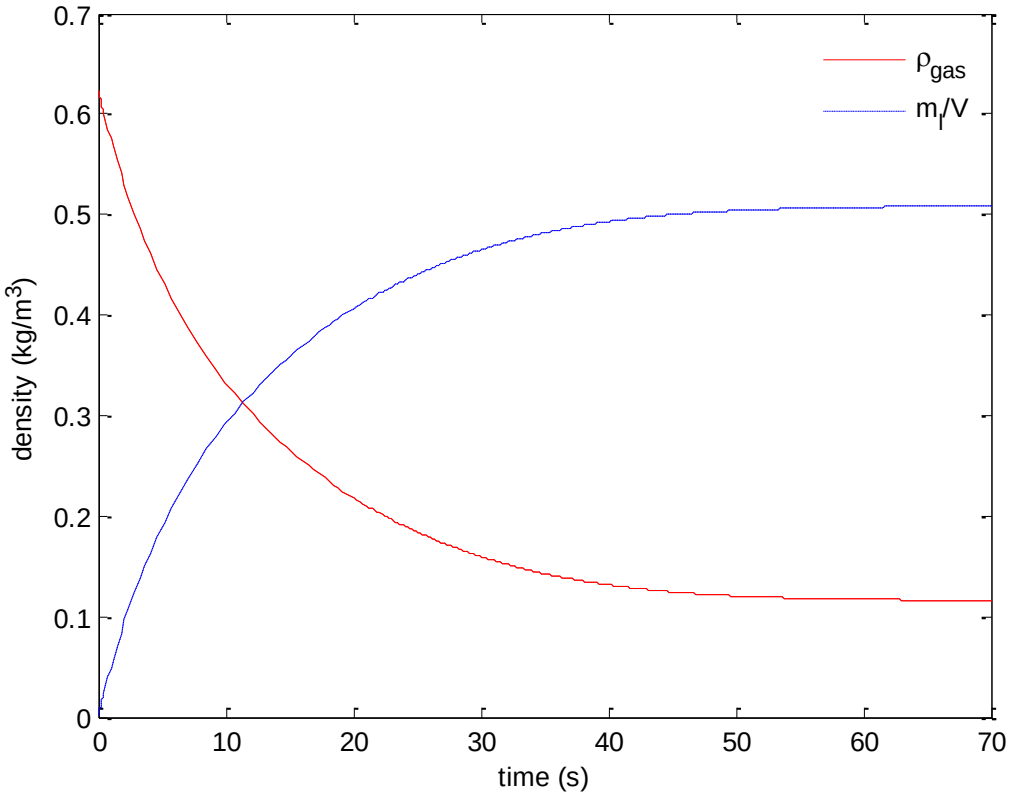

Figure 5.10 Variation of gas density and mass per unit volume of condensate.

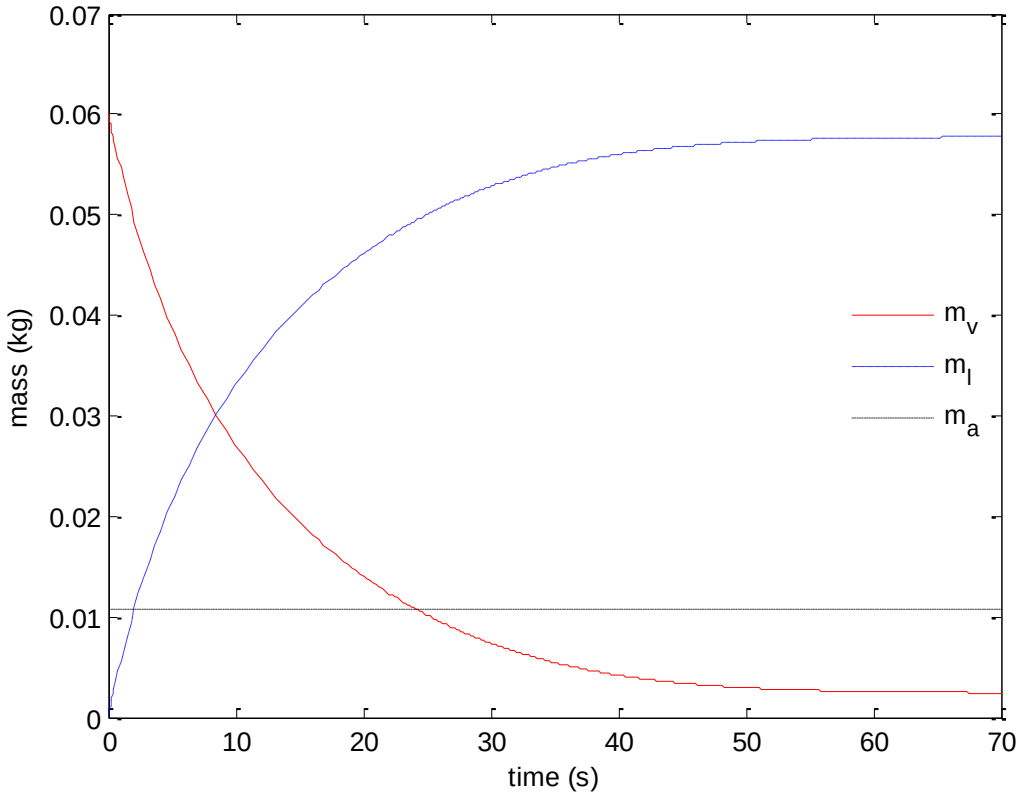

Figure 5.11 Variation of the mass of gas and condensate.

Figures 5.12-a and 5.12-b give a visual impression of the scale of variation of heat flux through different surfaces. These figures show that at first several seconds, heat flux carried away by coolant (q) is one order of magnitude greater than that of film condensation surface (q_p). This discrepancy is responsible for the condensation-induced heat transfer and storage effect as indicated by the governing Equation 5.4. Then both heat flux reduce and fall into the same scale after about 10 seconds. It is noted that heat flow through chamber inner surface (q_{ch}) is very small at the beginning and gradually increase (due to enhanced radiation and convection by the ever increasing temperature gradient near chamber surface) to the same order of magnitude of q and q_p.

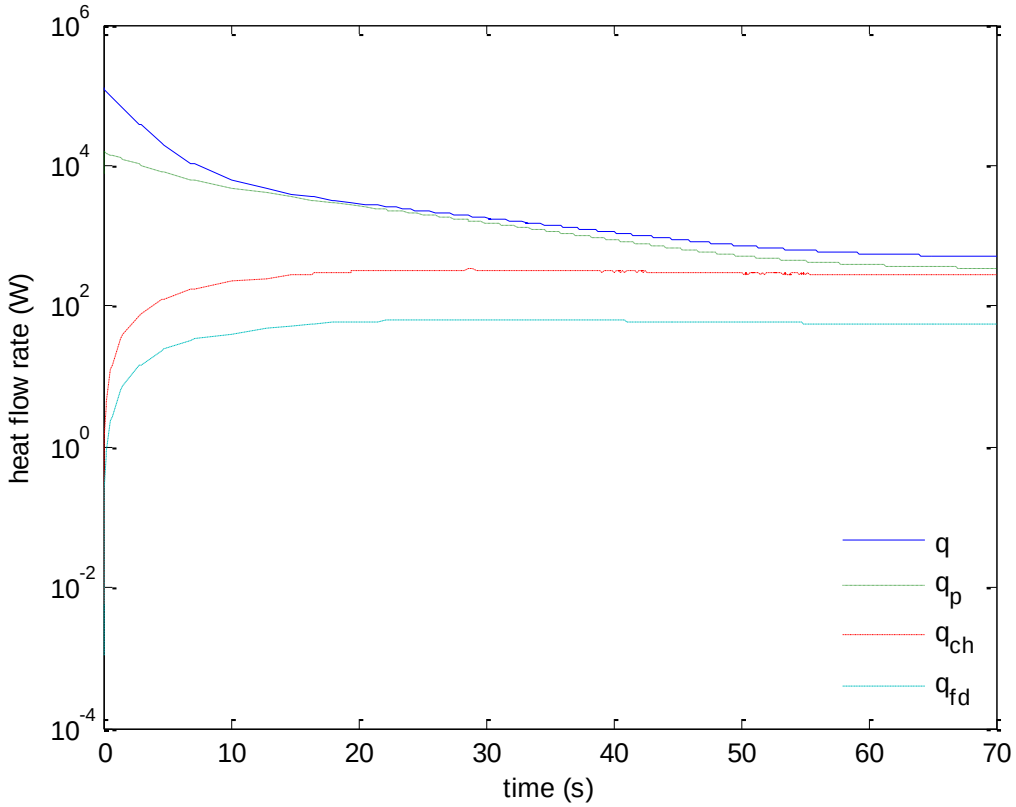

Figure 5.12-a Variation of heat flux at different surfaces.

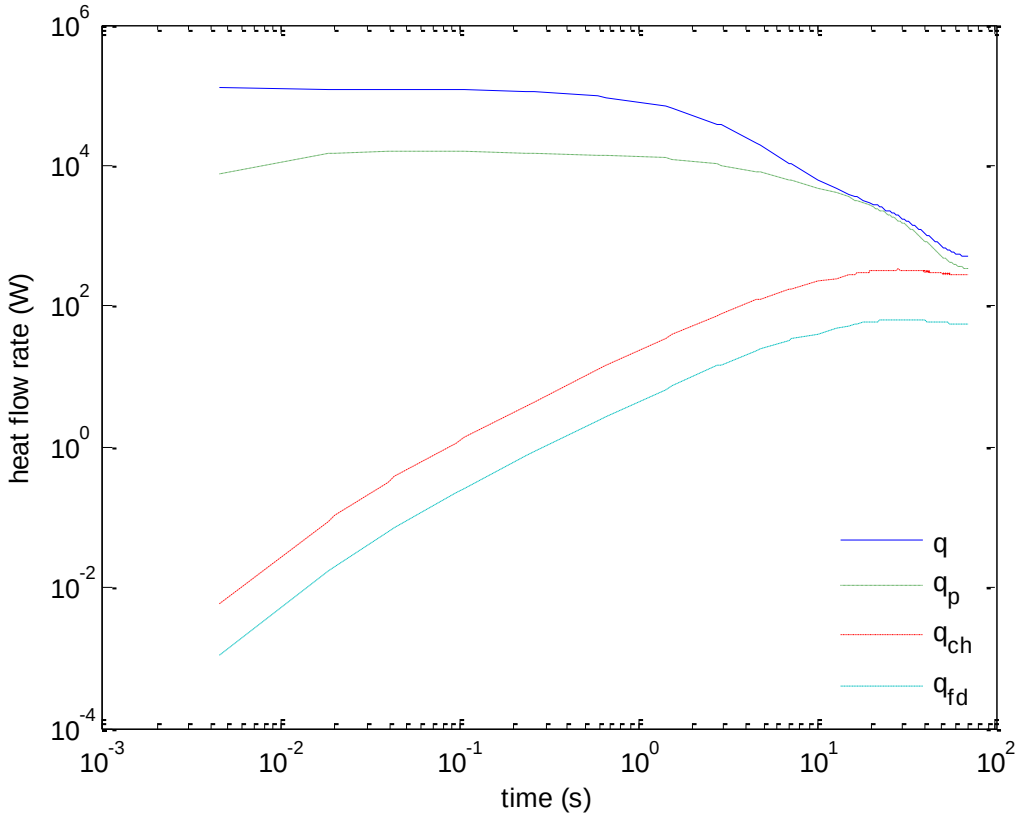

Figure 5.12-b Variation of heat flux at different surfaces (time log-scale).

5.4.3 Parametric Study

Figure 5.13 shows the effect of coolant flow rate on depressurization. The result is as expected that the higher the coolant flow rate, the faster the depressurization rate. It should be noted that, a limit flow rate of coolant (such as 21 L/min) exists. The depressurization rate can't surpass certain rate since the coolant reaches its heat absorbing limit. This is a good guidance for future design to avoid unnecessary coolant waste and conserve pumping energy.

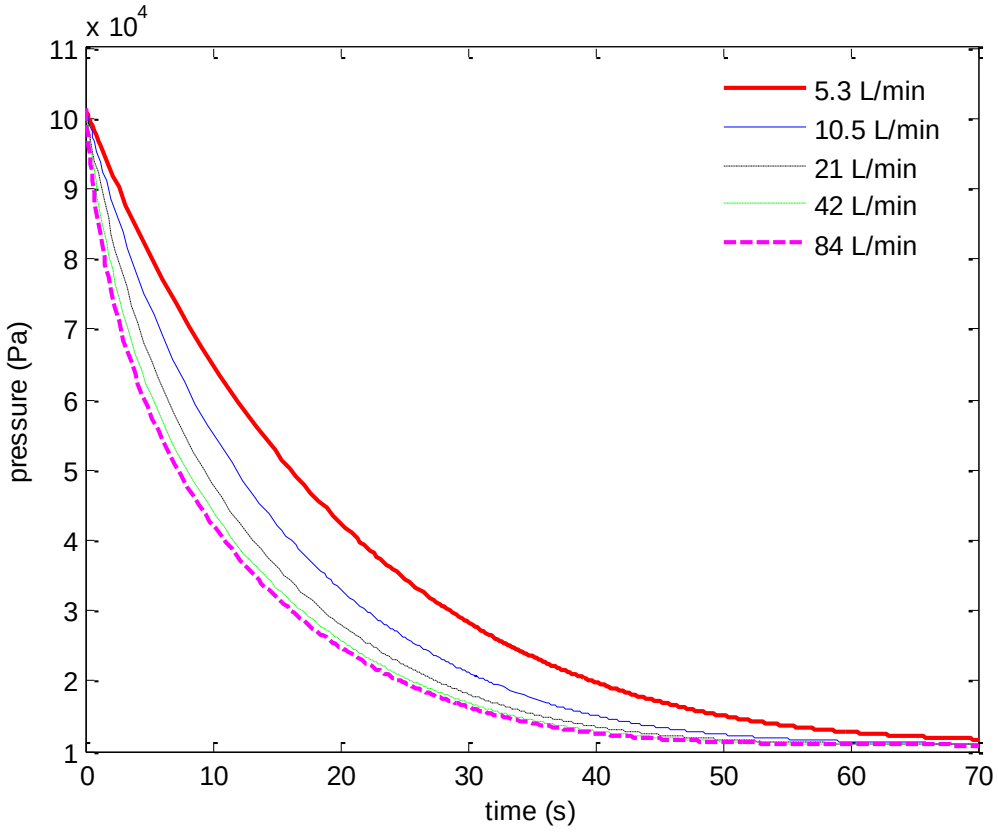

Figure 5.13 Effect of coolant flow rate on depressurization.

Figure 5.14 shows the effect of cooling surface area on depressurization. The result is also as expected just like the previous one, that the bigger the surface area, the faster the depressurization rate, which is sensitive to cooling area. However, unlike the coolant flow rate, the cooling surface does not have an "sufficient amount" concept. Due to the lump-capacity assumption, bigger cooling surface can lead to much higher depressurization rate, and vice versa.

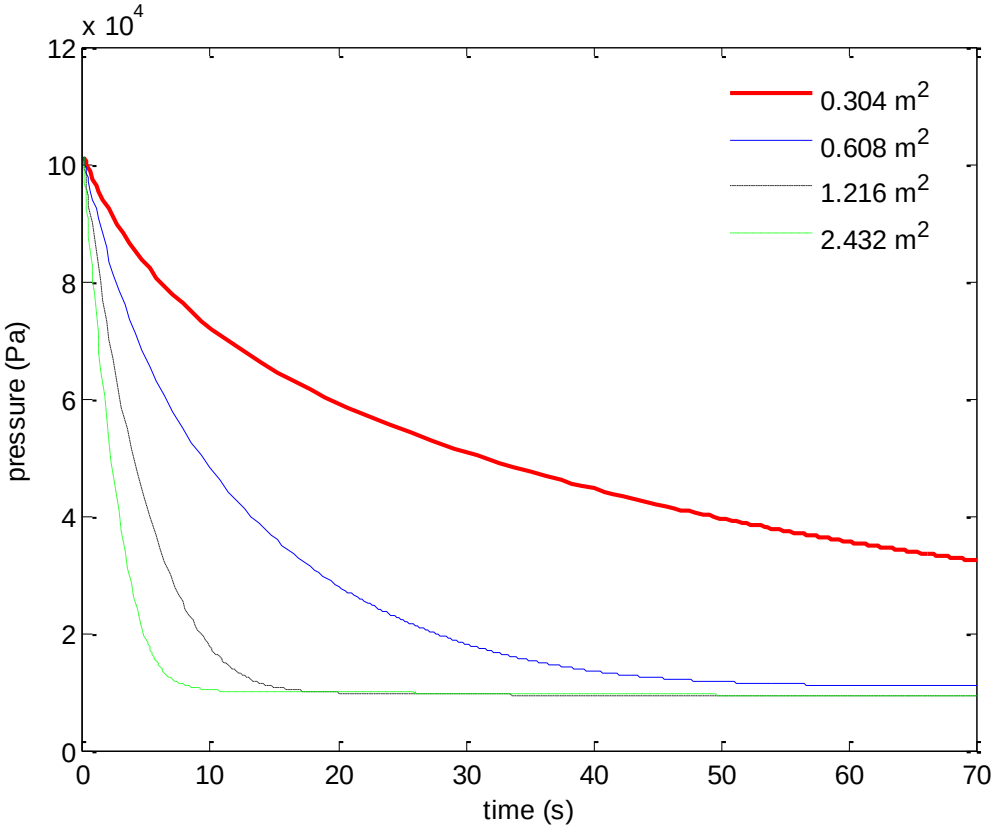

Figure 5.14 Effect of cooling coil surface area on depressurization.

From Figure 5.15, it can be observed that as long as maintaining same ratio of cooling surface and coolant flow rate to chamber size, the depressurization rate will have a relatively similar time scale regardless of scaling-up. This figure indicates a potential scalability of this condensation-induced depressurization method.

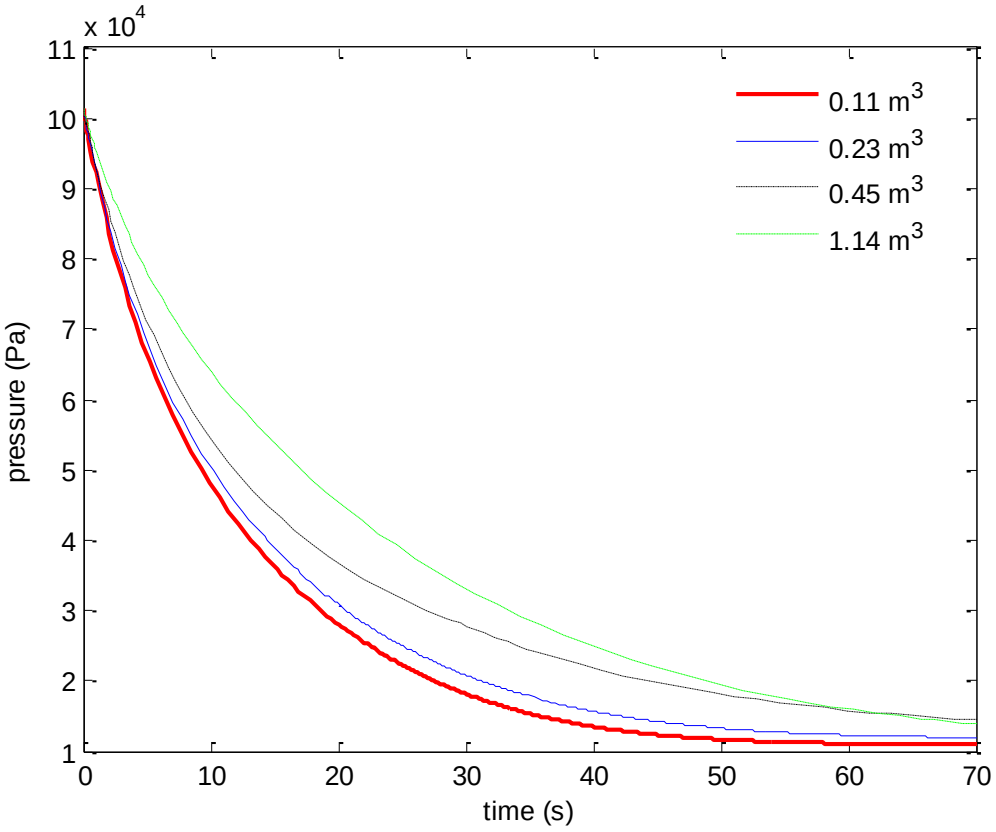

Figure 5.15 Effect of vessel volume and cooling coil surface area on depressurization.

Figure 5.16 shows the NCG effect on the depressurization rate. The C_{NC} coefficients are selected by the reference (Collifer and Thome, 1994) as 0.1, 0.05 and 0.008 for NCG initial percentage of 1%, 5% and 20%. The result shows that, obviously higher percentage of NCG will not only lead to higher terminal pressure but also reduce depressurization rate. This indicates a trade-off between higher depressurization quality from higher purity of vapor and the cost of generating higher purity.

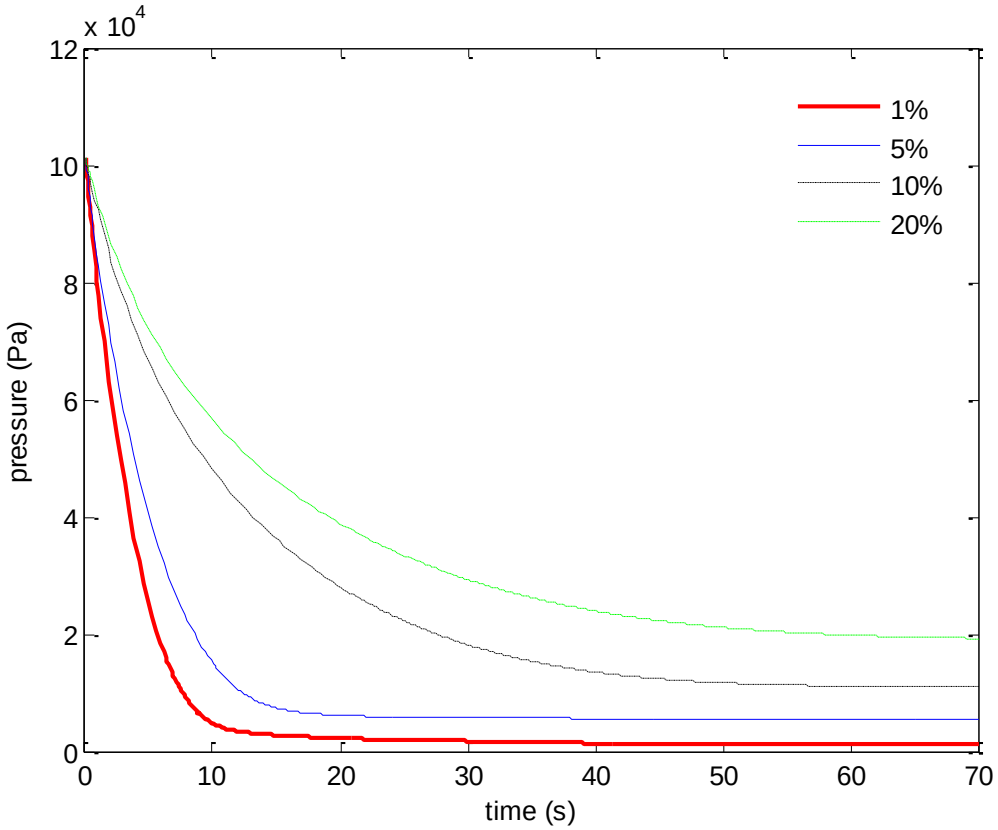

Figure 5.16 NCG effect on depressurization

5.5 Conclusion

In this study, an experimental system of condensation-induced depressurization is designed and built up. The measurement shows asymptotic depressurization with rapid changes at the beginning. A parametric model and a full-field CFD model are developed, respectively, for the parametric predictions of system depressurization and for the understanding of effects of non-equilibrium in phase transport on the depressurization process. The former is based on four sub-lumped capacity models with instant thermo-equilibrium in each lump, while the latter considers the phase non-uniformity and thermal non-equilibrium within the depressurization system. Both models provide correct

predictions in both transient and asymptotic depressurization characteristics, with reasonable agreement to the corresponding measurements. The CFD results show that not only the temperature is non-uniformly distributed within the system but also the transient characteristics of temperature lags behind that of depressurization. The good agreement of both models on depressurization further indicates that the effect of thermal non-equilibrium within the system may only have a limited impact on the depressurization. The parametric predictions on effects of cooling rate, NCG fraction and vessel volume provide some useful guidance to future optimized design and operation of the depressurization by cooling-controlled condensation.

CHAPTER 6

CFD SIMULATION OF AEROSOL TRANSPORT IN THE CHAMBER

6.1 Introduction

Except the experimental approach, many literatures have showed that numerical simulation can be a very fast and efficient way to study the aerosol/particle transport in indoor environment. Both commercial and self-compiled Computational Fluid Dynamics codes are widely used. Unlike the experiments, the numerical simulation has its financially affordable and less time consuming advantages, especially for parametric study of an existed framework. The reason is because it always cost much more time and money to adjust parameters for experiment study. In short, a proper defined CFD model can be a very effective approach to study such aerosol transport problem.

However, CFD also has its own limitations. For example, due to the incompleteness of existing theoretical model, many extreme or complicated conditions are short of the backup of proper theoretical guidance. For those cases, CFD modeling always needs to be validated by experiment. In this particular study, due to the low Reynolds number, the flow field is in a weak turbulence region, which requires carefully selection of turbulence model. Besides, the natural convection in this study is ineligible but difficult to predict. The temperature difference for this study is low hence the Grashof Number is relatively small. The combination of weak turbulence and weak natural convection makes the model selection very difficult for CFD simulation. In addition, the couple discrete phase modeling should also be dealt with a lot of cautions, its trajectory

and evaporation could be significantly different by selecting different model or applying User-Defined Function (UDF).

In this Chapter, a three dimensional transient multiphase multi-component CFD model has been established. The calculation time is more than 20 seconds real time, the coughing time is one second, the gas phase has two components air and water vapor, while the discrete phase is the aerosol liquid, which is carefully modeled by defining its components, size distribution, evaporative or non-evaporative to match the real situation.

With the current developed CFD model, the transport and fate of aerosols can be determined. The amount of aerosol inhaled by different person, the contamination of aerosol to wall/floor/ceiling as well as the remaining aerosol travel into A/C system can be obtained. This Chapter also provides a derivation of droplet evaporation model for the aerosol transport with evaporation. Besides, a latent heat model is proposed to bring on the issue of latent heat partition for the evaporation. Overall, this Chapter provide a conclusive numerical simulation approach to study the aerosol transport under air-conditioned chamber environment.

6.2 Setup of CFD Model

6.2.1 CFD Modeling of Aerosol Transport between Two Head-on Persons

Table 6.1 CFD Model Details for Aerosol Transport Between Two Head-on Persons

CFD model selection	
Steady/Unsteady	Transient
Dimension	3-D
Turbulence model	Realizable k-ε
Multi-component model	Species transport for gas phase (Air and steam)
Discrete Phase model	Saliva droplet (two different injections)
Boundary conditions	
Outlet	Pressure outlet; Escape (DPM)
Mouth1	Velocity inlet; Escape (DPM)
Mouth2	Velocity inlet (negative value); Escape (DPM)
Human dummy	Wall (Standard wall function); 300K; Trap (DPM)
Wall/ceiling	Wall (Standard wall); 293K; Trap (DPM)
Initial conditions	
Temperature	298 K
H_2O mass fraction	0.012
Major governing equations	
Continuity	$\frac{\partial}{\partial t}(\rho Y_i) + \nabla \cdot (\rho \mathbf{U} Y_i) = -\nabla \cdot \mathbf{J}_i$
Momentum	$\frac{\partial}{\partial t}(\rho \mathbf{U}) + \nabla \cdot (\rho \mathbf{U}\mathbf{U}) = -\nabla p + \nabla \cdot \boldsymbol{\tau}$
Energy	$\frac{\partial}{\partial t}(\rho E) + \nabla \cdot [\mathbf{U}(\rho E + p)] = \nabla \cdot \left[k \nabla T - \sum_i h_i \mathbf{J}_i + (\boldsymbol{\tau} \cdot \mathbf{U}) \right]$
Species conservation	$\sum Y_i = 1$
Diffusion flux	$\mathbf{J}_i = -\rho D_{i,m} \nabla Y_i$
Turbulence k	$\frac{\partial}{\partial t}(\rho k) + \nabla \cdot (\rho k \mathbf{U}) = \nabla \cdot \left[\left(\mu + \frac{\mu_t}{\sigma_k} \right) \nabla k \right] + G_k + G_b - \rho \varepsilon - Y_M$
Turbulence ε	$\frac{\partial}{\partial t}(\rho \varepsilon) + \nabla \cdot (\rho \varepsilon \mathbf{U}) = \nabla \cdot \left[\left(\mu + \frac{\mu_t}{\sigma_k} \right) \nabla \varepsilon \right] + C_{1\varepsilon} \frac{\varepsilon}{k} (G_k + C_{3\varepsilon} G_b) - C_{2\varepsilon} \rho \frac{\varepsilon^2}{k}$

This study is coupled with the experiment measurement of the breath simulator. It's simulating two persons sitting facing each other, one coughing and the other just breathing in the air around. The chamber is 2.5x4x6 m^3. The distance between two persons is similar as experiment measurement (1.7 m). The mouth is a circle with diameter of 0.0254 m. The CFD model is three dimensional, transient, turbulent, multicomponent for gas phase, multicomponent for discrete phase model (DPM, liquid injection of saliva droplet/aerosol). The details of CFD model setup/selection are shown in Table 6.1 and Table 6.2.

Table 6.2 Details of the DPM of Saliva

Saliva droplet	
Components	Water, Sodium Chloride and Glycerin
Material properties of glycerin	Density: 1261 kg/m^3 Specific heat: 2430 j/kg-K
Details of DPM	
Drag law	Spherical
Injection1 (fine droplets)	Particle type: multicomponent Particle size:,5 μm (uniform) Injection type: from surface (mouth1) Injection velocity: 10 m/s Mass flowrate: 5 mg/s Turbulent dispersion: discrete random walk model Evaporative component: H_2O
Injection2 (coarse droplets)	Particle type: multicomponent Particle size:, Rosin-Rammlar distribution: 77 μm min, 737 μm max, 17 μm mean, number of group particle: 8μm Injection type: from surface (mouth1) Injection velocity: 4.2 m/s Mass flowrate: 5 mg/s Turbulent dispersion: discrete random walk model Evaporative component: H_2O
Discrete Phase model	Saliva droplet (two different injections)

The details of geometry for this CFD model and mesh generation can be referred in Figure 6.1 and Figure 6.2. The total number of mesh is 228,000. The coughing is lasting for 1 second, after that the turbulence model is switched from Realizable k- ε to Standard k-ε. The breathing is set as flowrate-equivalent constant velocity (0.45 m/s) based on literature data (Gupta *et al*. 2009a).

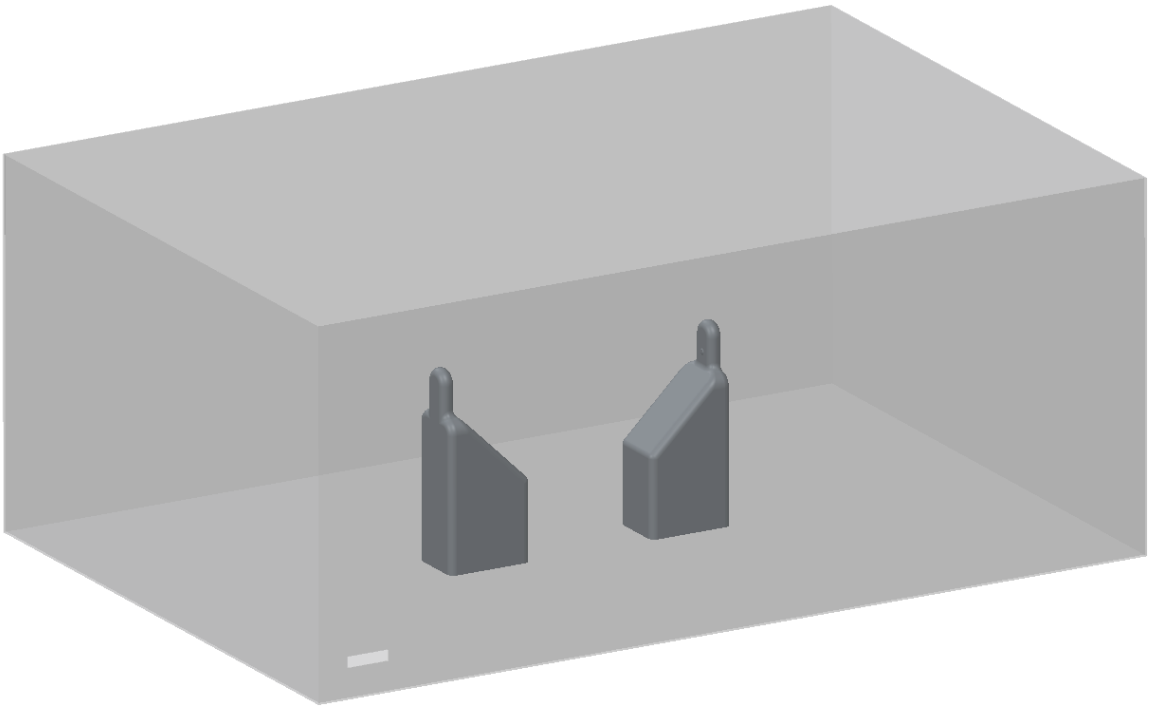

Figure 6.1 Geometry of numerical simulation.

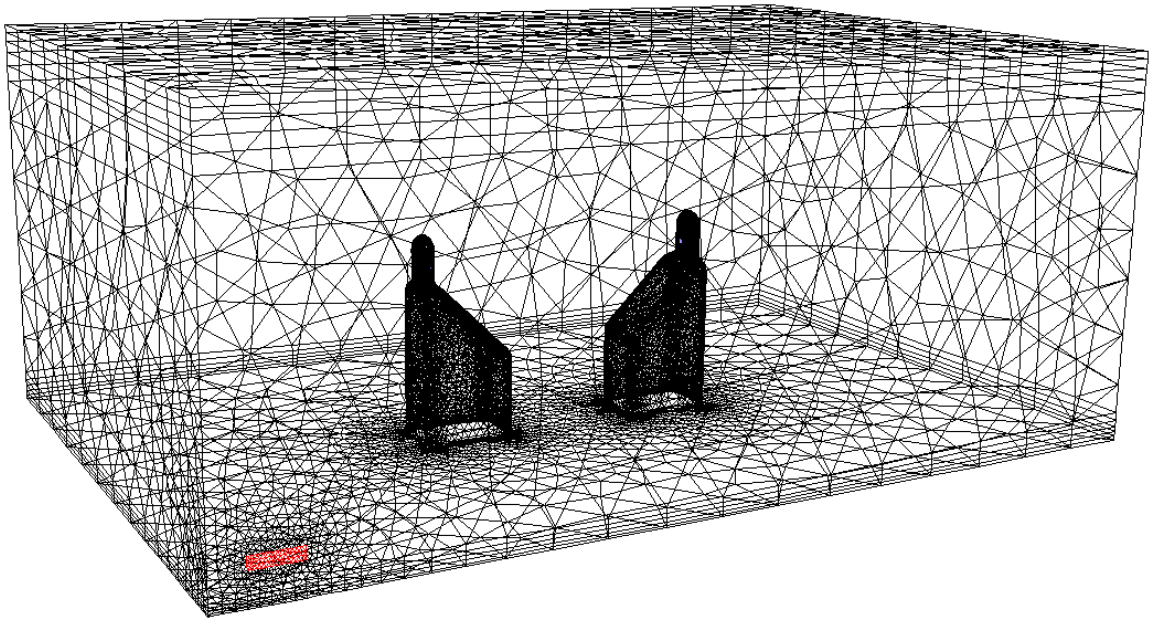

Figure 6.2 Mesh of numerical simulation.

6.2.2 CFD Modeling of Aerosol Transport inside the Air-Conditioned Chamber

This study is coupled with the experiment measurement of aerosol transport in the air-conditioned chamber. One person coughs for one second and the other on just breathing in the air. The chamber is 7x8x10 ft^3. The geometry is built exactly based on the experiment, and the total cell number is around 500,000. The distance between two persons is similar as experiment measurement (1 m). The mouth is a circle with diameter of 0.0254 m. The CFD model is three dimensional, transient, turbulent, multicomponent for gas phase, multicomponent for discrete phase model (DPM, liquid injection of saliva droplet). Geometry and mesh are shown in the Figures 6.3 and 6.4. This model has three inlets and three outlets on the chamber wall and four human mouths as inhaling/ exhaling source. Major governing equations, model setup, and boundary conditions are listed in Table 6.3:

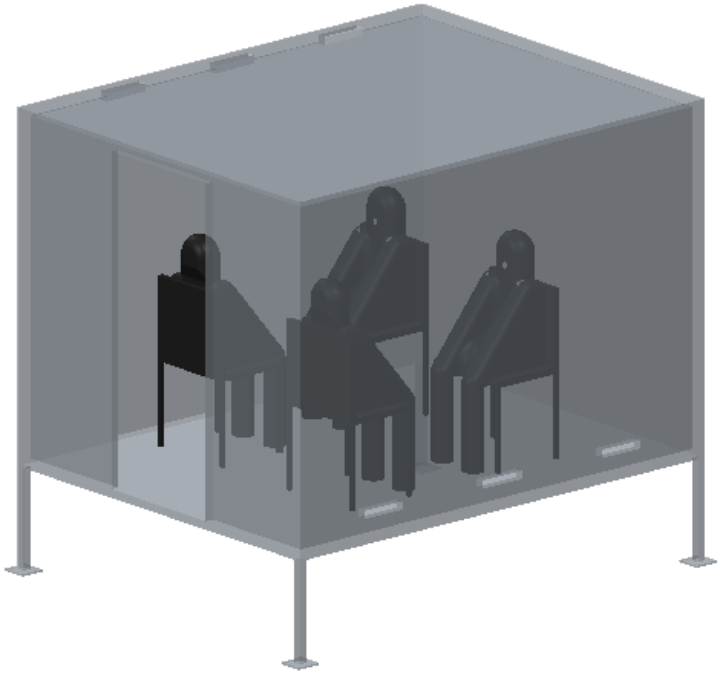

Figure 6.3 Geometry of numerical simulation.

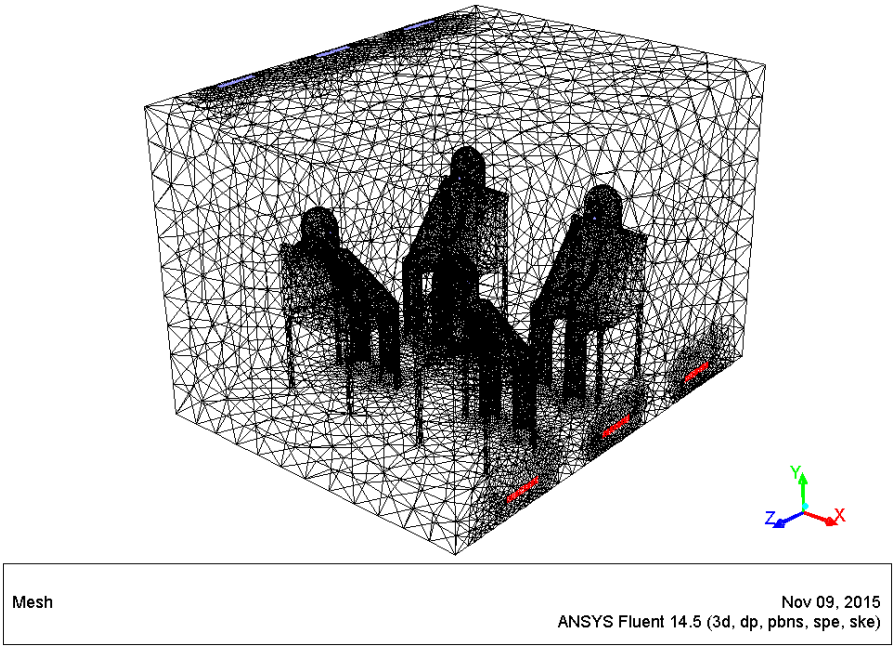

Figure 6.4 Mesh of numerical simulation.

Table 6.3 CFD Model Details for Aerosol Transport in the A/C Chamber

CFD model selection	
Steady/Unsteady	Steady
Dimension	3-D
Turbulence model	Standard k-ε
Multi-component model	Species transport
Discrete Phase model	Droplet
Boundary conditions	
Inlet	Velocity inlet
Outlet	Pressure outlet
Mouth	Velocity inlet
Wall	Wall (Standard wall function); Trap (for DPM)
Initial conditions	
Temperature	298 K
H_2O mass fraction	0.012
Major governing equations	
Continuity	$\frac{\partial}{\partial t}(\rho Y_i) + \nabla \cdot (\rho \mathbf{U} Y_i) = -\nabla \cdot \mathbf{J}_i$
Momentum	$\frac{\partial}{\partial t}(\rho \mathbf{U}) + \nabla \cdot (\rho \mathbf{U}\mathbf{U}) = -\nabla p + \nabla \cdot \boldsymbol{\tau}$
Energy	$\frac{\partial}{\partial t}(\rho E) + \nabla \cdot \left[\mathbf{U}(\rho E + p)\right] = \nabla \cdot \left[k \nabla T - \sum_i h_i \mathbf{J}_i + (\boldsymbol{\tau} \cdot \mathbf{U})\right]$
Species conservation	$\sum Y_i = 1$
Diffusion flux	$\mathbf{J}_i = -\rho D_{i,m} \nabla Y_i$
Turbulence k	$\frac{\partial}{\partial t}(\rho k) + \nabla \cdot (\rho k \mathbf{U}) = \nabla \cdot \left[\left(\mu + \frac{\mu_t}{\sigma_k}\right)\nabla k\right] + G_k + G_b - \rho\varepsilon - Y_M$
Turbulence ε	$\frac{\partial}{\partial t}(\rho \varepsilon) + \nabla \cdot (\rho \varepsilon \mathbf{U}) = \nabla \cdot \left[\left(\mu + \frac{\mu_t}{\sigma_k}\right)\nabla \varepsilon\right] + C_{1\varepsilon}\frac{\varepsilon}{k}(G_k + C_{3\varepsilon} G_b) - C_{2\varepsilon}\rho\frac{\varepsilon^2}{k}$

6.3 Droplet Evaporation and Heat Transfer Model

The droplet evaporation also plays a very important role in the aerosol transport. First, the size of droplet affects its trajectory. As the droplet evaporates, the size keeps shrinking. And secondly, the water content of droplet maybe critical for the carrying pathogen vitality and mortality. The existed droplet evaporation mostly deals with single component diffusion controlled evaporation. Based on our best knowledge, the

convection effect is rarely considered and also the latent heat partition on droplet and adjacent gas phase has never been studied. The convection should not be totally ignored without justification, since in this study the droplets evaporating in an air circulating environment. The latent heat study is important here because it may greatly affect the droplet temperature, which dictates the saturation pressure of water vapor at its interface.

The multi-component, diffusion controlled and convection assisted droplet evaporation model is based on traditional d^2 model. Using boundary layer analysis, the diffusion boundary layer is introduced as a convection factor. The latent heat partition has been discussed and analyzed. This evaporation model will be implemented to the CFD model via User-Defined Function.

6.3.1 Derivation of Droplet Evaporation

The d^2-law model of droplet vaporization (Goldsmith, 1955; Sirignano, 1999) is among the simplest and the most popular, which considers the evaporation of a saturated spherical droplet by pure diffusion in a quiescent gas environment. The classical d^2-law can be directly applied to estimate the evaporation for moving droplets with very small relative *Re* number (around or less than 1), such as the case of fine droplets (1-10 μm) in this study. However, the aforementioned assumptions of quiescent gas environment and pure diffusion are not adequate for the higher *Re* number scenario, such as the case of the coarse droplets (100–700 μm with corresponding *Re* number around 10-50) in this study. Hence, a modified d^2-law has been used to include the convection effect (Sirignano, 1999):

$$\frac{dm}{dt} = 4\pi D\rho R_D \left(1 + \frac{\mathrm{Re}\,\mathrm{Sc}}{2}\right) \ln\left(1 + \frac{Y_{R_D} - Y_\infty}{1 - Y_{R_D}}\right) \tag{6.1}$$

where D, Y, R_D, Re and Sc represent the mass diffusivity, mass fraction of water vapor in the gas mixture, droplet radius, droplet Reynolds number, and Schmidt number, respectively. It should be noted that Y_{RD} depends on the droplet temperature and Re depends on both droplet velocity and ambient gas flow velocity. In this study, the ambient gas flow is acquired by a CFD simulation with the coupling effect of droplet vaporization. The droplet transport is modeled by a Lagrangian approach, with coupled momentum and energy equations of droplet.

The droplet momentum equation can be expressed by:

$$m\frac{d\vec{u}_d}{dt} = \frac{\pi}{8} C_D d^2 \rho \left(\vec{u}_g - \vec{u}_d\right)\left|\vec{u}_g - \vec{u}_d\right| + \vec{g} - \vec{u}_d \frac{dm}{dt} \tag{6.2}$$

where C_D is a function of Re (Mandø and Rosendahl, 2010):

$$C_D = \begin{cases} \dfrac{16}{\mathrm{Re}}\left\{1 + \left[\dfrac{8}{\mathrm{Re}} + \dfrac{1}{2}\left(1 + \dfrac{3.315}{\sqrt{\mathrm{Re}}}\right)\right]\right\} & 100 > \mathrm{Re} > 1 \\ \dfrac{48}{\mathrm{Re}}\left(1 - \dfrac{2.21}{\sqrt{\mathrm{Re}}}\right) & 100 < \mathrm{Re} \end{cases} \tag{6.3}$$

The energy equation of droplet, with the effects of heat convection and droplet evaporation, can be expressed by:

$$c_p m \frac{dT_d}{dt} = \pi d^2 h\left(T_g - T_d\right) + L\frac{dm}{dt} \tag{6.4}$$

where the convective heat transfer coefficient h is estimated using a simple heat transfer correlation of a non-evaporative sphere (Incropera and DeWitt, 2011):

$$h = \frac{k}{d}\left(2 + 0.6 * \mathrm{Re}^{\frac{1}{2}} \mathrm{Pr}^{\frac{1}{3}}\right) \tag{6.5}$$

Hence, the droplet mass, velocity and temperature can be solved by the coupled equations (6.1), (6.2), (6.4), with the ambient gas velocity and humidity calculated via the CFD simulation.

6.3.2 Derivation of Latent Heat Partition

Assume there is a two-phase single component environment, as shown below. This two-phase environment has a gas-liquid interface, there are heating net and heating plate maintained at constant temperature to provide necessary heat for the steady state evaporation, which forms a Stefan flux towards the heating net direction. Due to the evaporation at the interface, the temperature there should be the lowest. The interface temperature for both liquid and gas phases are the same T_I.

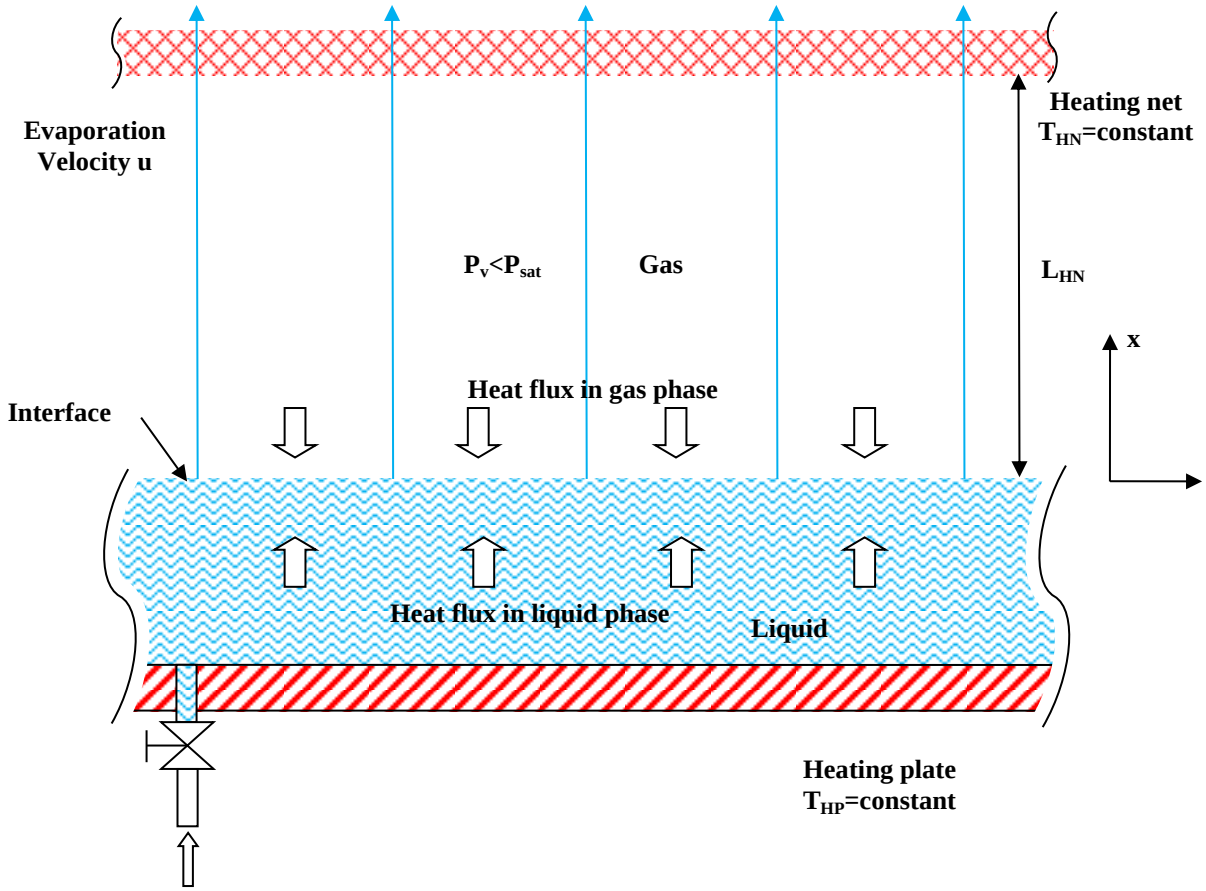

Figure 6.5 Problem description of latent heat model.

To find out the how the latent heat contributing to each phase, it is starting from the energy equation of a laminar flow for the gas phase:

$$\frac{\partial}{\partial t}\left(\rho c_v T_g\right)+\nabla\cdot\left(\rho\vec{u}c_v T_g\right)=-p\left(\nabla\cdot\vec{u}\right)+\nabla k\cdot\nabla T_g+\nabla:S+J_e \qquad (6.20)$$

For steady, one dimensional, no energy source or sink, also ignoring dissipation, we have:

$$\frac{d}{dx}\left(\rho u c_v T_g\right) = k\frac{d^2}{dx^2}T_g \tag{6.21}$$

where, the u represents the velocity of Stefan flux, which is a constant as the evaporation rate is a fixed value for this steady state condition. Hence, it can be changed to:

$$\frac{\rho u c_v}{k}\frac{dT_g}{dx} = \frac{d^2T_g}{dx^2} \tag{6.22}$$

Define:

$$\frac{\rho u c_v}{k} \equiv A \tag{6.23}$$

Then:

$$A\frac{dT_g}{dx} = \frac{d^2T_g}{dx^2} \tag{6.24}$$

And:

$$\frac{dT_g}{dx}\left(AT_g - \frac{dT_g}{dx}\right) = 0 \tag{6.25}$$

Integrate over x:

$$AT_g - \frac{dT_g}{dx} = C_1 \tag{6.26}$$

Rearrange to:

$$\frac{dT_g}{dx} = AT_g - C_1 \tag{6.27}$$

And:

$$\frac{dT_g}{AT - C_1} = dx \tag{6.28}$$

Then:

$$\frac{d\left(AT_g - C_1\right)}{AT_g - C_1} = Adx \tag{6.29}$$

Integrate again:

$$\ln\left(AT_g - C_1\right) = Ax + \ln C_2 \tag{6.30}$$

Rearrange to:

$$e^{Ax} = \frac{AT_g - C_1}{C_2} \tag{6.31}$$

Thus, the temperature of gas phase can be represented as:

$$T_g = \frac{1}{A}\left(C_2 e^{Ax} + C_1\right) \tag{6.32}$$

The coefficients C1 and C2 can be determined based on the boundary conditions:

$$\begin{cases} x = 0, T_g = T \\ x = L_{HN}, T_g = T_{HN} \end{cases} \tag{6.33}$$

$$\Rightarrow \begin{cases} C_1 = A\left(T_I - \dfrac{T_{HN} - T_I}{e^{AL_{HN}} - 1}\right) \\ C_2 = \dfrac{A\left(T_{HN} - T_I\right)}{e^{AL_{HN}} - 1} \end{cases} \tag{6.34}$$

Thus, the temperature of gas phase can be expressed as:

$$T_g = T_I + \left(T_{HN} - T_I\right)\frac{e^{Ax} - 1}{e^{AL_{HN}} - 1} \tag{6.35}$$

Then the heat flux in gas phase is:

$$Q_g = k_g \frac{dT_g}{dx} = k_g \frac{A\left(T_{HN} - T_I\right)}{e^{AL_{HN}} - 1} e^{Ax} \tag{6.36}$$

For liquid phase, it is assumed no motion for liquid, thus

$$Q_l = k_l \frac{dT_l}{dx} = k_l \frac{T_{HP} - T_I}{L_{HP}} \tag{6.37}$$

The ratio is:

$$\frac{Q_g}{Q_l} = \frac{k_g \frac{A\left(T_{HN} - T_I\right)}{e^{AL_{HN}} - 1} e^{Ax}}{k_l \frac{T_{HP} - T_I}{L_{HP}}} \tag{6.38}$$

And the sum equals to the latent heat multiply the evaporation rate:

$$Q_g + Q_l = \dot{m}L \tag{6.39}$$

The fundamental of droplet evaporation model has been established. Next step will be include the multicomponent factor into the evaporation model and further explore the potential of the latent heat partition model. Equations 6.35 and 6.38 can also be expressed as:

$$T_g = T_I + \left(T_{HN} - T_I\right)\frac{e^{Pe\frac{x}{L_{HN}}} - 1}{e^{Pe} - 1} \tag{6.40}$$

$$Q^* = k^* PeT^* \frac{e^{Pe\frac{x}{L_{HN}}}}{e^{Pe} - 1} \tag{6.41}$$

where *Pe* is the Peclet number. The calculated temperature profile and latent heat partition are shown in the following figures:

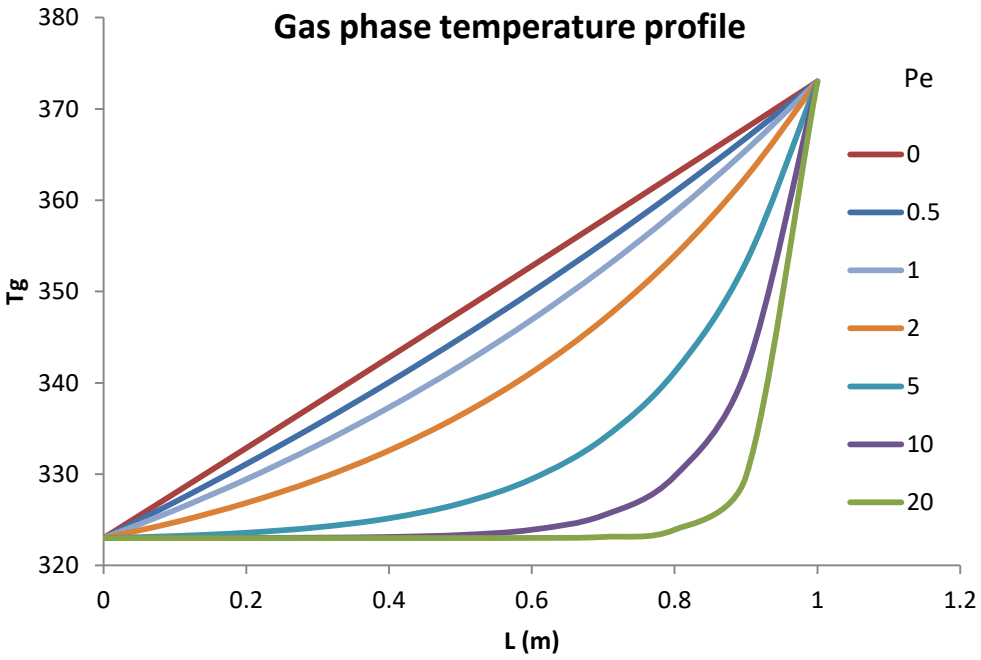

Figure 6.5a Gas phase temperature profile along L.

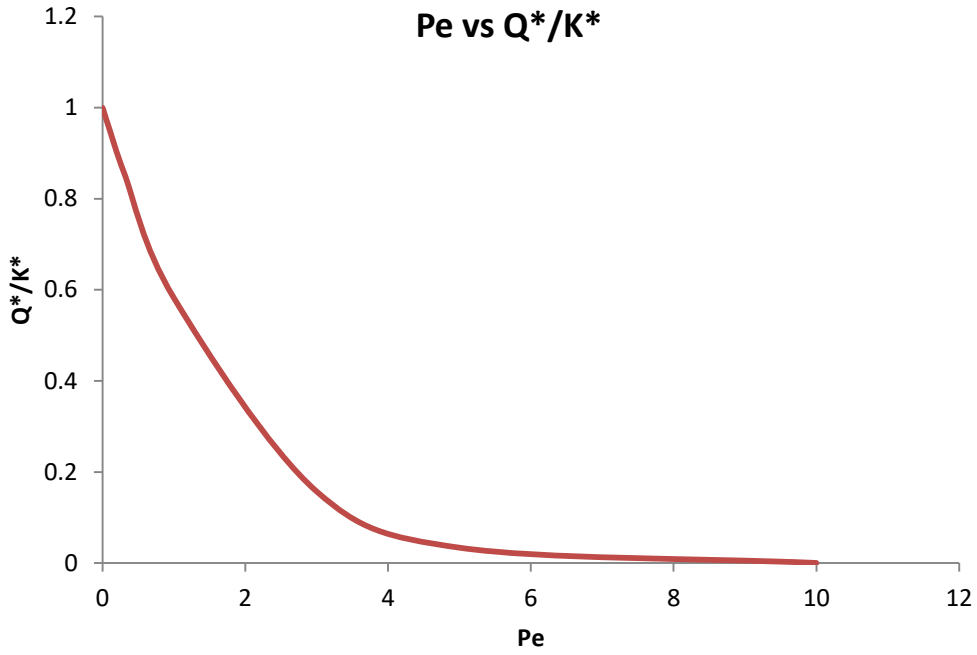

Figure 6.5b Latent heat partition of Q*/K* vs Peclet number.

Figure 6.5a Shows for very low Pe number, the temperature profile for gas phase is very close to the one for pure conduction with same temperature range. At height Pe number (more intense evaporation) condition, the temperature profile tend to turn to a curve instead of a linear line. The extreme case is the temperature profile will become a combination of two linear lines as the one of Pe=20.

6.4 Results and Discussion of the CFD Model

6.4.1 Results of CFD Simulation of Aerosol Transport for Two Head-on Persons

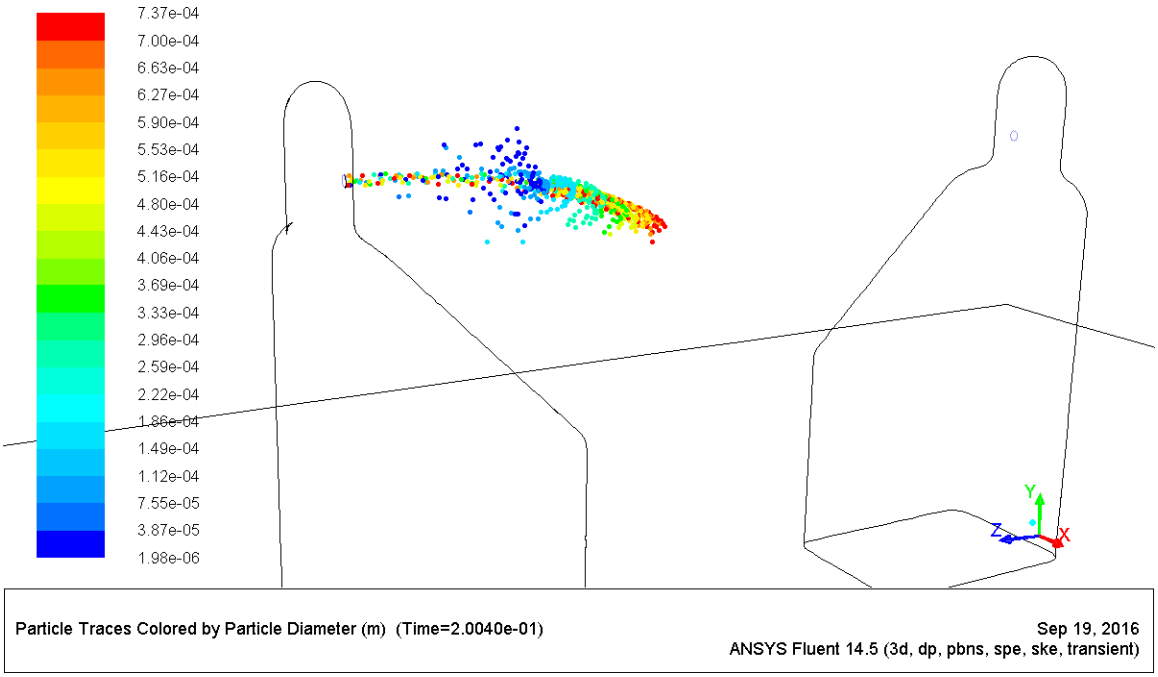

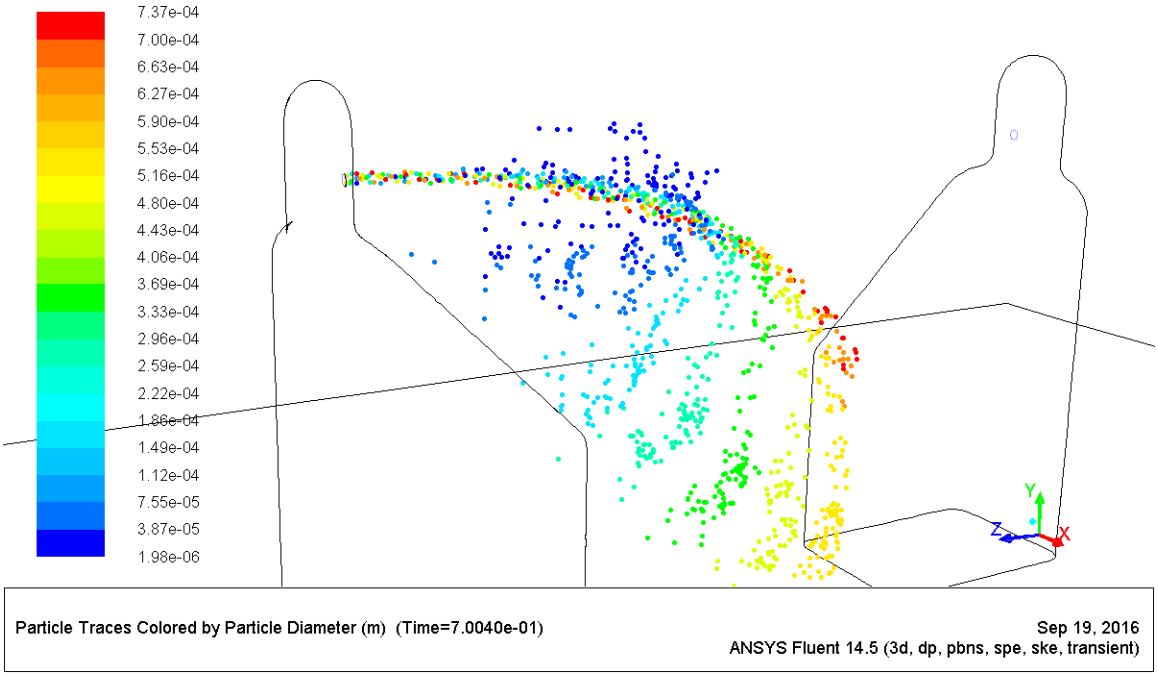

Figure 6.6 Coughing saliva transport at 0.2 s (top) and 0.7 s (bottom).

Figure 6.6 shows that the largest coarse (the red ones) droplets arrive to the other person within 0.6 second, while the smaller ones and fine droplets (aerosol) are still in the air.

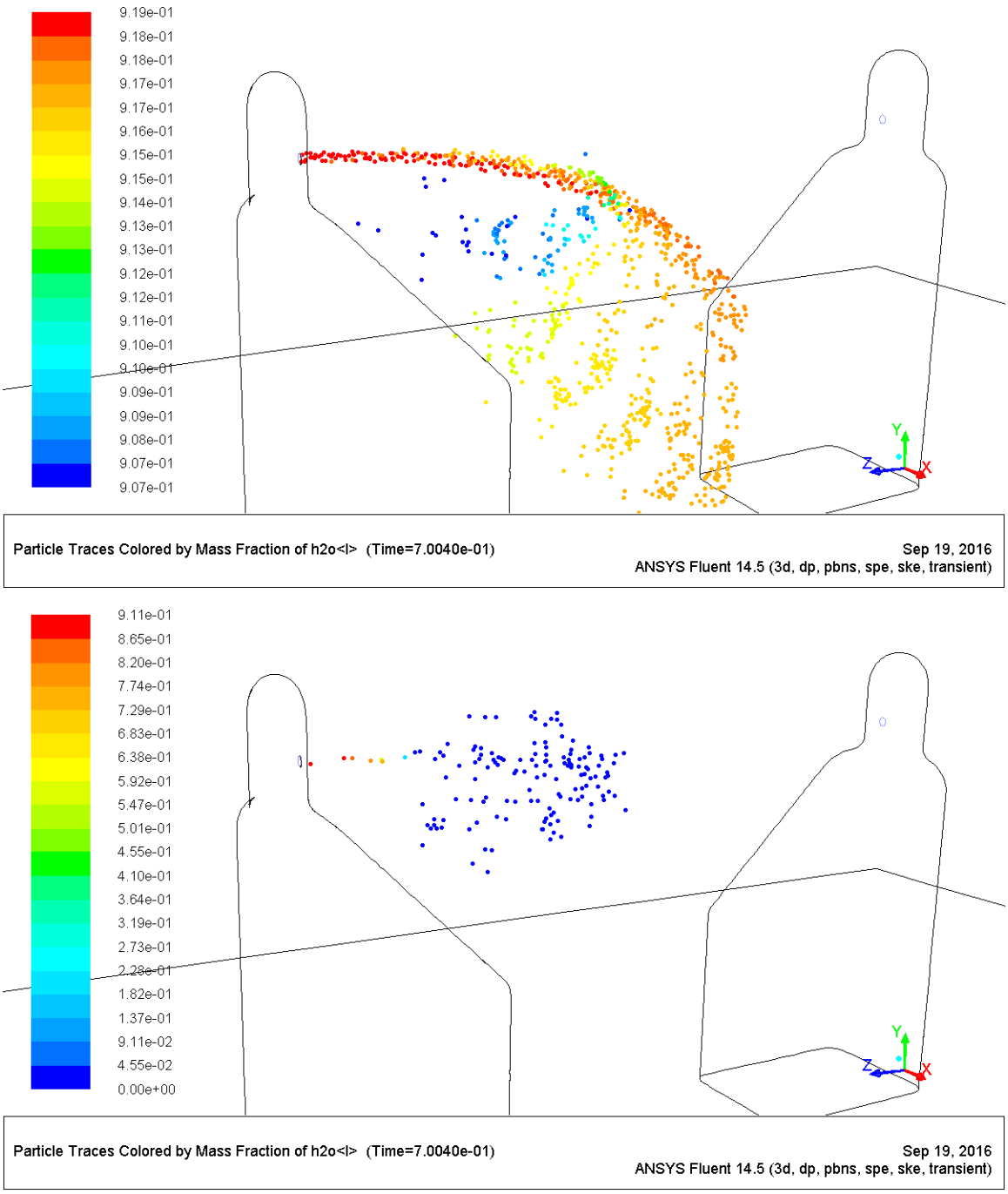

Figure 6.7 H_2O fraction at 0.7 s for coarse (top) and fine (bottom) Droplets.

Figure 6.7 shows the evaporation for both coarse and fine droplets at 0.7 second. Obviously, fine droplets evaporate almost instantaneously, while most coarse droplets remain very “wet”.

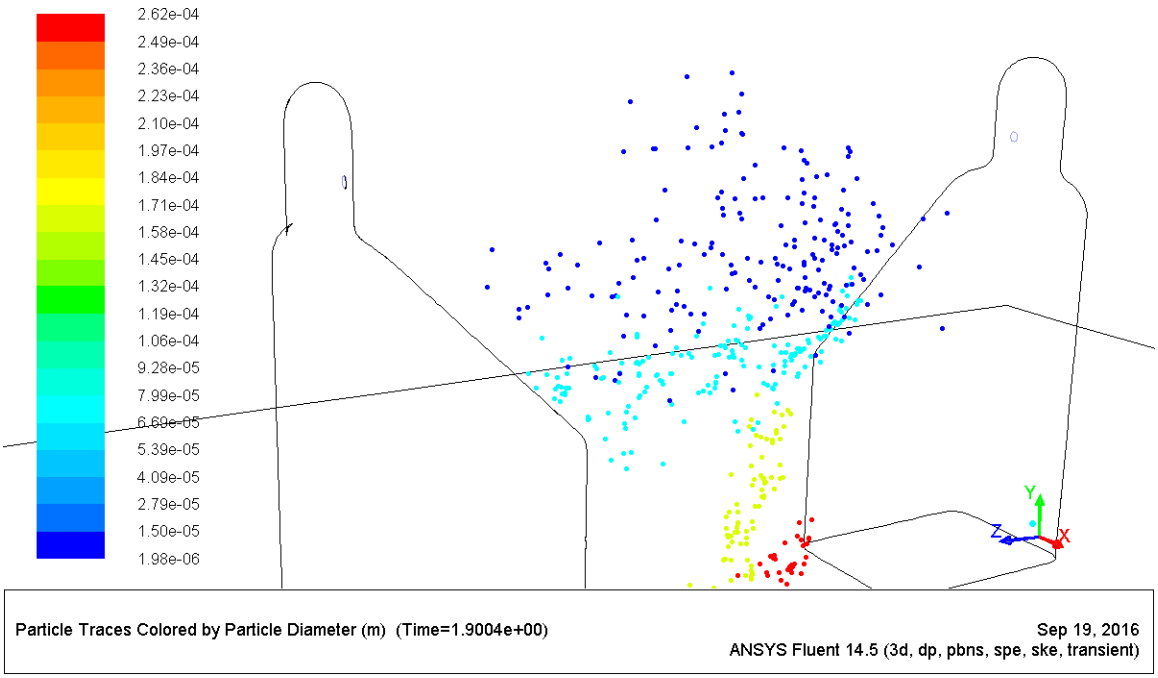

Figure 6.8 Droplets Size at 1.9 s.

Figure 6.8 shows at about 2 seconds (1.9 s), most coarse droplets have landed on the surface of human dummy or the floor. Meanwhile, most fine droplets are still in the air.

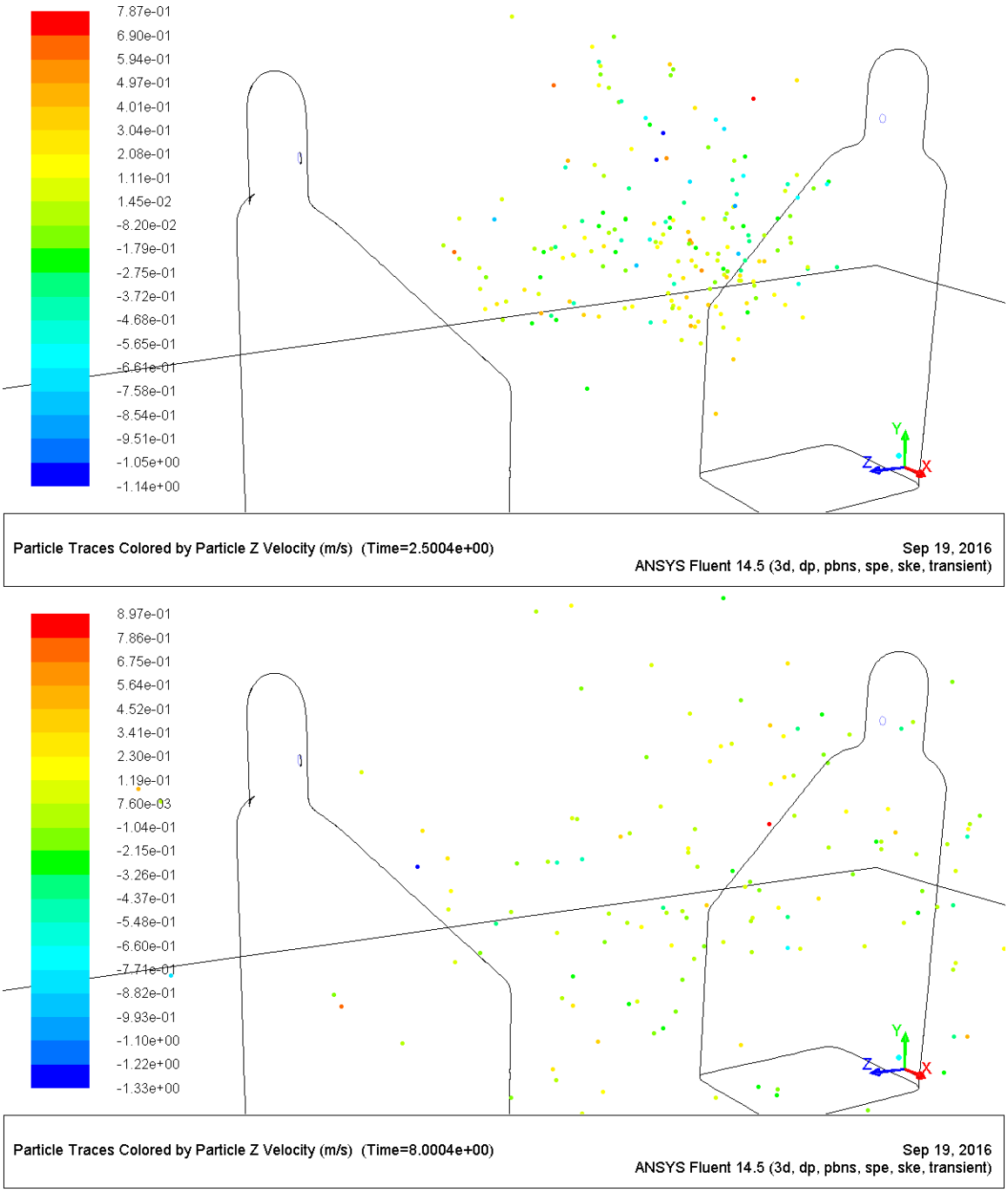

Figure 6.9 Fine Droplets (Aerosol) Transport at 2.5 s (top) and 8 s (bottom).

Figure 6.9 shows the aerosol transport from 2.5 second to 8 second. The color indicates the value of z-direction velocity for individual droplet. At 8 second after the

coughing, fine droplets have spread out by combined effect of convection and diffusion. Also, at this moment, a significant amount of aerosol has travelled to the mouth of the other person, which indicates the breathing in of aerosol.

Up to 20 seconds, the simulation is considered long enough, and the fate of all droplets is considered the final fate. A summary of the all droplets information at 20 seconds is listed in Table 6.4 with the comparison of the experiment measurement in Chapter 3.

Table 6.4 Fate for Aerosol Transport of CFD Simulation with Comparison of Experiment

Time (s)	% Breath in	% floor	% person 2	% person 1	% Ceiling	Experiment data
2.5	0	55.2	43.7	1.1	0	-
3.7	<0.01	55.5	43	1.2	0	-
5	0.02	55.1	43.6	1.3	0	-
10	0.05	54.5	43.9	1.6	0	-
20	0.09	52.8	43.8	3.3	<0.02	0.22

Considering the randomness of human coughing, the comparison between experiment data and CFD result at 20 seconds shows reasonable agreement. The calculation would come to better agreement with experiment data for longer calculation time (more than 20 seconds). Effectively and computational affordably, 20 seconds is the time for this simulation. Another reason is in the real experiment lab, though the size is similar as the CFD model, there are much more surfaces such as of tables and shelves to trap aerosol, which may reduce the accuracy for the CFD simulation if the calculation is long enough. Table 6.4 also shows the breathing in aerosol starts at 3.7 seconds after the

coughing. And the amount of coughing aerosol falling on the floor is more than on the person at the distance of 1.7 m. There is relatively tiny amount of aerosol ends up back to the coughing person. At 20s, a negligible amount of aerosol reaches to the ceiling.

6.4.2 Results of CFD Simulation for Aerosol Transport Inside the Air-conditioned Chamber

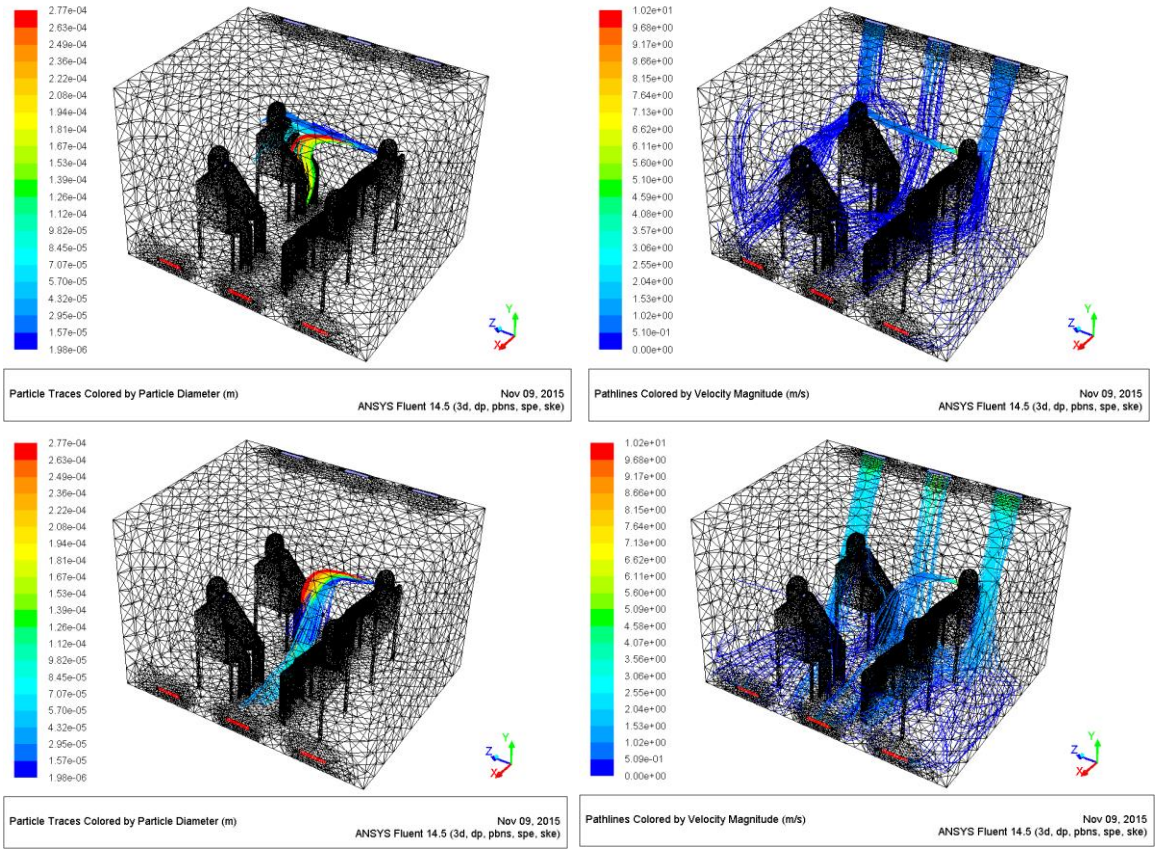

Figure 6.10 A steady state simulation of fine droplets trajectory and pathline under 15 ACH (top) and 60 ACH (bottom).

Based on the CFD setting aforementioned for the chamber aerosol transport, a steady state simulation has been conducted for a fast analysis of the effect for different ACH on aerosol transport and flow pattern in the chamber. The results show significant difference of droplets trajectory between different circulation rates. Higher ACH plays a huge

impact on the aerosol transport, while lower ACH may result a better circulation pattern in the chamber.

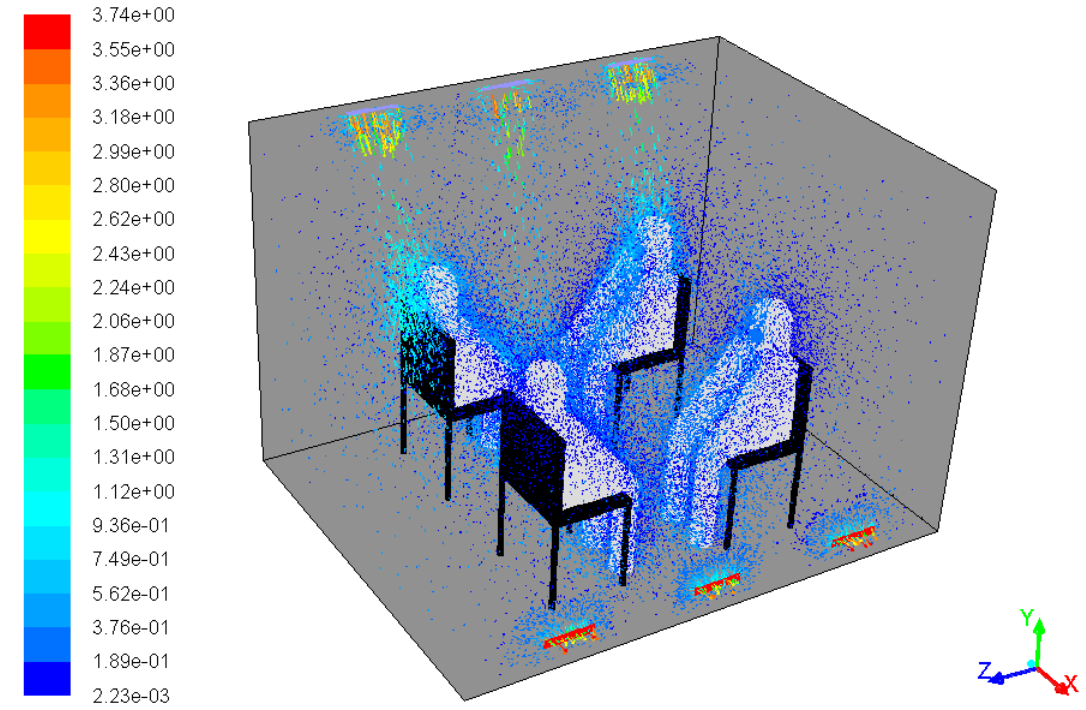

Figure 6.11 Initial condition for the CFD study of chamber aerosol transport.

The initial condition is using the simulation result for steady state without coughing injections, as shown in Figure 6.11.

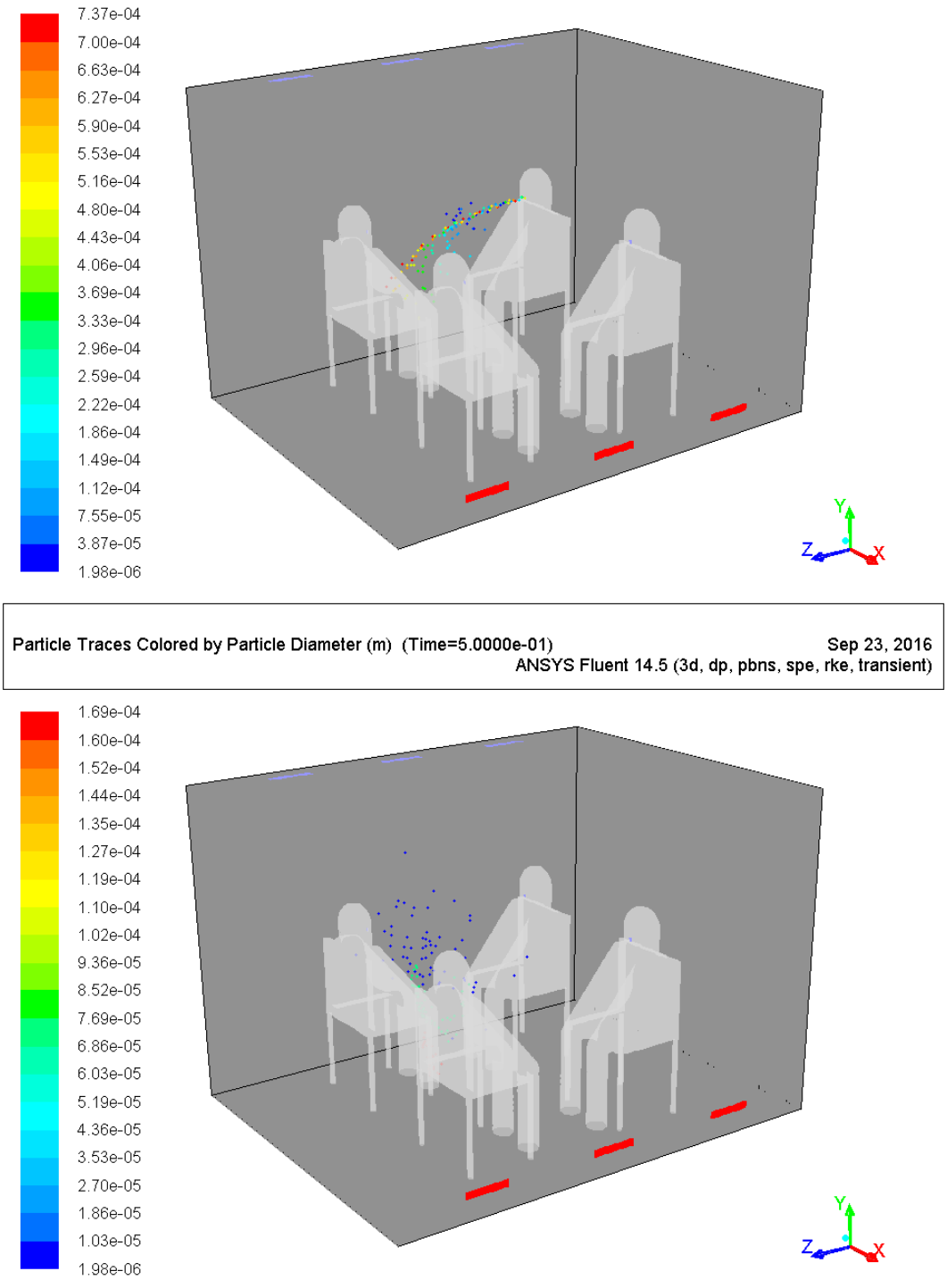

Figure 6.12 Results of CFD simulation for chamber aerosol transport at 0.5s (top) and 2s (bottom).

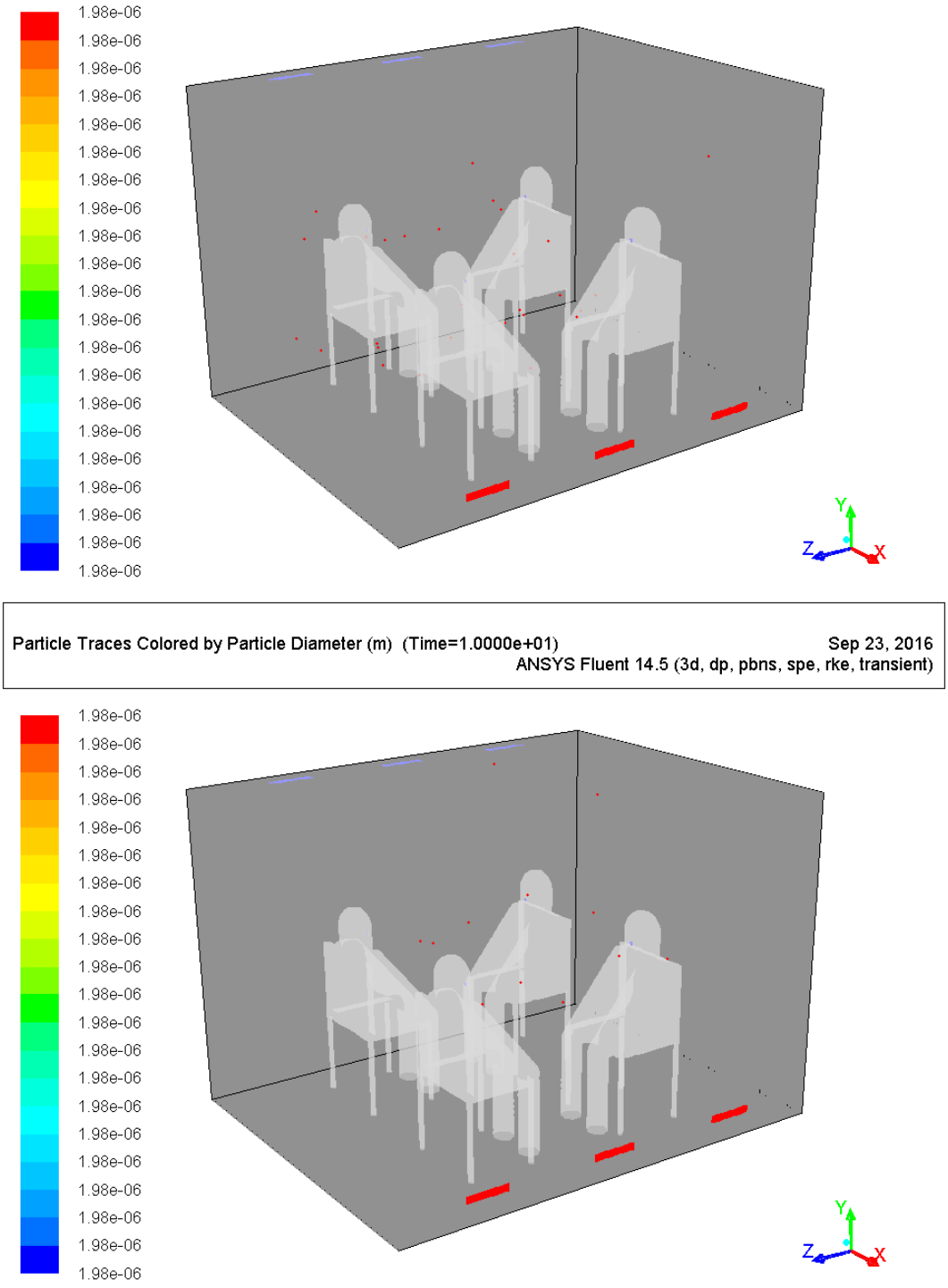

Figure 6.13 Results of CFD simulation for chamber aerosol transport at 10s (top) and 20s (bottom).

The results of CFD simulation for chamber aerosol transport are shown from Figure 6.12 and Figure 6.15.

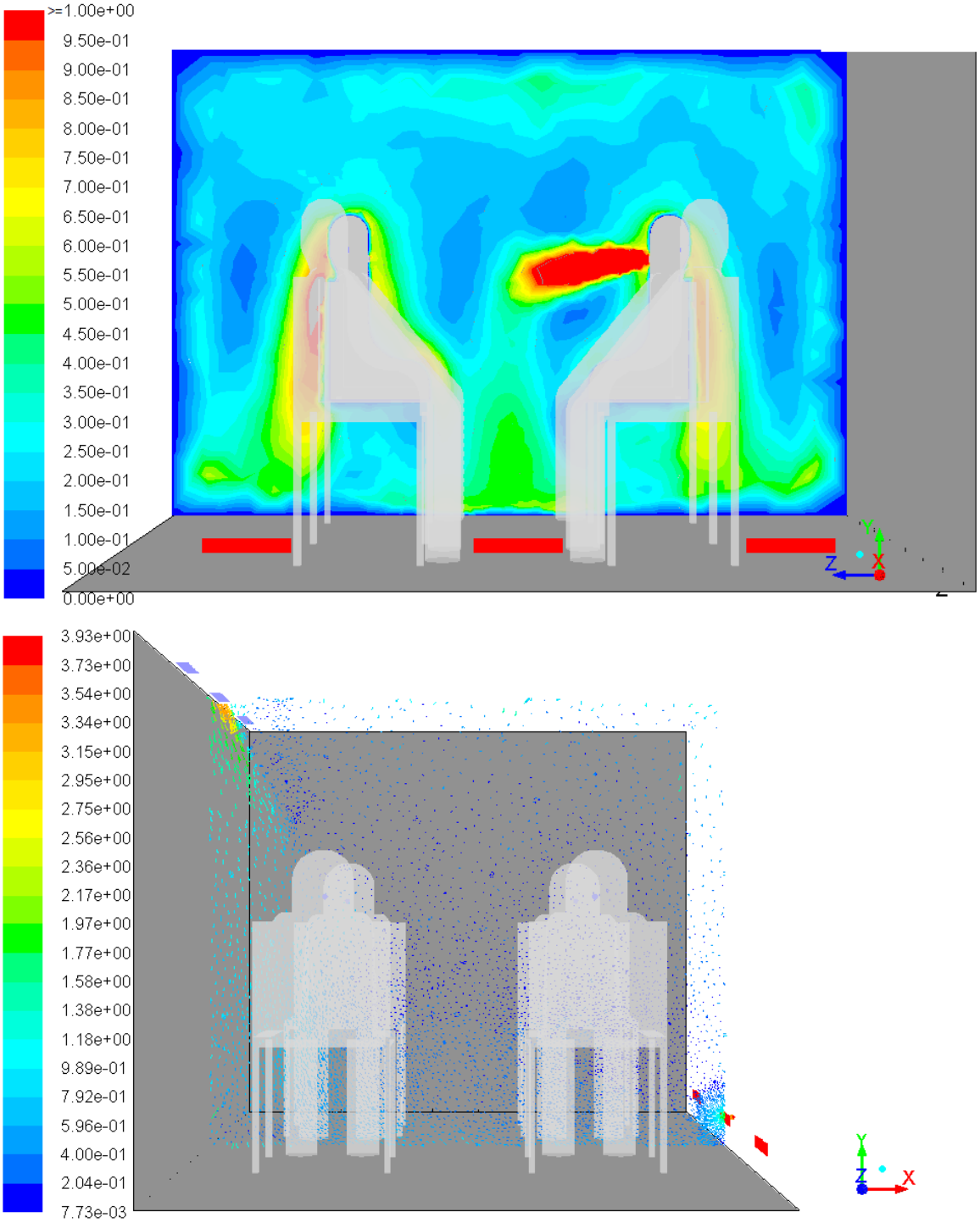

Figure 6.14 Results of CFD simulation for mean flow velocity at 0.5s.

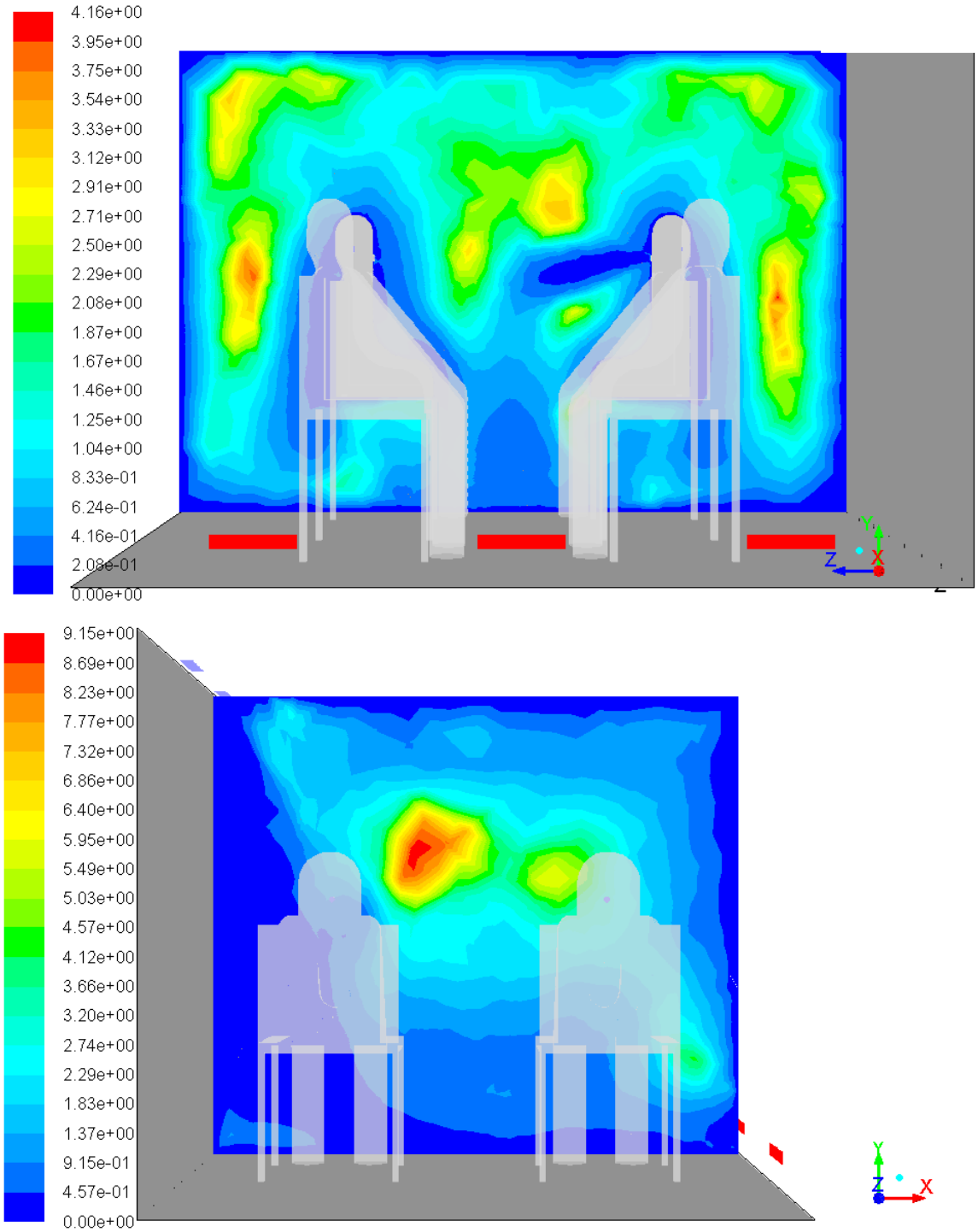

Figure 6.15 Results of CFD simulation for turbulence intensity at 0.5s.

Results show that under the coughing and air circulation conditions, the inhaling does not have much effect on the whole flow field. For the turbulence, carefully selection of the turbulence model is suggested.

The aerosol destiny of this CFD simulation is summarized in the following Figure 6.16 and Figure 6.17. The results show that majority of aerosol landed on the surfaces of floor/wall/ceiling/human, while some portion of aerosol is inhaled into human body. Very little of total aerosol further emits into A/C system.

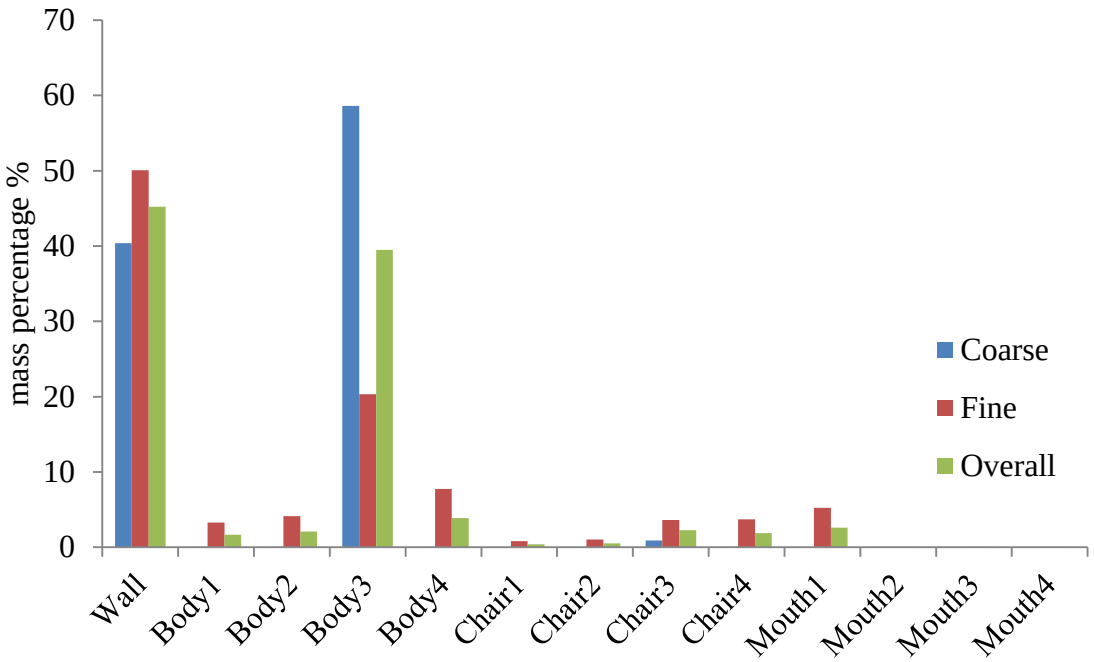

Figure 6.16 Results of CFD simulation for aerosol destiny at 20s.

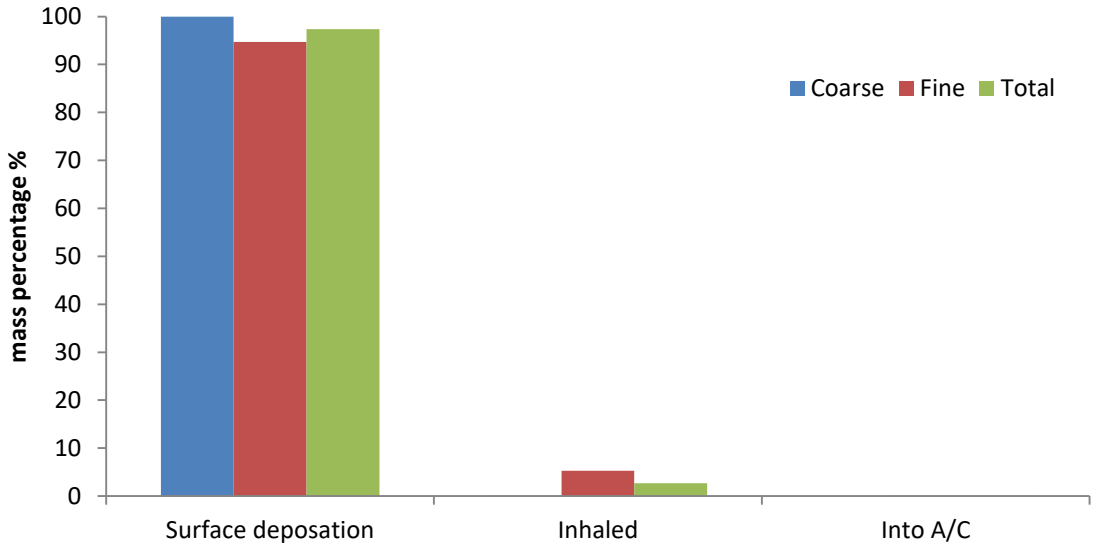

Figure 6.17 Results of CFD simulation for aerosol destiny at 20s as a summary.

6.5 Concluding Remark

In this chapter, the followings have been achieved: 1) A CFD simulation framework of predicting aerosol transport for indoor environment has been established. This simulation is three dimensional with weak turbulent and low temperature difference buoyance. The aerosol is multi-components, evaporative with nuclei. 2) Compared with experiment data and validated by experiment study. 3) More complicated and realistic evaporation model and latent heat partition model have been derived.

CHAPTER 7

CONCLUSION SUMMARY AND FUTURE STUDY

7.1 Dissertation Conclusion

This dissertation aims to establish a planform of studying the aerosol transport caused by coughing in a depressurized and air-conditioned environment. To reach this goal, the novel cough simulator is designed and produced with calibration of its characteristics; a breath simulator to collect the aerosol generated by the cough simulator has also been designed and produced. Both simulators have been designed and produced by 3-D printing. During the exploration of these two simulators, new experiment measurement methods have been proposed and verified. The CFD simulation for the full field chamber is also established. The droplet evaporation model is formed and the latent heat partition model shows some preliminary derivation results. To validate the CFD simulation, the experiment air-conditioned chamber has been built. The chamber has proper size and a controllable range of temperature and air circulation rate. To implement the sub-atmospheric pressure effect, an open flow depressurization system has been built. This system uses steam condensation to generate vacuum and is scale-up friendly. The depressurization system and the cough simulator have logical control systems to maintain and regulate the continuous operation. The bimodal cough simulator is the first ever to build, and the breath simulator is so too base on our best knowledge. The latent heat partition coupled multicomponent droplet evaporation model will be the first ever. The whole project will provide guidance of aerosol transport in a depressurized air-

conditioned chamber, and also provide critical input conditions for coughing-induced disease transmission model of medical, public health fields or similar.

7.2 Future Study

The future study would be including more parametric study of CFD simulation, building more sophisticated evaporation model and implement this evaporation model in the CFD simulation through User-Defined Functions. If possible, coupling more realistic latent heat partition model with the droplet evaporation model and including the depressurization effect for CFD simulation. Experimentally, combining the air-conditioned chamber with the depressurization system to realize an air-conditioned depressurized indoor environment for the study of coughing-induced aerosol transport.

BIBLIOGRAPHY

Anderson, M. H., Herranz, L. E. and Corradini, M. L. (1998) Experimental analysis of heat transfer within the AP600 containment under postulated accident conditions, Nuclear Engineering and Design, **185**(2-3): 153-172.

Beck-Broichsitter, M., Knuedeler, M. C., Seeger, W. and Schmehl, T. (2014) Controlling the droplet size of formulations nebulized by vibrating-membrane technology, European Journal of Pharmaceutics and Biopharmaceutics, **87**(3): 524-529.

Behrends, C., Fuchs, R. K. and Kaatze U. (2006) Dielectric properties of glycerol/water mixtures at temperatures between 10 and 50 °C, Jounal of Chemical Physics, **124**: 144512

Cecchini, S., Schena E., ilvestri S. (2011) An open-loop controlled active lung simulator for preterm infants, Medical Engineering and Physics, **33:** 47–55

Chambers, A. (2005). Experimental investigation on the heat transfer characteristics of vacuum spray flash evaporation cooling, International Journal of Heat and Mass Transfer, **102**(2016) 233–240

Chao, C. Wan, Y. H., Morawska, M. P. L., Johnson, G. R., Ristovski, Z. D., Hargreaves, M., Mengersen, K., Corbett, S., Li, Y., Xie, X. and Katoshevski, D. (2010) Characterization of expiration air jets and droplet size distributions immediately at the mouth opening, Journal of Aerosol Science, **40**(2): 122–133.

Chen, C. and Zhao, B. (2010) Some questions on dispersion of human exhaled droplets in ventilation room: Answers from numerical investigation, Indoor Air, **20**(2): 95-111.

Wen-Long Cheng, Yu-Hang Peng, Hua Chen, Lei Hu, Han-Ping Hu. (2016) Experimental study on optimal spray parameters of piezoelectric atomizer based spray cooling, International Journal of Heat and Mass Transfer, **103**: 57–65

Vincent C.C. Cheng, Jasper F.W. Chan, Kelvin K.W. To, K.Y. Yuen. (2013) Clinical management and infection control of SARS: Lessons learned, Antiviral Research, **100**: 407–419

Churchill, S. W. and H. H. S. Chu (1975). Correlating equations for laminar and turbulent free convection from a vertical plate, International Journal of Heat and Mass Transfer, **18**(11): 1323-1329.

Collier, J. G. (1996). Convective Boiling and Condensation, Oxford Engineering Science Series.

Dhir, V. and Lienhard, J. (1971). Laminar film condensation on plane and axisymmetric bodies in nonuniform gravity, Journal of Heat Transfer, Transactions ASME **93 Ser C**(1): 97-100.

Dryahina, K., Pospíšilová, V., Sovová, K., Shestivska, V., Kubišta, J., Spesyvyi, A., Pehal, F., Turzíková, J., Votruba, J., Španěl, P. (2014) Exhaled breath concentrations of acetic acid vapour in gastro-esophageal reflux disease, Journal of Breath Reserach **8**(3): 037109.

Duguid, J. P. (1946). The size and the duration of air-carriage of respiratory droplets and droplet-nuclei, The Journal of Hygiene (London) **44**(6): 471-479.

Filipiak, W., Beer, R., Sponring, A., Filipiak, A., Ager, C., Schiefecker, A., Lanthaler, S., Helbok, R., Nagl, M., Troppmair, J., Amann, A. (2015) Breath analysis for in vivo detection of pathogens related to ventilator-associated pneumonia in intensive care patients: A prospective pilot study, Journal of Breath Reserach **9**(1): 016004.

Funk, D. and A. Kumar (2015). Ebola virus disease: an update for anesthesiologists and intensivists, Canadian Journal of Anesthesia **1**(62): 12.

Geng, G. Y. (1985) China, Chengdu: people's medical publishing house, Epidemiology(I).

Garner, J. S. (1996) Guideline for isolation precautions in hospitals. The Hospital Infection Control Practices Advisory Committee, Infection Control and Hospital Epidemiology, **17**(1): 53-80.

Goldsmith, M. (1955) The Burning of Single Drops of Fuel in Oxidizing Atmosphere, Ph.D. disserttion, Califonia Institute of Technology.

Gralton, J., Tovey, E., McLaws, M. L. and Rawlinson, W. D. (2011) The role of particle size in aerosolised pathogen transmission: a review, Journal of Infection **62**(1): 1-13.

Gupta, J. K., Lin, C.-H., Chen, Q. (2009a) Flow dynamics and characterization of a cough, Indoor Air, **19**(6): 517-525.

Gupta, J. K., Lin, C.-H., Chen, Q. (2009b) Characterizing exhaled airflow from breathing and talking, Indoor Air, **20** (1), pp. 31-39.

Gupta, J. K., Lin, C-H., Chen, Q., (2011) Inhalation of expiratory droplets in aircraft cabins, Indoor Air, **21**: 341–350

He, F., Wang, J., Xu, L., Wang, X., (2013) Modeling and simulation of transpiration cooling with phase change, Applied Thermal Engineering, **58** 173-180

Heili-Frades, S., Peces-Barba, G., María Jesús Rodríguez-Nieto. (2007) Design of a Lung Simulator for Teaching Lung Mechanics in Mechanical Ventilation, Arch Bronconeumol. **43**(12): 674-9

Heo, J., Park H., and Yun, R. (2013) Comparison of condensation heat transfer and pressure drop of CO 2 in rectangular microchannels, International Journal of Heat and Mass Transfer, **65**: 719-726.

Incropera, F. P. and DeWitt, D. P. (2011). Introduction to Heat Transfer, Wiley.

Kang, D. K. (2017) Human breath simulator using controlled evaporator mixer to test the performance of a breath alcohol analyzer, Applied Thermal Engineering, **110**: 363–368

Kim, M. H. and Corradini, M. L. (1990) Modeling of condensation heat transfer in a reactor containment, Nuclear Engineering and Design, **118**(2): 193-212.

Kuhli, M., Weiss, M. and Steckel, H. (2009) A sampling and dilution system for droplet aerosols from medical nebulisers developed for use with an optical particle counter, Journal of Aerosol Science **40**(6): 523-533.

Li, J. D. (2013) CFD simulation of water vapour condensation in the presence of non-condensable gas in vertical cylindrical condensers, International Journal of Heat and Mass Transfer, **57**(2): 708-721.

Li, J. D., Saraireh, M. and Thorpe, G. (2011) Condensation of vapor in the presence of non-condensable gas in condensers, International Journal of Heat and Mass Transfer, **54**(17-18): 4078-4089.

Lindsley, W. G., Reynolds, J. S., Szalajda, J. V., Noti, J. D. and Beezhold, D. H. (2013) A cough aerosol simulator for the study of disease transmission by human cough-generated aerosols, Aerosol Science and Technology,**47**(8): 937-944.

Liu, J., Aizawa, H. and H. Yoshino (2004) CFD prediction of surface condensation on walls and its experimental validation, Building and Environment, **39**(8 SPEC. ISS.): 905-911.

Mandø, M. and Rosendahl, L. (2010) On the motion of non-spherical particles at high Reynolds number, Powder Technology, **202**(1-3): 1-13.

Mazumdar, S. and Chen, Q. (2008) Influence of cabin conditions on placement and response of contaminant detection sensors in a commercial aircraft, Journal of Environmental Monitoring, **10**, 71–81.

Minkowycz, W. J. and Sparrow, E. M. (1966) Condensation heat transfer in the presence of noncondensables, interfacial resistance, superheating, variable properties, and diffusion, International Journal of Heat and Mass Transfer, **9**(10): 1125-1144.

Morawska, L. (2006) Droplet fate in indoor environments, or can we prevent the spread of infection, Indoor Air, **16**(5): 335-347.

Moser, M. R., Bender, T. R., Margolis, H. S., Noble, G. R., Kendal, A. P. and Ritter, D. G. (1979) An Outbreak of Influenza aboard a Commercial Airline., American Journal of Epidemiology, **110**: 1-6.

Nicas, M., Nazaroff, W. W. and Hubbard, A. (2005) Toward Understanding the Risk of Secondary Airborne Infection: Emission of Respirable Pathogens, Journal of Occupational and Environmental Hygiene, **2**: 143–154.

Noti, J. D., Lindsley, W. G., Blachere, F. M., Cao, G., Kashon, M. L., Thewlis, R. E., McMillen, C. M., King, W. P., Szalajda, J. V. and Beezhold, D. H. (2012) Detection of Infectious Influenza Virus in Cough Aerosols Generated in a Simulated Patient Examination Room, Infectious Influenza in Cough Aerosols **54** (1 June): 1577

Nusselt, W. (1916) Die oberflächenkondensation des wasserdampfes Z. Ver. Dt. Ing. **60**(27): 541-546.

O'Hanlon, J. F. (1989). A User's Guide to Vacuum Technology.

Olsen, S. J., Chang, H. L., Cheung, T. Y., Tang, A. F., Fisk, T. L., Ooi, S. P., Kuo, H. W., Jiang, D. D., Chen, K. T., Lando, J., Hsu, K. H., Chen, T. J. and Dowell, S. F. (2003) Transmission of the severe acute respiratory syndrome on aircraft, The New England Journal of Medicine, **349**(25): 2416-2422.

Osterholm, M. T., Moore, K. A., Kelley, N. S., Brosseau, L. M., Wong, G., Murphy, F. A., Peters, C. J., LeDuc, J. W., Russell, P. K., Van Herp, M., Kapetshi, J., Muyembe, J. J., Ilunga, B. K., Strong, J. E., Grolla, A., Wolz, A., Kargbo, B., Kargbo, D. K., Sanders, D. A. and Kobinger, G. P. (2015) Transmission of Ebola viruses: what we know and what we do not know, mBio **6**(2): e00137-00115.

Patel, R., Patel, R., Zhu, C. and Lin, C.-H. (2011) Flushing of non-condensable gases by saturated steam, Proceedings of the ASME/JSME 2011 8th Thermal Engineering Joint Conference.

Ross, BB. (1955) Physical dynamics of the cough mechanism, Journal of Applied Physiology, **8**(3):264-8.

Shaker, M., Hunt, J. (2008) An economic analysis of an acid-reflux breath test in the evaluation of chronic cough, Journal of Breath Research, **2**(3): 037006.

Shen, S. C., Wang, Y. J. and Chen, Y. Y. (2008) Design and fabrication of medical micro-nebulizer, Sensors Actuat, A-Physical, **144**(1): 135-143.

Sirignano, W. A. (1999) Fluid Dynamics and Transport of Droplets and Sprays, Cambridge University Press.

Sparrow, E. M., Minkowycz, W. J. and Saddy, M. (1967) Forced convection condensation in the presence of noncondensables and interfacial resistance, International Journal of Heat and Mass Transfer, **10**(12): 1829-1845.

Steckel, H. and Eskandar, F. (2003) Factors affecting aerosol performance during nebulization with jet and ultrasonic nebulizers, European Journal of Pharmaceutical Sciences, **19**(5): 443-455.

Xueqiang Suna, David J. Ewing B. (2012) Lin Ma A laser extinction based sensor for simultaneous droplet size and vapor measurement, Particuology, **10**: 9–16

Sze To, G. N., Wan, M. P., Chao, C. Y. H., Fang, L. and Melikov, A. (2009) Experimental Study of Dispersion and Deposition of Expiratory Aerosols in Aircraft Cabins and Impact on Infectious Disease Transmission, Aerosol Science and Technology, **43**: 466–485.

Taylor, D. R. (2012) Advances in the clinical applications of exhaled nitric oxide measurements, Journal of Breath Research, **6**(4), 047102.

Thomas, R. J. (2013) Particle size and pathogenicity in the respiratory tract, Virulence, **4**(8): 847-858.

VanSciver, M., Miller, S. and Hertzberg, J. (2011) Particle Image Velocimetry of Human Cough, Aerosol Science and Technology, **45**: 415–422.

Wan, M. P., Chao, C. Y. H., Ng, Y. D., Sze To, G. N. and Yu, W. C. (2007) Dispersion of expiratory droplets in a general hospital ward with ceiling mixing type mechanical ventilation system, Aerosol Science and Technology, **41**(3): 244–258.

Wan, M.P., Sze To, G.N., Chao, C.Y.H., Fang, L. and Melikov, A. (2009) Modeling the fate of expiratory aerosols and the associated infection risk in an aircraft cabin environment, Aerosol Science and Technology, **43**(4): 322–343.

Wang, B., A. Zhang, J. L. Sun, H. Liu, J. Hu and L. X. Xu (2005). "Study of SARS transmission via liquid droplets in air." J Biomech Eng **127**(1): 32-38.

Weast, R. C. (1989) CRC Handbook of Chemistry, and Physics, 70th Edition, Ed., CRC Press, Boca Raton, FL, p. D-221.

WHO. (2007) infection prevention and control of epidemic- and pandemic-prone acute respiratory diseases in health care, from http://www.who.int/csr/resources/publications/WHO_CDS_EPR_2007_6c.pdf.

WHO. (2014) Unprecedented number of medical staff infected with Ebola, from http://www.who.int/mediacentre/news/ebola/25-august-2014/en/.

WHO. (2015) Ebola Situation Report - 14 October 2015, from http://apps.who.int/ebola/current-situation/ebola-situation-report-14-october-2015.

Wolf, A. V., Aqueous Solutions and Body Fluids, Harper and Row,New York, 1966.

Xie, X., Li, Y., Chwang, A., Ho, P. and Seto, W. (2007) How far droplets can move in indoor environments - revisiting the Wells evaporation-falling curve, Indoor Air, **17**: 211-225.

Yan, W., Zhang, Y., Sun, Y. and Li, D. (2009) Experimental and CFD study of unsteady airborne pollutant transport within an aircraft cabin mock-up, Building and Environment, **44**(1): 34–43.

Yang, S., G. Lee, W., Chen, C. M., Wu, C. C. and Yu, K. P. (2007) The size and concentration of droplets generated by coughing in human subjects, Journal of Aerosol Medicine, **20**(4): 484-494.

Zhang, H., L. D., X. L. and X. Y. (2015) Documentary Research of Human Respiratory Droplet Characteristics, Procedia Engineering, **121**: 1365-1374.

Zhang, X., Zhao, X., Du, H., Ma, J. and Rong, J. (2014) Effect of different breath alcohol concentrations on driving performance in horizontal curves, Accident Analysis and Prevention, **72**: 401–410

Zhang, Z. and Chen, Q. (2007b) Comparison of the Eulerian and Lagrangian methods for predicting particle transport in enclosed spaces, Atmospheric Environment, **41**(25), 5236–5248.

Zhang, Z., Chen, X., Mazumdar, S., Zhang, T. and Chen, Q. (2009) Experimental and numerical investigation of airflow and contaminant transport in an airliner cabin mockup, Building and Environment, **44**(1): 85–94.

Zhou, Z., Smith, B. and Yadigaroglu, G.. (1997) A mathematical model and its analytical solution for slow depressurization of a gas-filled vessel, Journal of Engineering Mathematics, **31**(1): 43-57.

Zhu, C., Slaughter, M. C., Soo, S. L. (1991) Measurement of Velocity of Particles in a Dense Suspension by Cross-Correlation of Dual Laser Beams, Review of Scientific Instruments, **62**(8): 2036-2039.

Zhu, S., Kato, S. and Yang, J.-H. (2006) Study on transport characteristics of saliva droplets produced by coughing in a calm indoor environment, Building and Environment, **41**: 1691–1702.